



**Michigan
Technological
University**

Michigan Technological University
Digital Commons @ Michigan Tech

Dissertations, Master's Theses and Master's Reports

2016

Design for Low-Cost Gas Metal Arc Weld-Based Aluminum 3-D Printing

Amberlee S. Haselhuhn
Michigan Technological University, aslifer@mtu.edu

Copyright 2016 Amberlee S. Haselhuhn

Recommended Citation

Haselhuhn, Amberlee S., "Design for Low-Cost Gas Metal Arc Weld-Based Aluminum 3-D Printing", Open Access Dissertation, Michigan Technological University, 2016.
<https://doi.org/10.37099/mtu.dc.etr/172>

Follow this and additional works at: <https://digitalcommons.mtu.edu/etr>

DESIGN FOR LOW-COST GAS METAL ARC WELD- BASED ALUMINUM 3-D PRINTING

By

Amberlee S. Haselhuhn

A DISSERTATION

Submitted in partial fulfillment of the requirements for the degree of

DOCTOR OF PHILOSOPHY

In Materials Science & Engineering

MICHIGAN TECHNOLOGICAL UNIVERSITY

2016

© 2016 Amberlee S. Haselhuhn

This dissertation has been approved in partial fulfillment of the requirements for the Degree of DOCTOR OF PHILOSOPHY in Materials Science & Engineering.

Department of Materials Science & Engineering

Dissertation Advisor: *Dr. Paul G. Sanders*

Committee Member: *Dr. Joshua M. Pearce*

Committee Member: *Dr. Stephen L. Kampe*

Committee Member: *Dr. Thomas Dorin*

Department Chair: *Dr. Stephen L. Kampe*

Table of Contents

List of Figures	vi
List of Tables	viii
Preface	ix
Acknowledgements	xi
Abstract	1
1 Gas Metal Arc Welding (GMAW) in Additive Manufacturing	3
1.1 Introduction	3
1.2 Gas Metal Arc Welding	3
1.3 3-D Printing & Additive Manufacturing	7
1.3.1 Subtractive vs. Additive Manufacturing	7
1.3.2 Methods of Printing Metal.....	9
1.4 References	11
2 A Low-Cost Open-Source GMAW-Based 3-D Printer	17
2.1 Description of GMAW-Based 3-D Printer	17
2.1.1 Basic Design	17
2.1.2 Evolution of 3-D Printer Design	19
2.1.3 Details of the Low-Cost Printer & 3-Axis Stage.....	20
2.2 Software Toolchain & Printing of Parts	21
2.3 Initial Prints & Metallurgical Considerations	22
2.4 References	25
3 Substrate Release Mechanisms for GMAW-Based 3-D Printing	27
3.1 Abstract.....	27
3.2 Introduction	28
3.3 Hypothesis.....	31
3.4 Materials & Methods	32
3.4.1 Description of the Metal 3-D Printer	32
3.4.2 Preparation of Print Substrates	33
3.4.3 Printing of Samples	33
3.4.4 Sample Testing & Analysis	35
3.5 Results.....	41
3.5.1 Dimensional Validation & 3-D Printed Part Inspection	41
3.5.2 Specimen-Substrate Impact Energy.....	42
3.5.3 Specimen Porosity	44
3.5.4 Specimen Microstructure	45
3.5.5 Specimen Hardness.....	47
3.5.6 Ultrasonic Modulus.....	48
3.6 Discussion.....	50
3.7 Conclusions	58
3.8 References	59

4 Structure-Properties Relationships of Common Aluminum Weld Alloys Utilized as Feedstock for GMAW-Based 3-D Printing	65
4.1 Abstract.....	65
4.2 Introduction	66
4.3 Background	67
4.4 Hypotheses	70
4.5 Materials and Methods.....	70
4.5.1 Description of the Metal 3-D Printer	70
4.5.2 Printing of Test Specimens.....	71
4.5.3 Specimen Machining & Analysis	73
4.6 Results.....	77
4.6.1 As-Printed Dimensions & Porosity.....	77
4.6.2 Influence of Specimen Location & Orientation on Mechanical Properties ..	79
4.6.3 Average Mechanical Properties	82
4.6.4 Microstructural Analysis	87
4.7 Discussion.....	91
4.7.1 As-Printed Dimensions & Porosity.....	91
4.7.2 Influence of Specimen Orientation on Mechanical Properties	93
4.7.3 Microstructural Analysis	95
4.7.4 Mechanical Properties	96
4.8 Conclusions	99
4.9 References	100
5 Aluminum Alloy Development for GMAW-Based 3-D Printing	108
5.1 Abstract.....	108
5.2 Introduction	109
5.2.1 Eutectic Modification Strategies in Hypoeutectic Al-Si Alloys.....	109
5.2.2 Grain Refinement in Hypoeutectic Aluminum-Silicon Alloys	112
5.2.3 Alloying Considerations for Welding	113
5.2.4 The Role of Wedge Castings in Alloy Development.....	115
5.3 Hypotheses	116
5.4 Materials & Methods	117
5.4.1 Description of Permanent Mold	117
5.4.2 Alloy Melting & Pouring.....	118
5.4.3 Alloy Testing & Analysis	120
5.5 Results.....	122
5.5.1 Microstructural Analysis	122
5.5.2 Mechanical Properties	125
5.5.3 Thermal Analysis	129
5.6 Discussion.....	131
5.7 Conclusions	134
5.8 References	135
6 3-D Printing of Experimental Aluminum Weld Wire	146

6.1	Abstract.....	146
6.2	Introduction	146
6.3	Hypotheses	147
6.4	Materials & Methods	148
6.4.1	Casting of Experimental Alloys	148
6.4.2	Extrusion & Heat Treatment.....	150
6.4.3	Wire Drawing	150
6.4.4	3-D Printing.....	150
6.4.5	Machining & Analysis.....	153
6.5	Results.....	154
6.6	Discussion.....	161
6.7	Conclusion.....	166
6.8	References	167
7	Conclusions.....	169

List of Figures

Figure 1.1 Schematic drawing of the GMAW process near the arc.	4
Figure 1.2 Schematic comparison of manufacturing methods.....	7
Figure 1.3 Comparison of single-layer multi-pass welding and GMAW-based 3-D printing.....	10
Figure 2.1 Comparison of plastic and metal printers.....	18
Figure 2.2 Evolution of the low-cost GMAW-based 3-D printing system.....	19
Figure 2.3 Toolchain used to print metal parts.	22
Figure 3.1 Labeled photograph of the GMAW-based metal 3-D printer shown with the M-100 weld gun for steel printing	32
Figure 3.2 Alternating print paths for the 3-D metal printer as viewed in the direction of the z-axis.	34
Figure 3.3 Schematic diagram of the modified Charpy impact tester	36
Figure 3.4 Schematic diagram describing lines along which hardness measurements were taken.....	39
Figure 3.5 Macro images of the interface between the 3-D printed part and the substrate.	42
Figure 3.6 Impact energy required to remove 3-D printed specimens from a print substrate based upon substrate release mechanism employed.....	43
Figure 3.7 Average specimen porosity measured via the Archimedes method:.....	44
Figure 3.8 Representative 3-D printed microstructures.....	46
Figure 3.9 Scanning electron images of aluminum specimens printed on steel near the specimen center.....	47
Figure 3.10 Representative hardness profiles.	48
Figure 3.11 Elastic and shear moduli of 3-D printed specimens.	50
Figure 4.1 Alternating print paths for all specimens viewed in the direction of the z-axis	73
Figure 4.2 Orientation of compression and microstructural specimen machining.	74
Figure 4.3 A dendrite in 4047 aluminum with a schematic line.....	76
Figure 4.4 Average center bead width in the top print layer for each aluminum alloy. ...	78
Figure 4.5 Average porosity of the as-printed specimens.....	79
Figure 4.6 Influence of specimen orientation on ultrasonic moduli.	80
Figure 4.7 Influence of specimen location in printed block on mechanical properties. ...	81
Figure 4.8 Influence of specimen orientation in printed block on compressive yield strength.....	81
Figure 4.9 Tensile fracture surfaces of 3-D printed aluminum alloys.	83
Figure 4.10 Examples of porosity in each 3-D printed aluminum alloy.....	84
Figure 4.11 Brittle 4047 fracture surface.....	85
Figure 4.12 Average mechanical properties of printed specimens.	86
Figure 4.13 Estimate of the strain hardening response of each aluminum alloy based upon solute content.	87

Figure 4.14 Scanning electron images of 4000 series test specimens in the bottom, top, and middle of the printed block.	88
Figure 4.15 Secondary dendrite arm spacing (SDAS) analysis of printed specimens.....	89
Figure 4.16 Secondary electron images of iron contamination in the first print layer of 1100 and 4047.....	90
Figure 4.17 Iron gradient from EDS of the first two print layers of 4043 and 4047.	90
Figure 4.18 Variation in microstructures observed in 4047 tensile specimens.	91
Figure 4.19 Calculated diffusion length of iron in aluminum as a function of solidification time.	94
Figure 5.1 Influence of alloying additions on the weld crack susceptibility in aluminum welds.	114
Figure 5.2 Schematic drawings of the wedge casting and permanent mold.	117
Figure 5.3 Schematic drawing of the wedge castings with dashed lines to represent cut sections.....	120
Figure 5.4 Schematic drawing showing the approximate origin of tensile bars.	121
Figure 5.5 Comparative microstructures of the high-silicon alloys.....	122
Figure 5.6 Comparative eutectic microstructures of the high-silicon alloys.	123
Figure 5.7 Comparative microstructures of the low-silicon alloys.....	124
Figure 5.8 Comparative eutectic microstructures in the low-silicon alloys.....	125
Figure 5.9 Average porosity of the cast experimental alloys.....	126
Figure 5.10 Average 0.02% offset yield strength of the cast experimental alloys.	127
Figure 5.11 Average ultimate tensile strength of the cast experimental alloys.	128
Figure 5.12 Average elongation at break of the cast experimental alloys and corresponding quality index.....	129
Figure 5.13 Cooling curves of cast alloys.....	130
Figure 5.14 Eutectic growth temperature of cast alloys.	130
Figure 6.1 Image of the CNC-based 3-D printer from CNC Router Parts.	151
Figure 6.2 Porosity of 3-D printed specimens.	155
Figure 6.3 Averaged mechanical properties of each printed alloy.	156
Figure 6.4 Mechanical properties based upon chill condition.	157
Figure 6.5 Average secondary dendrite arm spacing of printed alloys based upon chill condition.	159
Figure 6.6 Comparison of as-cast billet microstructures of experimental alloys.	160
Figure 6.7 Comparison of as-extruded and heat-treated extrusions.	160
Figure 6.8 Comparison of 3-D printed microstructures.....	161

List of Tables

Table 1.1 Comparison of the Three Transfer Modes Common to GMAW	5
Table 1.2 Common Aluminum Filler Metals in Welding	6
Table 2.1 Initial Observations from Printing Steel vs. Aluminum	23
Table 2.2 Thermal Properties of Aluminum Compared with Carbon Steel.	24
Table 3.1 Substrate Release Mechanisms Analyzed by this Study	31
Table 3.2 3-D Metal Print Parameters Used to Produce 1" Cubes	34
Table 3.3 Aluminum and Steel Modulus Values as Reported in the Literature	54
Table 4.1 Common Aluminum Weld Alloys	68
Table 4.2 Compositions of Aluminum Weld Wire	72
Table 4.3 3-D Printing Parameters	72
Table 4.4 Average Calculated Elastic Properties for Each Aluminum Alloy	82
Table 4.5 Mechanical Properties of Aluminum Alloys from Multiple Processes Compared with Study Results	98
Table 5.1 Strontium Levels in Hypoeutectic Al-Si Alloys as Reported in the Literature	111
Table 5.2 Target Compositions of Experimental Alloys.	118
Table 6.1 Target Compositions of Experimental Alloys.	148
Table 6.2 3-D Printing Parameters	152
Table 6.3 Ultrasonic Moduli of Printed Alloys.	158
Table 6.4 Comparison of Cast and 3-D Printed Chemistries	161
Table 6.5 Mechanical Properties of Experimental Aluminum Alloys Compared with Previous Results	162
Table 6.6 Results of Hypothesis Testing	165

Preface

This dissertation was prepared, in part, with the work of published journal articles and journals accepted for publication. These publications have been developed by Amberlee Haselhuhn, Dr. Joshua M. Pearce, and Dr. Paul G. Sanders.

All experimental work discussed within this dissertation was performed by Amberlee Haselhuhn. In some cases, the assistance of undergraduate researchers and staff members was used to print specimens and perform measurements. Undergraduate students Eli Gooding, Ali Glover, Michael Buhr, Brian Brook, Lauren Borowicz, Emily Hunt, and Violet Thole assisted with sample printing and polishing. Fellow graduate student Bas Wijnen developed the firmware, Franklin, used to 3-D print parts. Amberlee Haselhuhn and Dr. Paul G. Sanders developed the project, experimental design, and presentation of the results.

This dissertation includes the following peer reviewed journal articles with permission:

A.S. Haselhuhn, E.J. Gooding, A.G. Glover, G.C. Anzalone, B. Wijnen, P.G. Sanders, & J.M. Pearce. (2014). "Substrate Release Mechanisms for Gas Metal Arc 3-D Aluminum Metal Printing." *3-D Printing and Additive Manufacturing*. 1(4): 204-209. The final publication is available from Mary Ann Liebert, Inc., publishers <http://dx.doi.org/10.1089/3dp.2014.0015>.

A.S. Haselhuhn, B. Wijnen, G.C. Anzalone, P.G. Sanders, & J.M. Pearce. (2015). "In-Situ Formation of Substrate Release Mechanisms for Gas Metal Arc Weld Metal 3-D Printing." *Journal of Materials Processing Technology*. 226: 50-59.

A.S. Haselhuhn, M.W. Buhr, B. Wijnen, P.G. Sanders, & J.M. Pearce. (2016). "Structure-Property Relationships of Common Aluminum Weld Alloys Utilized as Feedstock for GMAW-Based 3-D Printing." *Materials Science & Engineering: A*. Submitted.

Acknowledgements

I would first like to express thanks to my advisor, Dr. Paul G. Sanders, for the extensive support he provided to develop and execute the research contained in this dissertation. His mentorship, patience, and motivational skills have helped me to become a better scientist and engineer, and are part of what made this work truly possible.

The work contained in this dissertation has been funded through America Makes and the Air Force Research Laboratory under agreement number FA8650-12-2-7230. I am grateful to the America Makes community for valuable feedback on my research.

I would like to extend sincere gratitude to the faculty and staff members who have provided significant technical assistance to this project. In particular, I would like to thank Dr. Joshua Pearce, Tom Wood, Paul Fraley, Pat Quimby, and Jerry Anzalone for their guidance and support throughout this project. I am grateful to fellow graduate student Bas Wijnen for the use of his printing firmware, Franklin, and for the countless hours he spent modifying his firmware for metal 3-D printing. I would also like to thank several undergraduate students, Eli Gooding, Ali Glover, Michael Buhr, Brian Brook, Lauren Borowicz, Emily Hunt, and Violet Thole for their assistance with 3-D printing and sample preparation.

Finally, I would like to thank Howard, Alicia, and Jake for their humor, friendship, guidance, and support throughout the graduate process.

Abstract

Additive manufacturing, commonly known as 3-D printing, has the potential to change the state of manufacturing across the globe. Parts are made, or printed, layer by layer using only the materials required to form the part, resulting in much less waste than traditional manufacturing methods. Additive manufacturing has been implemented in a wide variety of industries including aerospace, medical, consumer products, and fashion, using metals, ceramics, polymers, composites, and even organic tissues. However, traditional 3-D printing technologies, particularly those used to print metals, can be prohibitively expensive for small enterprises and the average consumer.

A low-cost open-source metal 3-D printer has been developed based upon gas metal arc weld (GMAW) technology. Using this technology, substrate release mechanisms have been developed, allowing the user to remove a printed metal part from a metal substrate by hand. The mechanical and microstructural properties of commercially available weld alloys were characterized and used to guide alloy development in 4000 series aluminum-silicon alloys. Wedge casting experiments were performed to screen magnesium, strontium, and titanium boride alloying additions in hypoeutectic aluminum-silicon alloys for their properties and the ease with which they could be printed. Finally, the top performing alloys, which were approximately 11.6% Si modified with strontium and titanium boride were cast, extruded, and drawn into wire. These wires were printed and the mechanical and microstructural properties were compared with those of commercially available alloys. This work resulted in an easier-to-

print aluminum-silicon-strontium alloy that exhibited lower porosity, equivalent yield and tensile strengths, yet nearly twice the ductility compared to commercial alloys.

1 Gas Metal Arc Welding (GMAW) in Additive Manufacturing

1.1 Introduction

The art and science of welding is an ancient practice, with the first recorded instances of hammer (or pressure) welding of decorative gold boxes from the Late Bronze Age in Ireland (Tylecote, 1978). Welding technology has matured since ancient times from an art to a true science. In the United States, Charles L. Coffin was awarded the first patent for a method to weld together metals using a metal arc in 1889 (Coffin, 1889). Since then, there has been a rich history of rapid technological advancement in the field of welding including gas metal arc welding, gas tungsten arc welding, stick welding, and most recently electron beam welding, laser beam welding, and friction stir welding (Kou, 1987; Lancaster, 1993). Of these methods, gas metal arc welding (GMAW) may be the most economical and broadly used method of fusion welding (Lancaster, 1993). Low associated costs, breadth of use, and availability to the average consumer led researchers to its use in a low-cost GMAW-based metal 3-D printer (Anzalone, et al., 2013).

1.2 Gas Metal Arc Welding

Gas metal arc welding (GMAW) is a fusion welding process in which two metals are joined by an arc forming between a consumable electrode and the workpiece (Figure 1.1) (Kou, 1987; Lancaster, 1993; Easterling, 1983).

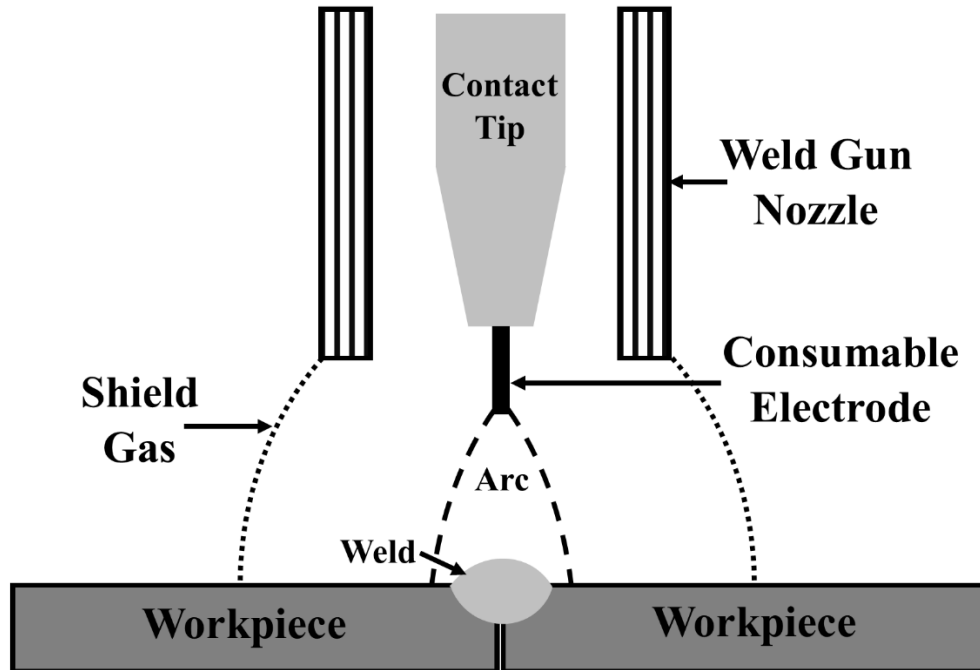
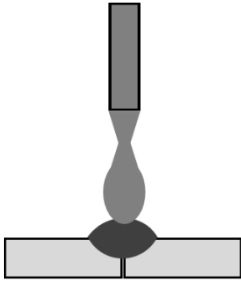
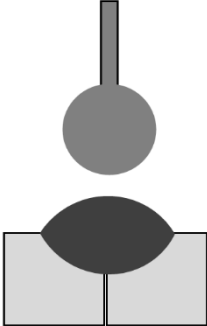
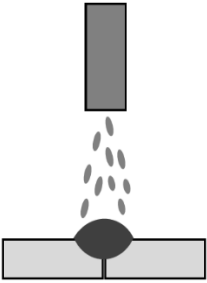


Figure 1.1 Schematic drawing of the GMAW process near the arc.

GMAW utilizes a protective shield gas, specific to the metal being welded, to protect the molten weld pool from atmospheric gas and moisture and to help control the shape and behavior of the weld pool. Argon and argon-helium gas mixtures are common with aluminum welding whereas argon and argon-carbon dioxide gas mixtures are commonly used to weld steel (Lyttle, 1993).

Upon the application of energy, the metal consumable is melted and transferred to the workpiece in one of three main transfer modes: Short-circuiting, globular, or spray transfer modes (Table 1.1) (Kou, 1987; Lancaster, 1993; Holliday, 1993).

Table 1.1 Comparison of the Three Transfer Modes Common to GMAW

	Short-Circuit	Globular	Spray
Diagram:			
Current Level:	Low	Medium	High
Droplet Size:	None	Droplet > Electrode	Droplet < Electrode
Droplet Transfer:	Contact with Workpiece	Gravity	Arc Acceleration
Shield Gas Dependent:	Moderate	No	Yes: Argon
Weld Sections:	Thin	Thick	Thin

Short-circuit transfer occurs at the lowest arc current levels in which the electrode melts and touches the weld pool while maintaining contact with the remainder of the electrode, forming a short circuit. This method of metal transfer results in a small weld pool that solidifies quickly and is thus ideally suited for thin metal sections. Globular transfer requires a mid-level of arc current. In globular transfer the electrode melts into droplets larger than the size of the electrode and gravity dominates the transfer of these large droplets to the workpiece. Spray transfer occurs at the highest arc currents under the influence of inert shield gas such as argon. In this metal transfer method, drops smaller than the electrode are accelerated by the arc to the workpiece. Spray transfer can result in deep weld penetration and is ideally suited to joining thick workpieces.

In GMAW it is important to choose filler metals to suit the base metal composition and the given application considering such factors as susceptibility to cracking, weld strength, ductility, thermal cycle of the part during welding and in service, susceptibility to corrosion, and in some cases, color matching (Dickerson, 1993). In aluminum alloys, common filler metals are 1000 series (high-purity aluminum), 2000 series (aluminum-copper), 4000 series (aluminum-silicon), or 5000 series (aluminum-magnesium) (Table 1.2).

Table 1.2 Common Aluminum Filler Metals in Welding (Hobart Brothers Company, 2014, 2016a, and 2016b; Dickerson, 1993)

Filler Metal	Main Alloying Element	Commonly Joins
1000	None; $\geq 99\%$ Aluminum	1000, 3000, & 5000 series Al
2000	Copper	2000 series Al
4000	Silicon	1000, 2000, 3000, & 6000 series Al
5000	Magnesium	5000, 6000, & 7000 series Al

Of these alloys, 4043 (Al-5.5Si) and 5356 (Al-5Mg) are most commonly used in the United States and are also some of the least expensive filler metals (Hobart Brothers Company, 2014). The 4043 alloy is commonly used to join 1000, 2000, 3000, and 6000 series aluminum alloys whereas 5356 is commonly used to join 5000, 6000, and 7000 series aluminum alloys (Dickerson, 1993; Hobart Brothers Company, 2016a; Hobart Brothers Company, 2016b).

1.3 3-D Printing & Additive Manufacturing

1.3.1 Subtractive vs. Additive Manufacturing

Traditional manufacturing is typically subtractive manufacturing in which a part is machined from a larger block of material, often resulting in a large amount of material waste (Figure 1.3).

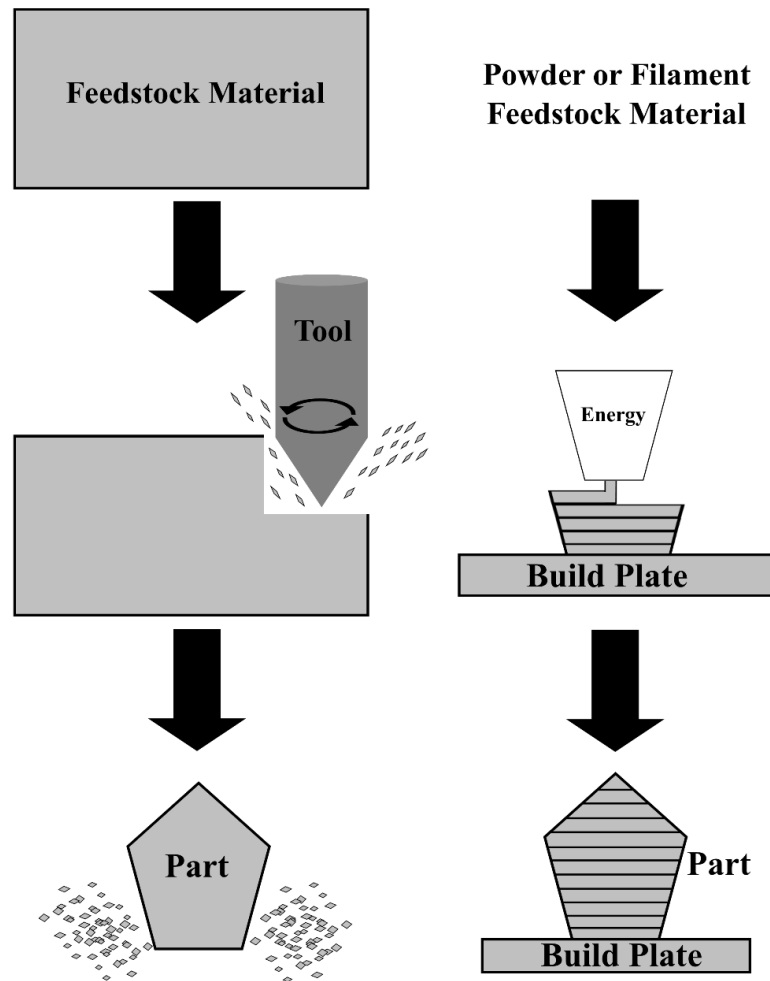


Figure 1.2 Schematic comparison of manufacturing methods. Traditional subtractive manufacturing is shown at left and additive manufacturing is shown at right.

The process of additive manufacturing begins with powder or filament. Energy is applied (in the form of an electron beam or laser) and a part is built layer by layer (Murr, et al., 2012a). Since less waste is produced by additive manufacturing compared to traditional manufacturing methods, the carbon footprint of manufacturing is reduced when additive processes are utilized (Frazier, 2014). For instance the buy to fly ratio, commonly used by aerospace companies to represent the ratio between raw material weight and final part weight, is much smaller in additive manufacturing (Horn & Harrysson, 2012). In subtractive manufacturing this number can be as large as 15-20 whereas in additive manufacturing this number is closer to 1.

Additive manufacturing is used in a wide variety of ways, from design and prototyping, small-batch production, to distributed manufacturing (Wohlers & Caffrey, 2014). It is typically utilized in specialized industries such as for aerospace applications, medical implants, and surgical models. It is also finding ground in scientific equipment, sporting equipment, clothing, jewelry, and art.

Media hype surrounds the additive manufacturing and 3-D printing technological revolution. For instance, CNBC has stated, “3-D Printing will make life as we know it today barely recognizable in 50 to 70 years,” (Federico-O’Murchu, 2014). The Economist has stated, “3-D printing will bring the third industrial revolution” (2012). However, the hype must be balanced with reality and researchers must ensure quality parts are being produced prior to production and implementation. The U.S. Government Accountability Office has identified key areas of 3-D printing that are currently lacking, including

characterization of 3-D printed materials and parts, which has become the focus of many academic institutions, national labs, and companies (Dodaro, 2015).

1.3.2 Methods of Printing Metal

Additive manufacturing was first demonstrated with laser curing of photopolymers on a layer-by-layer basis in the 1960's (Wohlers & Caffrey, 2014). Yet it wasn't until the mid-2000's that metal 3-D printers became commercially available (Murr, et al., 2012b). These metal printers utilized electron beams or lasers to selectively sinter or melt thin layers of metal powder according to instructions provided by a computer model in print resolutions on the micrometer scale. Common metal powders include stainless steels, Ti-6Al-4V, and nickel-based super alloys. Some electron beam or laser printers utilize wire feedstock to eliminate issues related to metal powder feeding and distribution (Tamingir & Hafley, 2003). An alternate method to 3-D print metal powders involves selectively printing a layer of liquid adhesive onto a thin layer of metal powder and subsequently sintered to burn off the adhesive and to sinter the metal particles (Kruth, 1991). Some of these metal powder printing techniques can be prohibitively expensive with some equipment priced at \$500,000-1.5 million (Peels, 2014).

A more affordable metal 3-D printing technique utilizes GMAW technology and can cost as little as \$2,000 or less (Chapter 2) (Anzalone, et al., 2013). Not only is the equipment more economical than laser and powder methods, but the consumable weld wire is also much more affordable, on the order of \$4.57 for 0.062" diameter stainless 316 wire versus \$10 per pound for an equivalent powder (Sciaky, 2016). The first

methods that can be described as weld-based 3-D printing were patented in 1972 to continuously weld circular vessels (Ujiie, 1972) and later in 1976 to produce large metal shafts and structural vessels (Brandi & Luckow, 1976). GMAW-based 3-D printing is also known as wire and arc additive manufacturing (WAAM) (Ding, et al., 2015). This method of printing is closely related to single-layer multi-pass welding (Figure 1.4) (Lancaster, 1993).

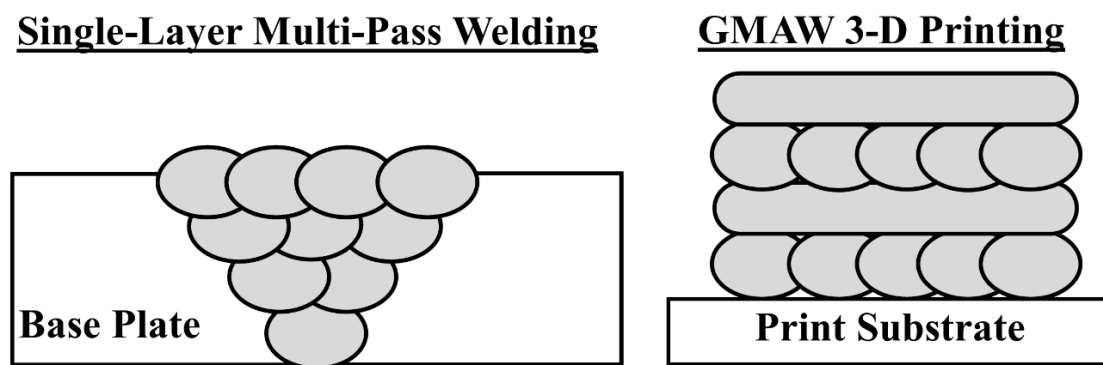


Figure 1.3 Comparison of single-layer multi-pass welding and GMAW-based 3-D printing Welding schematic (left) and 3-D printing (right).

In GMAW-based 3-D, weld beads vary in direction and orientation rather than being welded in the same direction as is done in single-layer multi-pass welding. Additionally, there's no dilution of weld filler metals in 3-D printing as there is in normal gas metal arc welding, so the part is dependent upon high quality filler metals for its microstructural and mechanical properties (Martukanitz, 1993). The weld transfer mode best suited for 3-D printing is the short-circuit mode as this mode is easy to control, has little weld spatter, and minimizes heat input into the rest of the 3-D printed part (Heard, et al., 2012). Low

weld currents and fast weld speeds reduce heat input into the welded part, minimizing temperature effects to part dimensions, microstructure, or properties (Lancaster, 1993).

Due to a larger print resolution on the order of millimeters, considerable work has been performed to sense and control the GMAW-based 3-D printing process. Ding, et al., developed a model to optimize weld bead overlap to obtain fully dense parts with good dimensional control (2015). Xiong & Zhang developed a vision sensor to monitor weld bead height during printing and to adjust print settings to maintain a consistent layer height (2014). Other researchers have combined GMAW-based 3-D printing with milling, milling each layer to precise geometries before the next layer is printed (Song, et al., 1999; Song, et al., 2005a; Song, et al., 2005b; Akula & Karunakaran, 2006). Additional work has been performed to minimize the environmental impact of this 3-D printing method by developing substrate release mechanisms for sample removal and substrate reuse (Chapter 3) (Haselhuhn, et al., 2014; Haselhuhn, et al., 2015) and to develop alloys that are easy to print by the GMAW-based methods (Chapter 5).

1.4 References

- Akula, S., & Karunakaran, K. P. (2006). Hybrid adaptive layer manufacturing: An Intelligent art of direct metal rapid tooling process. *Robotics and Computer-Integrated Manufacturing*. 22(2): 113–123.
- Anzalone G. C., Zhang C., Wijnen B., Sanders, P. G., Pearce, J. M. (2013). A low-cost open-source metal 3-D printer. *IEEE Access*, 1: 803-810.

- Brandi, H. T., & Luckow, H. (1976). U.S. Patent No. 3,985,995. (Published October 12, 1976). Washington, DC: U.S. Patent and Trademark Office.
- Coffin, C. L. (1889). U.S. Patent No. 427971A (Published May 13, 1890). Washington, DC: U.S. Patent and Trademark Office.
- Dickerson, P. B. (1993). Welding of Aluminum Alloys. *ASM Handbook*, 6, 722-739.
- Ding, D., Pan, Z., Cuiuri, D., & Li, H. (2015). A multi-bead overlapping model for robotic wire and arc additive manufacturing (WAAM). *Robotics and Computer-Integrated Manufacturing*. 31: 101–110.
- Dodaro, G. L. (2015). 3D Printing: Opportunities, Challenges, and Policy Implications of Additive Manufacturing. United States Government Accountability Office.
- Easterling, K. Introduction to the physical metallurgy of welding; 1983. London, Butterworth.
- Federico-O’Murchu, L. (11 May 2014). How 3-D printing will radically change the world. CNBC. <http://www.cnbc.com/2014/05/09/will-3-d-technology-radically-change-the-world.html>, Last accessed 22 March 2016.
- Frazier, W. E. (2014). Metal Additive Manufacturing: A Review. *Journal of Materials Engineering and Performance*. 23(6), 1917–1928.

- Haselhuhn, A. S., Gooding, E. J., Glover, A. G., Anzalone, G. C., Wijnen, B., Sanders, P. G., & Pearce, J. M. (2014). Substrate release mechanisms for gas metal arc weld 3-D aluminum metal printing. *3-D Printing & Additive Manufacturing*. 1(4), 204-209.
- Haselhuhn, A. S., Wijnen, B., Anzalone, G.C., Sanders, P.G., & Pearce, J.M. (2015). In situ formation of substrate release mechanisms for gas metal arc weld metal 3-D printing. *Journal of Materials Processing Technology*. 226, 50-59.
- Heard, D. W., Brophy, S., & Brochu, M. (2012). Solid freeform fabrication of Al-Si components via the CSC-MIG process. *Canadian Metallurgical Quarterly*.
- Hobart Brothers Company. (2014). Aluminum Filler Metals: Selection, Characteristics and More. <http://www.hobartbrothers.com/news/183/523/Aluminum-Filler-Metals-Selection-Characteristics-and-More.html>, last accessed 22 March 2016.
- Hobart Brothers Company. (2016a). Hobart MAXAL 4043. http://maxal.com/Hobart_Maxal_4043.pdf, last accessed 3 February 2016.
- Hobart Brothers Company. (2016b). Hobart MAXAL 5356. http://maxal.com/Hobart_Maxal_5356.pdf, last accessed 3 February 2016.
- Holliday, D. B. (1993). Welding of Aluminum Alloys. *ASM Handbook*, 6, 180-185.
- Horn, T. J., & Harrysson, O. L. A. (2012). Overview of current additive manufacturing technologies and selected applications. *Science Progress*. 95(3): 255–282.

- Kellner, T. (14 April 2015). The FAA cleared the first 3D printed part to fly in a commercial jet engine from GE. GE Reports. <http://www.gereports.com/post/116402870270/the-faa-cleared-the-first-3d-printed-part-to-fly/>, last accessed 22 March 2016.
- Kou, S. *Welding Metallurgy*; 1987. New York: John Wiley & Sons.
- Kruth, J. P. (1991). Material increment manufacturing by rapid prototyping techniques. *CIRP Annals-Manufacturing Technology*. 40(2): 603-614.
- Lancaster, J. F. *Metallurgy of Welding*; 1993. London, Chapman & Hall.
- Lytle, K.A. (1993). Welding of Aluminum Alloys. *ASM Handbook*, 6, 64-69.
- Martukanitz, R. P. (1993). Selection and Weldability of Heat-Treatable Aluminum Alloys. *ASM Handbook*, 6, 528-536.
- Murr, L. E., Martinez, E., Amato, K. N., Gaytan, S. M., Hernandez, J., Ramirez, D. A., ... & Wicker, R. B. (2012a). Fabrication of Metal and Alloy Components by Additive Manufacturing: Examples of 3D Materials Science. *Journal of Materials Research and Technology*. 1(1): 42-54.
- Murr, L. E., Gaytan, S. M., Ramirez, D. A., Martinez, E., Hernandez, J., Amato, K. N., ... & Wicker, R. B. (2012b). Metal Fabrication by Additive Manufacturing Using Laser and Electron Beam Melting Technologies. *Journal of Materials Science & Technology*. 28(1): 1-14.

- Peels, J. (23 May 2014). Metal 3D printing: From lab to fab. Inside 3DP. <http://www.inside3dp.com/metal-3d-pinting-lab-fab/>, last accessed 22 March 2016.
- Sciaky, Inc. (2016). Advantages of wire AM vs. Powder AM. <http://www.sciaky.com/additive-manufacturing/wire-am-vs-powder-am>, last accessed 22 March 2016.
- Song, Y.-A., Park, S., Jee, H., Choi, D., & Shin, B. (1999). 3D Welding and Milling - A Direct Approach for Fabrication of Injection Molds. In *Proceedings of the Solid Freeform Fabrication Symposium* (pp. 793–800). Austin, Texas.
- Song, Y.-A., Park, S., & Chae, S.-W. (2005). 3D welding and milling: part II— optimization of the 3D welding process using an experimental design approach. *International Journal of Machine Tools and Manufacture*. 45(9): 1063–1069.
- Song, Y.-A., Park, S., Choi, D., & Jee, H. (2005). 3D welding and milling: Part I—a direct approach for freeform fabrication of metallic prototypes. *International Journal of Machine Tools and Manufacture*. 45(9): 1057–1062.
- Taminger, K. M. B., & Hafley, R. A. (2003). Electron Beam Freeform Fabrication: A Rapid Metal Deposition Process. Presented at the 3rd Annual Automotive Composites Conference, Troy, MI: Society of Plastics Engineers, Inc.
- The Economist Newspaper Limited. (21 April 2012). A third industrial revolution. <http://www.economist.com/node/21552901>, last accessed 22 March 2016.

Tylecote, R. F. (1978). The Solid Phase Bonding of Gold to Metals. *Gold Bulletin*. 11(3): 74–80.

Ujiie, A. (1972). U.S. Patent No. 3,665,143. (Published May 23, 1972). Washington, DC: U.S. Patent and Trademark Office.

Wohlers, T., & Caffrey, T. (2014). Wohlers Report 2014 Annual Worldwide Progress Report. Wohlers Associates, Inc. Fort Collins, CO.

Xiong, J., & Zhang, G. (2014). Adaptive control of deposited height in GMAW-based layer additive manufacturing. *Journal of Materials Processing Technology*. 214(4): 962–968.

2 A Low-Cost Open-Source GMAW-Based 3-D Printer¹

2.1 Description of GMAW-Based 3-D Printer

2.1.1 Basic Design

An open-source GMAW-based metal 3-D printer was designed to be a low-cost (<\$2,000) alternative to traditional metal 3-D printers. This printer was comprised of two distinct components, a workshop-grade gas metal arc welder (GMAW) and a 3-axis stage (Figure 2.1) (Anzalone, et al., 2013; Haselhuhn, et al., 2014). The GMAW, a Millermatic 140 or Millermatic 190 with a standard weld gun, supplied the material used to print and the energy required to melt the material. The 3-axis stage was microprocessor controlled, permitting precise computer numerical control (CNC) of both the position and speed of the platform upon which parts were printed. Parts were built upon a sacrificial 6.35 mm thick mild steel or aluminum plate.

¹ The material contained within this chapter has been published in the journal “*3-D Printing & Additive Manufacturing*.” The final publication is available from Mary Ann Liebert, Inc., publishers <http://dx.doi.org/10.1089/3dp.2014.0015>:

A.S. Haselhuhn, E.J. Gooding, A.G. Glover, G.C. Anzalone, B. Wijnen, P.G. Sanders, & J.M. Pearce. (2014). “Substrate Release Mechanisms for Gas Metal Arc 3-D Aluminum Metal Printing.” *3-D Printing and Additive Manufacturing*. 1(4): 204-209.

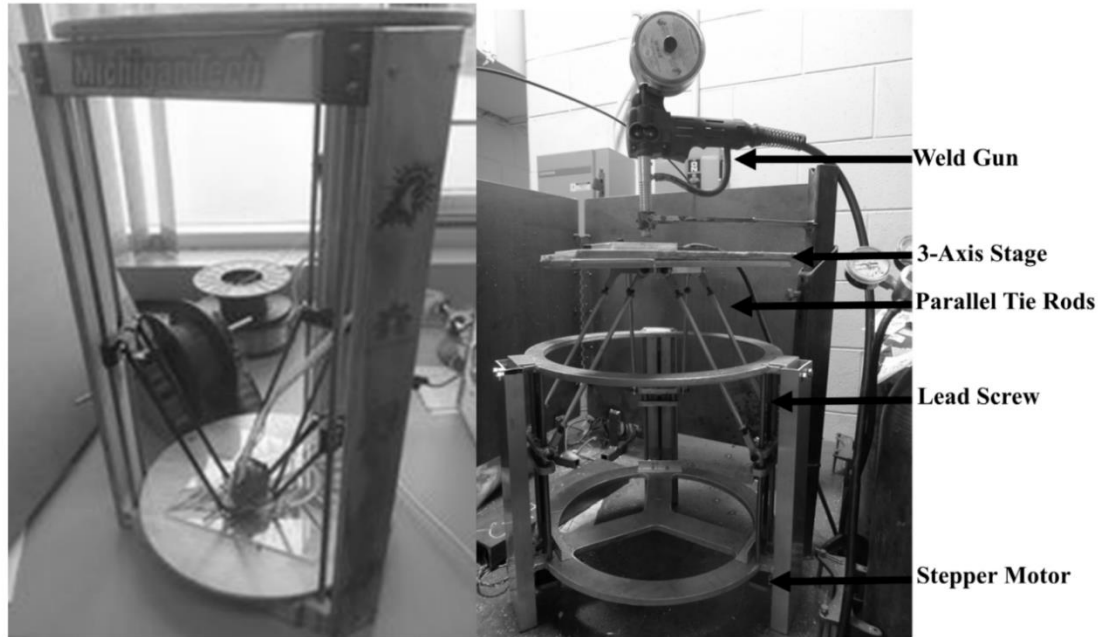


Figure 2.1 Comparison of plastic and metal printers. Photograph of a Rostock printer at Michigan Tech (left) and the GMAW-based metal 3-D printer (right).

The stage was derived from an open-source 3-D printer design known as a Rostock, which is a RepRap derivative (Figure 2.1) (RepRap Org, 2014). The original Rostock printer had the extruder mounted on the moving end effector whereas the 3-axis stage used in this work was essentially a Rostock turned upside-down, with the workpiece on the moving end effector and the "extruder" (welding gun) fixed in position above it.

During this study, welding parameters were set manually and the motion of the stage was adjusted to produce a quality bead. A quality bead was defined as a continuous line of 3-D printed material with consistent profile. Shield gas was used to minimize inclusions and spatter so as to produce a higher quality weld bead; argon shield gas was

used with aluminum and RC25, a 25% mixture of carbon dioxide in argon, was used with steel. Flux core wire was not utilized as it can leave a waste layer on top of the weld, making it difficult to print multiple layers.

2.1.2 Evolution of 3-D Printer Design

The low-cost GMAW-based printer has evolved to include improvements in safety, print area, and fluidity of motion (Figure 2.2).

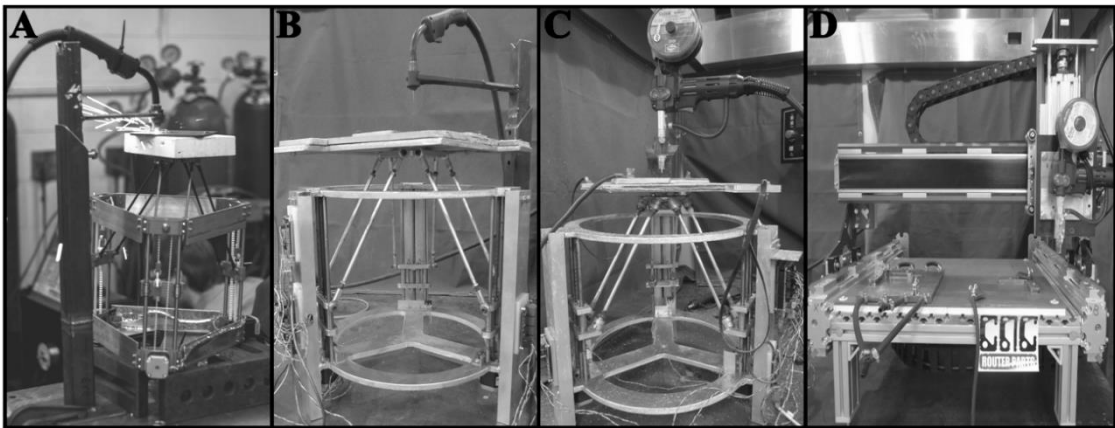


Figure 2.2 Evolution of the low-cost GMAW-based 3-D printing system. The metal-plastic printer (A) was modified to an all metal system with mechanical bearings (B). The mechanical bearings were switched for magnetic bearings (C). A new system based off a CNC router has also been developed (D).

The initial printer design (Figure 2.2 A) was comprised of both metal and plastic parts (Anzalone, et al., 2013). Motion of the stage was controlled via stepper motors and polymer-based belts. The initial printer was capable of printing within a 101 x 101 mm print area.

This printer was modified to an all-metal design to prevent melt-related damage to the printer from weld sparks (Figure 2.2 B) (Haselhuhn, et al., 2014). Motion of the stage was controlled with stepper motors and metal lead screws. The choice of insulation between print substrate and welder was improved such that a thinner, lighter piece of insulation could be used allowing for a reduction in both cost and weight. These improvements increased the allowable print area to 127 x 127 mm. Replacing mechanical bearings with magnetic bearings further increased the print area to 152 x 152 mm and produced more fluid motion of the 3-axis stage (Figure 2.2 C) (Nilsiam, et al., 2015).

An alternate printer design was developed by modifying a CNC router (CNC Router Parts) (Figure 2.2 D). Rather than a router, a weld gun was mounted to the moving gantry. Insulation, electrical grounds, and clamps to hold print substrates were added to the stationary build plate of the printer. This printer could print in an area up to 635 x 635 mm. Researchers could utilize this larger print area to print larger parts or to print multiple parts in quick succession. Additionally, as the build plate was stationary, a chill plate could be added to increase cooling of metal parts allowing for faster printing of larger parts.

2.1.3 Details of the Low-Cost Printer & 3-Axis Stage

The 3-axis stage is shown in Figure 2.2 B. All of the designs for the hardware and all of the software employed are free and open-source (Pearce, 2014). The all-metal construction minimized risk of damage due to weld spatter and heat. The drive mechanism utilized three NEMA17 stepper motors (5.5 kg-cm torque) with lead screws integrated into their shafts, requiring no couplings between the motors and lead screws

(Haselhuhn, et al., 2014; Nilsiam, et al., 2015). The trapezoidal-threaded lead screws had an 8 mm pitch and were 300 mm in length. The three motors were arranged vertically on a 394 mm circle, spaced 120° apart as shown in Figure 2.1. The lead screws and stepper motors allowed for 2.5 μm movement resolution. In general, the 3-axis stage was based upon an industrial delta robot design commonly used for pick-and-place operations, except allowing for greater movement in the z-direction.

Control was provided by an Arduino-based controller. Firmware (software resident on the printer's microcontroller) controlled the motion of the printer, translating commands from a printer server running on a host computer. The host computer, in turn, served a web interface from which the end user was able to control stage motion, queue print jobs, and make configuration changes.

2.2 Software Toolchain & Printing of Parts

RepRap 3-D printers utilize STereoLithography (.stl) files for the input. OpenSCAD, a script-based open source CAD package, is commonly used to develop the solid models (Figure 2.3) (OpenSCAD, 2014). The solid models are then sliced with the 3-D printing software, such as Cura, and converted into G-code (Ultimaker, 2014). G-code provided numerical control to the stepper motors, directing them when to move and how fast to move. For simple parts, such as cubes and blocks, it is also possible to manually write G-Code for stepper motor control using a text editor. The metal printer interfaced with these programs using a printer server developed at Michigan Tech with a web-based interface (Wijnen, et al., 2016). Print times depended upon part size and complexity, but most parts typically required less than 1 hour to print.

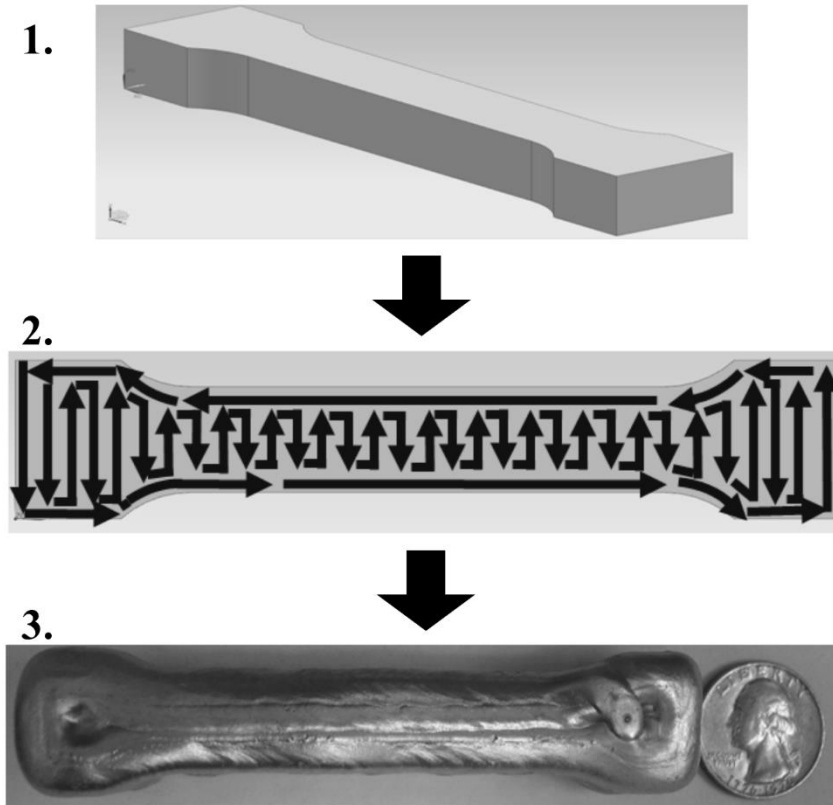
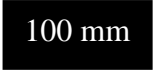




Figure 2.3 Toolchain used to print metal parts. A 3-D model is developed using modeling software (1). Using a slicing software, print paths are developed on a layer-by-layer basis for the parts (2). The printer uses the coded print paths to print a metal part (3).

2.3 Initial Prints & Metallurgical Considerations

These printers were initially used to print single-layer parts from both steel and aluminum. Steel was observed to be easier to print as it exhibited a finer print resolution, less porosity, and was easier to print in complex geometries without heat extraction issues (Table 2.1).

Table 2.1 Initial Observations from Printing Steel vs. Aluminum

	Steel	Aluminum
Print Resolution:	Finer: <1-3 mm	Coarser: 2-6 mm
Wire Diameters Used:	0.024”	0.030”, 0.035”
Porosity:	Less	More
Complex Geometry:	Simple	Difficult
Heat Extraction Issues:	Less	More
Residual Stress Effects:	More	Less
		

The finer print resolution in steel was easy to attain using smaller diameter wires. This smaller wire diameter also promoted the printing of more complex geometries in steel than aluminum. In preliminary work, aluminum wires on the order of 0.024” in diameter were evaluated to determine if a smaller diameter aluminum wire would result in comparable print resolutions as steel. However, the fine 0.024” diameter aluminum wires were exceedingly difficult to control due to arc wander issues and consistent, quality welds could not be achieved.

Aluminum exhibits greater porosity issues than steel when welded because aluminum is generally a more reactive metal than steel with gaseous elements. For instance, hydrogen gas is soluble in both liquid aluminum and liquid steel. Upon cooling, hydrogen exhibits a large solubility gap in aluminum and small solubility gaps in steel (Lancaster, 1993). The large hydrogen solubility gap in aluminum causes hydrogen pores to come out of solution, nucleating as pores.

The inherent differences in thermal properties of steel and aluminum result in the observed heat extraction issues (Table 2.2) (Kou, 1987).

Table 2.2 Thermal Properties of Aluminum Compared with Carbon Steel. (Kou, 1987)

Parameter	Aluminum	Carbon Steel
Thermal Diffusivity (m ² /sec)	8.5*10 ⁻⁵	9.1*10 ⁻⁶
Thermal Conductivity (W/m-K)	229	41
Volumetric Thermal Capacity (J/m ³ -K)	2.7*10 ⁶	4.5*10 ⁶
Melting Point (K)	933	1800

Aluminum readily responds to differences in temperature (thermal diffusivity) and is able to transfer a significant quantity of that heat to other parts of the metal part (thermal conductivity), but is unable to store much thermal energy without undergoing a phase transformation (volumetric thermal capacity). Steel is slower to respond to thermal changes, does not transfer as much of the heat to other parts of the metal part, and is capable of storing more thermal energy without undergoing a phase transformation as compared with aluminum. The more localized heating in steel makes it easier to print larger parts from steel than from aluminum while minimizing re-melting of previously printed layers.

The thermal properties of aluminum significantly reduce the residual stresses in aluminum weldments compared with steel (Lancaster, 1993). The linear contraction of a weld is a product of the metal's thermal expansion coefficient and the difference between its melting temperature and room temperature. While aluminum exhibits a larger thermal expansion coefficient than steel, it also exhibits a significantly smaller difference in

melting and room temperatures. This results in less contraction of the weld and less residual stress build-up in the metal. Additionally, the high thermal conductivity of aluminum results in a stress-relieving heat treatment upon printing of additional layers of metal, further reducing any residual stress-related distortion (Lancaster, 1993). Due to the observed differences in aluminum and steel in preliminary work, aluminum was determined to be more difficult to print with via weld-based methods. Thus, aluminum 3-D printing may benefit most from process and alloy modifications, guiding the course of this project.

2.4 References

Anzalone, G.C., Zhang, C., Wijnen, B., Sanders, P.G., & Pearce, J.M. (2013). A low-cost open-source metal 3-D printer. *IEEE*; 1: 803-810.

Haselhuhn, A. S., Gooding, E. J., Glover, A. G., Anzalone, G. C., Wijnen, B., Sanders, P. G., & Pearce, J. M. (2014). Substrate release mechanisms for gas metal arc weld 3-D aluminum metal printing. *3-D Printing & Additive Manufacturing*, 1(4), 204-209.

Kou, S. *Welding Metallurgy*; 1987. New York: John Wiley & Sons.

Lancaster, J. F. *Metallurgy of Welding*; 1993. London, Chapman & Hall.

Nilsiam, Y., Haselhuhn, A., Wijnen, B., Sanders, P. and Pearce, J.M., (2015). Integrated voltage-current monitoring and control of gas metal arc weld magnetic ball-jointed open source 3-D printer. *Machines.*, 3(4), pp.339-351.

OpenSCAD, <http://www.openscad.org>, last accessed June 24, 2014.

Pearce, J.M. Michigan Tech's Open Sustainability Technology Lab, Open-Source Metal 3-D Printer, http://www.appropedia.org/Open-source_metal_3-D_printer, last accessed June 24, 2014.

Reprap Org, Rostock, <http://reprap.org/wiki/Rostock>, last accessed June 24, 2014.

Ultimaker, Software Downloads, <http://software.ultimaker.com/>, last accessed June 24, 2014.

Wijnen, B., Anzalone, G.C., Haselhuhn, A.S., Sanders, P.G., & Pearce, J.M. (2016). Free and Open-Source Control Software for 3-D Motion and Processing. *Journal of Open Research Software*. 4(e2): 339-351.

3 Substrate Release Mechanisms for GMAW-Based 3-D Printing²

3.1 Abstract

This study provides an in-depth investigation into low-cost and no-cost substrate release mechanisms that allow gas metal arc welded 3-D printed ER4043 aluminum and ER70S-6 steel parts to be removed from a reusable print substrate with minimal energy. Aluminum oxide, boron nitride, and titanium nitride coatings were evaluated as possible substrate release agents for aluminum printing. Additionally, the in situ formation of substrate release agents such as intermetallics and oxides were tested for both aluminum and steel printing. Testing was performed with a modified Charpy impact tester to remove 3-D printed metal parts from an 1100 aluminum or A36 low carbon steel print substrate to assess the impact energy required for removal. Specimen porosity was measured prior to sectioning and microstructural analysis, hardness traverses were measured across the specimens, and the elastic and shear moduli of the parts were analyzed via ultrasonic methods. All of the employed substrate release mechanisms minimized weld penetration and, in some instances, formed a brittle phase with the print substrate that allowed the specimens to be removed with minimal impact energy. This

² The material contained within this chapter has been published in the journal “*Journal of Materials Processing Technology*.” This material can be found in the following publication:

A.S. Haselhuhn, B. Wijnen, G.C. Anzalone, P.G. Sanders, & J.M. Pearce. (2015). “In-Situ Formation of Substrate Release Mechanisms for Gas Metal Arc Weld Metal 3-D Printing.” *Journal of Materials Processing Technology*. 226: 50-59.

brittle, ferrous-based phase was imaged and the amount of ferrous impurities in 3-D printed aluminum was measured. These results thus provide methods with the removal of metal 3-D printed parts from print substrates with no specialized tooling or equipment conducive to distributed manufacturing.

3.2 Introduction

Additive manufacturing, commonly known as 3-D printing, has progressed beyond prototyping and tooling (Sachs et al. 1992) and is now changing the state of manufacturing across the globe (Campbell et al., 2011). This type of manufacturing is already being used to produce functional components for custom biomedical implants, dental prostheses, non-structural aircraft components, custom tooling, and thousands of customized consumer parts such as jewelry, sculptures, phone cases, and more (Wohlers & Caffrey, 2014). The ability to quickly model, change, and print designs makes manufacturing possible in small or large quantities, including end-user manufacturing on a micro-scale (Wittbrodt et al., 2013) and the associated social change (Ratto and Ree, 2012).

Traditional metal printing methods utilizing sintering, typically with laser or electron beam sources, are expensive due to the high capital and operating cost of the 3-D printing equipment employed. For instance, Berman (2012) stated that industrial-grade printers capable of rapid prototyping can cost on the order of hundreds of thousands of dollars; Peels (2014) reported that some direct metal laser sintering machines cost as much as \$1.5 million. Often specialized and expensive facilities are needed to house the equipment (e.g. blast-protected rooms for metal powder printing). Expensive, energy

intensive, and time-consuming methods are then needed to remove metal 3-D printed parts from the substrates such as wire electrical discharge machining (EDM). As a result, additive manufacturing with metal is largely isolated to large corporations possessing the means to equip and maintain these expensive facilities.

Gas metal arc welding (GMAW) may be one low-cost solution to three dimensionally print metals (Anzalone et al., 2013). The GMAW process is described by O'Brien (1991) and Holliday (1993). GMAW utilizes a gas-shielded metal wire fed through a nozzle that is a consumable electrode heated by an electrical arc established between the wire and a metallic substrate. This arc melts the electrode and a portion of the weld substrate, depositing metal into the substrate's weld pool. The gas shield protects the hot metal from atmospheric gases and humidity that can cause porosity or oxidation. The composition of the gas shield mixtures can be tuned to modify weld pool geometry, penetration, and porosity while also stabilizing the arc and minimizing weld spatter (Holliday, 1993). For instance, helium additions to the argon gas in aluminum welding yields a more uniform weld pool geometry with less porosity at the expense of lower arc stability and more weld spatter (O'Brien, 1991).

The GMAW-based open-source design for a 3-D printer by Anzalone et al. (2013) was inspired by a Rostock RepRap printer, (a self-replicating rapid prototyper (Jones et al., 2011)); the printer features a 3-axis stage upon which the print substrate is clamped (Reprap Org, 2014). A stationary weld gun is the print head which delivers material to the substrate, with a common GMAW welder is used to print layers in a single-pass,

multi-layer regime. This printer is capable of printing both aluminum and steel alloys to produce near net-shape parts.

As O'Brien (1991) and Holliday (1993) describe, welding shield gases are essential to forming a strong weld joint in GMAW. However, the formation of a strong, weld-like joint between a 3-D printed metal part and a metallic substrate is undesirable. Strong adhesion between the part and the substrate makes separation of the part from the substrate more difficult and the substrate must be sacrificed so it can only be used once. It is desirable to 3-D print a metal part onto a metal substrate, remove the part with little force, and have the ability to re-use the substrate with minimal post-print processing.

A previous study explored the use of coatings, such as oxides and nitrides, and welding of dissimilar metals to prevent adhesion between the 3-D printed metal part and the substrate (Haselhuhn et al., 2014). Nitride coatings and printing aluminum on steel substrates were shown to be effective at minimizing part-substrate adhesion with aluminum parts. In this paper, this preliminary work has been further analyzed, extended to steel printing, and new substrate release mechanisms such as omission of shield gas and application of alternate coatings are explored (Table 3.1). Steel was not printed on an aluminum substrate as this resulted in significant melting of the aluminum substrate in preliminary work.

Table 3.1 Substrate Release Mechanisms Analyzed by this Study

Mechanism	Print Material	Substrate Type	Coating Type	Coating Thickness (µm)	Shield Gas Use 1st Layer
Control	ER70S-6	A36 Low Carbon Steel	None	0	25% CO2 in Argon
	ER4043	1100 Aluminum	None	0	Argon
Alternate Settings	ER70S-6	A36 Low Carbon Steel	None	0	None
	ER4043	1100 Aluminum	None	0	None
Intermetallics	ER4043	A36 Low Carbon Steel	None	0	Argon
Coatings	ER4043	1100 Aluminum	Aluminum Oxide	18.50	Argon
	ER4043	1100 Aluminum	Boron Nitride	5.95	Argon
	ER4043	1100 Aluminum	Titanium Nitride	6.25	Argon

The development of these substrate release mechanisms is described in depth and evaluated in terms of their efficacy and practicality with both aluminum and steel parts. The strength of adhesion was evaluated using modified Charpy impact testing. The sample porosity, microstructures, hardness, and ultrasonic modulus were analyzed to evaluate 3-D printed part quality.

3.3 Hypothesis

If substrate release mechanisms are employed, then impact energy required to remove a 3-D printed metal specimen from a metal substrate will be reduced allowing for sample removal by hand, because weld penetration into the metal substrate will be limited.

3.4 Materials & Methods

3.4.1 Description of the Metal 3-D Printer

The 3-D metal printer and open-source software tool chain used in this study has been previously described (Chapter 2; Haselhuhn et al., 2014) (Figure 3.1). A Millermatic 140 with an M-100 weld gun was used to print steel parts whereas aluminum parts were printed with a Miller Spoolmate 100 weld gun. The weld gun remained stationary while a computer numeric controlled 3-axis stage provided the necessary motion to 3-D print a metal part. Welder and printer settings were manually adjusted to achieve high-quality prints with a maximum print diameter of approximately 80 mm. Weld-grade argon shield gas was used during aluminum printing and RC25, a typical steel weld-gas mixture of 25% CO₂ in argon, was used as a cover gas for steel printing.

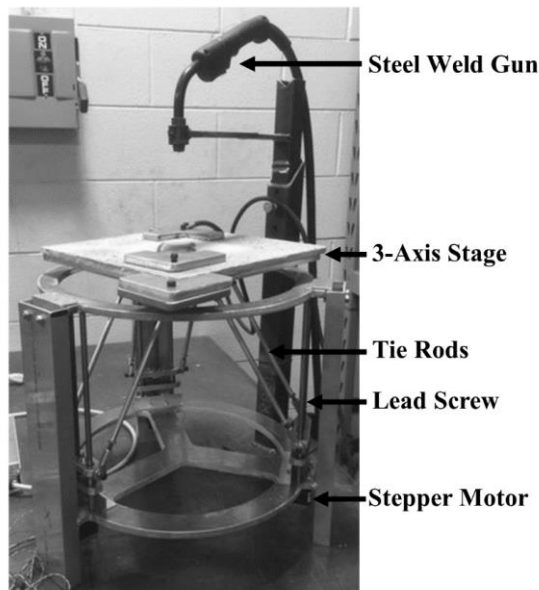


Figure 3.1 Labeled photograph of the GMAW-based metal 3-D printer shown with the M-100 weld gun for steel printing

3.4.2 Preparation of Print Substrates

Degreased 1100 aluminum and ASTM A36 low carbon steel sheets, 152.4 x 152.4 x 6.35 mm in size, were used as print substrates. Aerosol-based aluminum oxide, boron nitride, and titanium nitride coatings (ZYP Coatings, Inc.) were evenly sprayed onto separate 1100 aluminum substrates prior to printing (Table 3.1). The coatings were smooth and geometrically uniform to prevent dimensional variation that could distort layer and part geometries. The thickest possible coating was applied that would still allow a weld arc to form between the weld gun and the print substrate. At coating thicknesses in excess of those reported, the welder could not produce a stable arc and welding did not occur. The coatings were allowed to dry completely in ambient air prior to printing. Samples were weighed before ($W_{initial}$) and after (W_{final}) application of the coating and coating thickness was calculated based upon the average coating weight across the surface area (SA) of the substrate given a known coating density ($\rho_{coating}$) (Equation 3.1).

$$Thickness = \frac{W_{final} - W_{initial}}{\rho_{coating} * SA} \quad (3.1)$$

A subset of aluminum substrates was left in the uncoated state to serve as controls. Coatings were not applied to steel substrates as preliminary work indicated that they did not survive the steel welding environment. Five samples per treatment condition were prepared.

3.4.3 Printing of Samples

Standard ER4043 aluminum GMAW wire (Blue Demon Welding Products), 0.030 inches (0.762 mm) in diameter, and standard ER70S-6 low carbon steel GMAW

wire (Hobart), 0.023 inches (0.584 mm) in diameter were used as the print material. One inch (25.4 mm) cube samples were printed directly onto the center of the prepared substrates (Table 3.2; Figure 3.2).

Table 3.2 3-D Metal Print Parameters Used to Produce 1" Cubes

Print Mat'l	Method	Weld Voltage V	Weld Current A	Wire Feed Rate mm/s	Print Speed mm/s	Wire Stick-Out mm	Gas	Gas Flow Rate L/s
ER70S-6	Control Alternate Settings: 2 nd -15 th Layers	16	76	25.4	5.23	8	RC25	0.13
	Alternate Settings: 1 st Layer Only	14	65	33.9	5.23	11	None	0.00
ER4043	All Methods ^a	15	72	38.1	15.00	14	Ar	0.22

^aShield gas was not used to print the 1st layer of some samples, as described in Table 3.1.

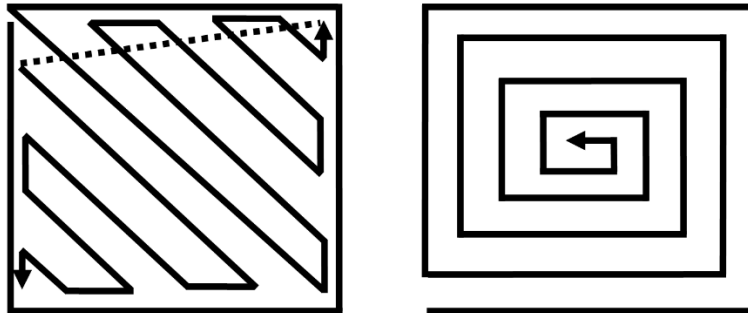


Figure 3.2 Alternating print paths for the 3-D metal printer as viewed in the direction of the z-axis. The lines in this schematic only represent the print paths taken by the printer and the print was a solid part. The starting point for each layer alternated between the cube's four corners.

Alternating the print path between layers improved the in-fill between weld beads improving overall print quality. A 60 second pause was applied between each layer when printing with aluminum. A similar approach was applied when printing steel cubes with a 10 minute pause after the first layer, 60 second pauses after the 3rd and 5th layers, followed by 2 minute pauses after every other subsequent layer. These pauses were performed to allow the sample to cool sufficiently to maintain dimensional tolerance and also to prevent the welder from overheating. Allowing the first steel layer to cool completely before printing additional layers was found in preliminary experiments to reduce the energy required to remove the part from the substrate. Each specimen was water quenched immediately following print completion. Five samples were printed per group and their final dimensions were measured with digital calipers (± 0.01 mm).

3.4.4 Sample Testing & Analysis

The impact strength of each sample-substrate interface was tested using a modified Charpy impact tester (Tinius Olsen) (Figure 3.3). This modified test apparatus removed the entire 3-D printed specimen from the print substrate and did not shear off any of the printed layers. A standard 1 lb (0.45 kg) claw hammer head was used as the striker rather than the traditional wedge striker to simulate the effects of removing the sample from the substrate using a standard hammer by hand. However, as the weight of the hammer head was much smaller than a typical striker arm used with Charpy impact testing, the weight of the pivot arm was not negligible and was included in the calculation as a friction term (Equation 3.2).

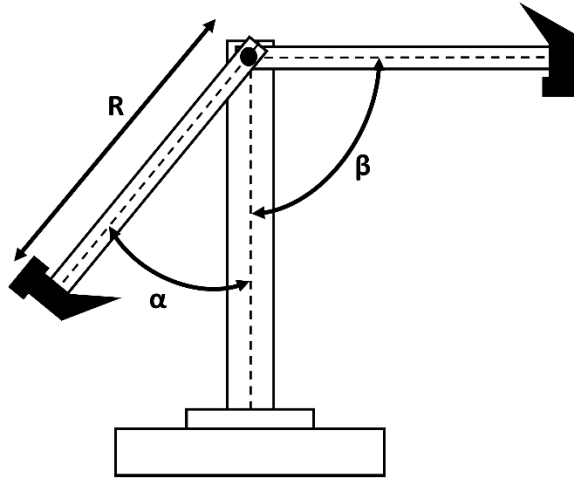


Figure 3.3 Schematic diagram of the modified Charpy impact tester

Samples were securely wedged into place to avoid displacement during testing. The pivot arm was initially set to an angle of 90 degrees from vertical and released in a consistent manner using a lever mechanism. The pivot arm rotated about a fixed axis that only allowed in-line swing. The striking face of the hammer head was approximately the same size as the 3-D printed specimens and the specimens were situated vertically in the test apparatus such that the hammer squarely struck the specimens at or near the specimen center point. The clearance between the hammer and the substrate was less than 3 millimeters. A high speed camera was used to capture images of the pendulum during and after striking the sample. Using NIH ImageJ software (Rasband, 2014), the maximum angle of the pivot arm after hitting the sample was measured. Knowing the mass of the pendulum (m), acceleration due to gravity (g), length of pivot arm to the center of hammer mass (R), the initial, stationary angle of the pendulum (β), the final angle of the pendulum (α) following impact, and the energy loss associated with friction

(E_f), the impact energy (E_i) was calculated (Equation 3.2). In a frictionless system, the initial and final angles would be equivalent. However, when the mass of the pendulum is low, friction can play a significant role in the final results. The frictional energy loss was determined by releasing the pendulum from a known initial angle without a specimen in the sample holder, measuring the final angle of the pendulum, and calculating an associated energy using the first half of Equation 3.2 in square brackets. Any specimens not removed by the Charpy impact were physically removed with a water cooled horizontal band saw for additional analysis.

$$E_i = [mgR(\cos \alpha - \cos \beta)] - E_f \quad (3.2)$$

Following Charpy impact testing, the porosity in the cube specimens was measured using the Archimedes Principle, following ASTM B962, “*Standard Test Methods for Density of Compacted or Sintered Powder Metallurgy (PM) Products Using Archimedes’ Principle*” (2013). This measurement compares the weight of the specimen dry (W_{dry}) and when submerged in water ($W_{submerged}$) using a temperature corrected density ($\rho_{water(T)}$) to determine density (ρ_{sample}) (Equation 3.3).

$$\rho_{sample} = \frac{W_{dry}}{W_{dry} - W_{submerged}} * \rho_{water(T)} \quad (3.3)$$

To measure the submerged weight of the sample, each sample was placed in distilled water and ultrasonically agitated prior to measurement. This agitation was performed to fill any open porosity, ensuring that only closed porosity influenced the final porosity measurement. By comparing the density of the specimen to a known

standard density for the weld alloy (ρ_{standard}), the specimen porosity (% Porosity) was calculated (Equation 3.4).

$$\% \text{ Porosity} = \frac{\rho_{\text{standard}} - \rho_{\text{sample}}}{\rho_{\text{standard}}} * 100\% \quad (3.4)$$

A representative specimen from each group was sectioned twice using a slow speed diamond saw: once along the x-axis and once along the y-axis to produce 4 rectangular specimens each approximately 12.7 x 12.7 x 25.4 mm in size. The specimens were vacuum impregnated with fluorescent epoxy to fill micro-cracks, porosity, or regions with poor infill between the weld beads. This fluorescent epoxy improved detection of smaller features in the microscope and also facilitated later polishing processes as it minimized the risk of collecting grinding media in the voids which would later scratch the polished surface. Aluminum samples were polished to 0.05 μm with silica whereas the steel specimens were polished to 0.05 μm with alumina. To enhance the microstructural features for microscopy work, the aluminum specimens were etched for 30 seconds in Keller's etchant whereas the steel specimens were etched with 2% nital solution for approximately 10 seconds.

The specimens were examined in a standard optical microscope and also in a Philips XL40 environmental scanning electron microscope in order to observe the microstructural features. Energy dispersive spectroscopy (EDS) was performed with particular emphasis near the interface between the print substrate and the first layer of the specimen to determine if any inclusions (oxides, nitrides, or aluminum-iron intermetallics) formed or if segregation of these compounds occurred within the

specimen. EDS analyses were performed at 25 keV accelerating voltage with a spot size of 6 and a collection time of 100 live time seconds. The goal was to determine the mechanism by which adhesion strength was minimized by these adhesion modifiers and/or by minimal first layer weld penetration.

Vickers hardness values were measured at 1 millimeter increments across the 3-D printed cube along the lines depicted in Figure 3.4.

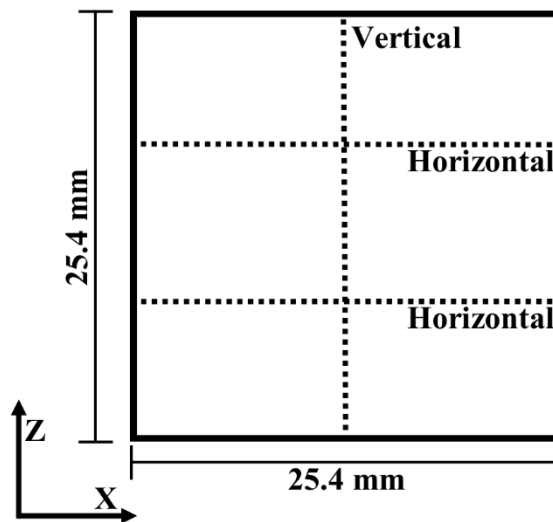


Figure 3.4 Schematic diagram describing lines along which hardness measurements were taken

A diamond indenter with 50 gmf and a 10 second dwell time was used to measure macro-hardness to evaluate hardness changes throughout the cube result resulting from process parameters. These test parameters were unlikely to detect the effects of thin interlayer or interfacial compounds present in the specimen. Any bulk compounds that may have formed in the first layer in situ, such as oxides and intermetallics, may affect the hardness

of the material. Re-melting of layers that occurred as a result of the welding process can cause these compounds to mix and be dispersed among subsequent layers.

An additional representative specimen from each treatment group was used to measure ultrasonic modulus. This type of test was non-destructive and did not produce fracture surfaces. The top and bottom surfaces of the cube specimens were cut to be parallel with one another and polished to 600 grit with silicon carbide in order to provide a good interface for the transducers. An Olympus Panametrics Pulser Receiver 5052PR was used to measure both the transverse and longitudinal elastic wave velocities in the vertical direction of the specimen. A 2.25 GHz transducer with a molasses couplant was used to induce and measure transverse waves within the specimen whereas a 5 GHz transducer with Panametrics Ultrasonic Couplant D Gel was used to induce and measure longitudinal waves within the specimen. Poisson's ratio (ν) was calculated from the transverse velocity (V_T) and longitudinal velocity (V_L) according to Equation 3.5 (Krautkrämer and Krautkrämer, 1990).

$$\nu = \frac{1-2\left(\frac{V_T}{V_L}\right)^2}{2-2\left(\frac{V_T}{V_L}\right)^2} \quad (3.5)$$

Using this calculated value, the longitudinal velocity, and the measured specimen density (ρ) from the previous Archimedes density measurement (Equation 3.3), Young's modulus of the material (E) was calculated (Equation 3.6).

$$E = V_L^2 \rho \frac{(1+\nu)(1-2\nu)}{1-\nu} \quad (3.6)$$

The shear modulus (G) was a function of the transverse velocity and the specimen density (Equation 3.7).

$$G = V_T^2 \rho \quad (3.7)$$

3.5 Results

3.5.1 Dimensional Validation & 3-D Printed Part Inspection

The print parameters employed produced specimens with good dimensional tolerances. The aluminum cubes averaged $28.3 \times 28.3 \times 27.7$ mm in size (± 0.9 mm) whereas the steel cubes averaged $26.3 \times 26.1 \times 26.3$ mm in size (± 0.5 mm). Less dimensional variation was observed in the steel specimens than the aluminum specimens. No warping of the substrate or the printed part was observed during printing or after specimen removal. In many instances, such as parts produced without shield gas for the first layer, the print substrate surface was almost completely unaffected by the welding process. Upon subsequent cleaning with a degreasing agent, the underlying metal was clean, glossy, and could be reused. The surface topology of the bottom surface of the cube (the face in contact with print substrate) varied significantly based upon the mechanism studied (Figure 3.5). Aluminum specimen A and steel specimen B in Figure 3.5 were printed without shield gas for the first layer with specimen B printed at different welder settings. This treatment resulted in the smoothest interface compared with aluminum specimens C and D, which employed the use of intermetallic formation and ceramic coatings, respectively. Representative images for steel and aluminum specimens

produced in the control group were not imaged as these specimens could only be removed from the substrate by cutting them off.

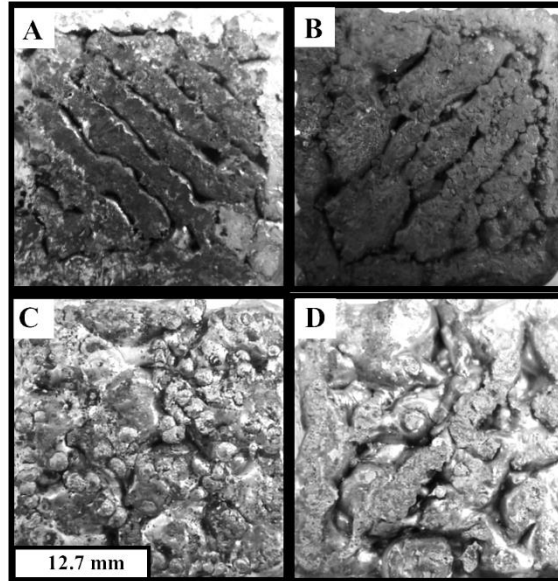


Figure 3.5 Macro images of the interface between the 3-D printed part and the substrate. A: Aluminum, no shield gas used for the 1st layer, B: Steel, no shield gas used for the 1st layer, C: Aluminum-iron intermetallics, D: Coated aluminum.

3.5.2 Specimen-Substrate Impact Energy

All specimens, barring the steel and aluminum control group specimens, were readily removed by the Charpy apparatus (Figure 3.6). Representative specimens from each specimen could also be removed from the substrate either by hand or with minimal assistance from a handheld 1 lb hammer. As previously mentioned, both the aluminum and steel specimens printed in the control group without any adhesion modifiers could not be removed from the substrate by the test apparatus. In fact, these specimens could

not be removed from the substrate even when the hammer type was changed to a 5 lb sledgehammer (approximately 40 J of applied impact energy). These specimens could only be removed from the substrate by cutting, in this case with a horizontal band saw. Although the aluminum and steel specimens printed without first-layer shield gas could be readily removed, they required more energy than other substrate release mechanisms (with aluminum being the highest). Aluminum printed on steel, (intermetallic formation), required the least amount of energy to remove. Although coatings all enabled low-energy release, there was no statistical difference in removal energy between the coating types on aluminum substrates.

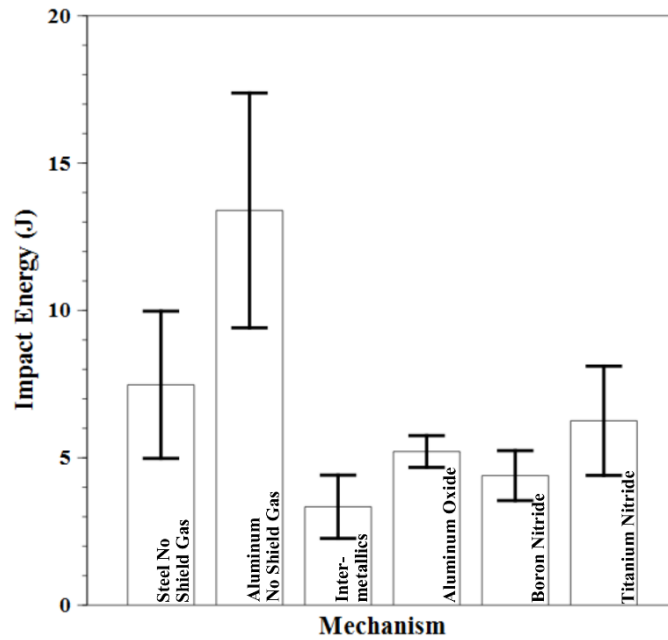


Figure 3.6 Impact energy required to remove 3-D printed specimens from a print substrate based upon substrate release mechanism employed. Error bars represent ± 2 standard error (95% confidence interval).

3.5.3 Specimen Porosity

All samples had less than 5% porosity (>95% dense) (Figure 3.7). Overall, the porosity of the steel specimens was less than that of the aluminum specimens. The control group porosity was less than those produced with no shield gas for the first layer. This trend was statistically significant with the steel specimens but not the aluminum specimens. The porosity of aluminum on a steel substrate (intermetallic formation) was significantly less than aluminum specimens with other substrate release mechanisms. This porosity may appear lower due to the presence of dense iron-containing compounds into the aluminum part and as further evaluated in the microstructural analysis. There was no statistical difference in aluminum specimen porosity based upon ceramic coating type.

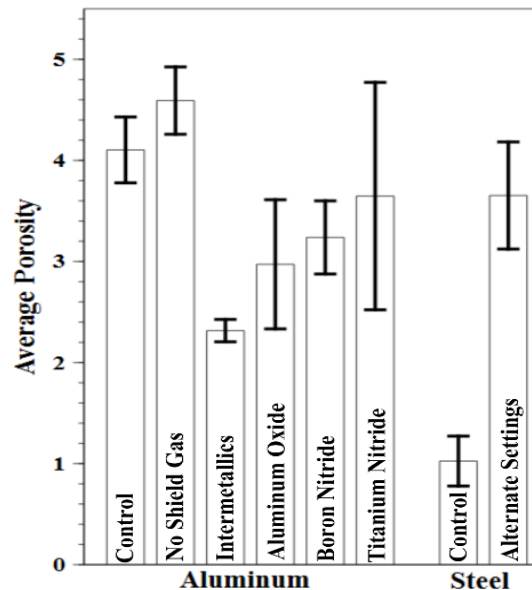


Figure 3.7 Average specimen porosity measured via the Archimedes method: Aluminum samples (left) and steel samples (right). Error bars represent ± 2 standard error (95% confidence interval).

3.5.4 Specimen Microstructure

Optical microscopy revealed a banded microstructure in both the aluminum and steel specimens (Figure 3.8), although this texture was more prevalent in the aluminum specimens. These regions were composed of bands having smaller microstructural features, such as dendrites in aluminum and grain boundaries in steel, sandwiched between bands with larger microstructural features. These banded regions also varied from one another in terms of feature orientation, such as dendritic cell orientation within the aluminum specimens. Banded regions formed due to the unique thermal cycles associated with GMAW wherein portions of the previous layer are re-melted when a new layer is welded onto the part. The layers did not perfectly coincide with each print layer and there was a slight curvature to the banded regions at the specimen edges, presumably due to a faster cooling rate. The steel specimens were dominated by polygonal ferrite near the center, with the polygonal ferrite transitioning to acicular ferrite near the edges and interfaces where faster cooling rates dominated. The polygonal ferrite was banded, similar to the aluminum specimens, although less pronounced.

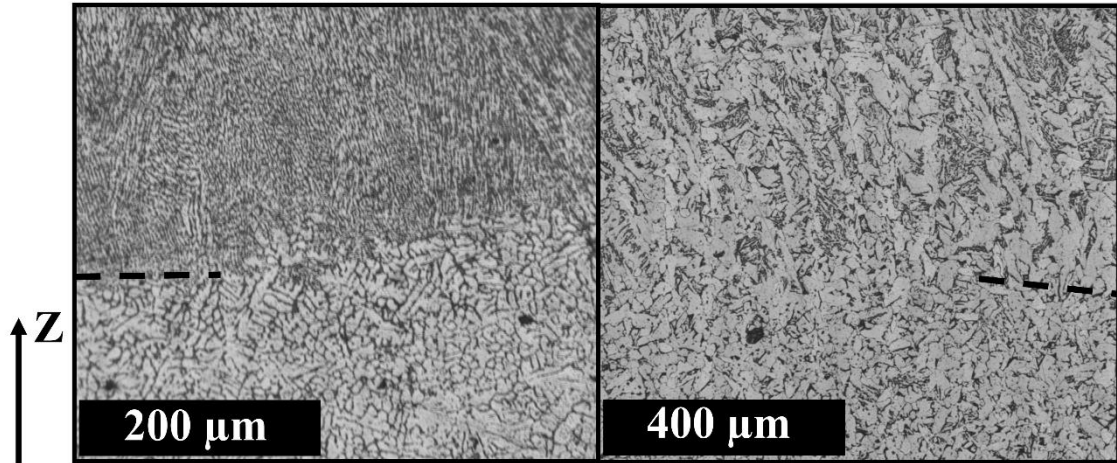


Figure 3.8 Representative 3-D printed microstructures. Aluminum shown at left and steel shown at right. Lines added to the figures indicate where boundaries exist.

Directional cooling occurred in the +Z direction.

The microstructural images of aluminum and steel specimens control group showed the alloy without any inclusions or defects. Specimens produced without first layer shield gas exhibited a disproportionate amount of porosity in the first layer as compared to the rest of the specimen. As subsequent layers were printed with the benefit of shield gas, this phenomenon did not reappear. Some oxides were visible by direct observation on the bottom surface of both the aluminum and steel specimens, but these could not be confirmed with EDS.

For aluminum printed on steel (intermetallic formation) an iron gradient was observed within the first 10 microns of the interface with the substrate (Figure 3.9). The densest layer closest to the part-substrate interface was the most iron rich with approximately 32% iron. This iron rich layer yielded to a second layer with lower iron

concentration further into the sample specimen, yet still within the first 3-D printed layer. EDS analysis could not detect iron beyond these two layers. Structural analyses were not performed on these layers to determine their chemical structure. The aluminum specimens printed on ceramic coated aluminum substrates had similar macrostructures to those prepared by without first layer shield gas. However, many of these specimens exhibited small ceramic coating particles mixed within the first few millimeters of the specimen.

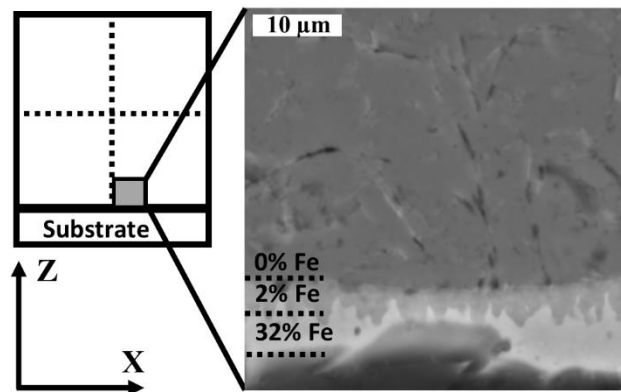


Figure 3.9 Scanning electron images of aluminum specimens printed on steel near the specimen center. White and lighter colored layers correspond to phases rich in iron.

3.5.5 Specimen Hardness

For both printed aluminum and steel, more variation in hardness was observed in the vertical direction than in the horizontal direction (Figure 3.10). No significant long range trends were observed in the hardness measurements of the aluminum specimens. There are many short range increases and decreases in the hardness values that are related to the print layer interval. In aluminum, harder regions corresponded to microstructural

regions with smaller dendrite sizes whereas softer regions corresponded to microstructural regions with larger dendrite sizes. A similar trend was exhibited in steel with harder regions corresponding to smaller grain structures. Additionally, the hardness of the steel specimens increased near the specimen edges where acicular ferrite was dominant.

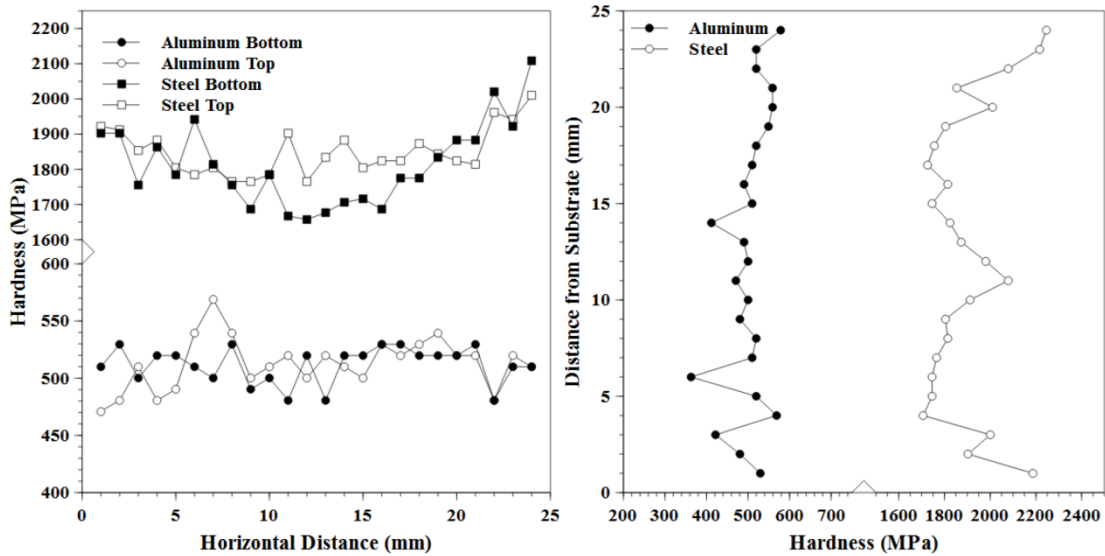


Figure 3.10 *Representative hardness profiles. Horizontal profiles for aluminum and steel (left) and vertical profiles (right). The aluminum specimen was printed on boron nitride coated aluminum whereas the steel specimen was printed with alternate settings for the first layer.*

3.5.6 Ultrasonic Modulus

There was a significant difference in both the elastic and shear moduli based upon the substrate release mechanism utilized and this phenomenon was more pronounced in aluminum than steel (Figure 3.11). The aluminum and steel moduli were significantly

lower for the specimens produced without shield gas and alternate settings for the first layer compared with the control group specimens. Both the elastic and shear moduli of the aluminum specimen printed on steel were larger than both the aluminum specimen printed without shield gas and the aluminum specimen printed on coated substrates. However, the aluminum specimen printed on steel exhibited a smaller elastic and shear modulus compared to the aluminum control group. There was no statistical difference between the moduli of aluminum specimens printed on boron nitride and titanium nitride and these moduli were larger than the moduli of aluminum specimens printed on aluminum oxide. The elastic modulus of the aluminum specimens was approximately 71 GPa whereas the elastic modulus of the steel specimens was approximately 208 GPa. The shear modulus of the aluminum specimens was on the order of 27 GPa whereas for steel this value was approximately 80 GPa.

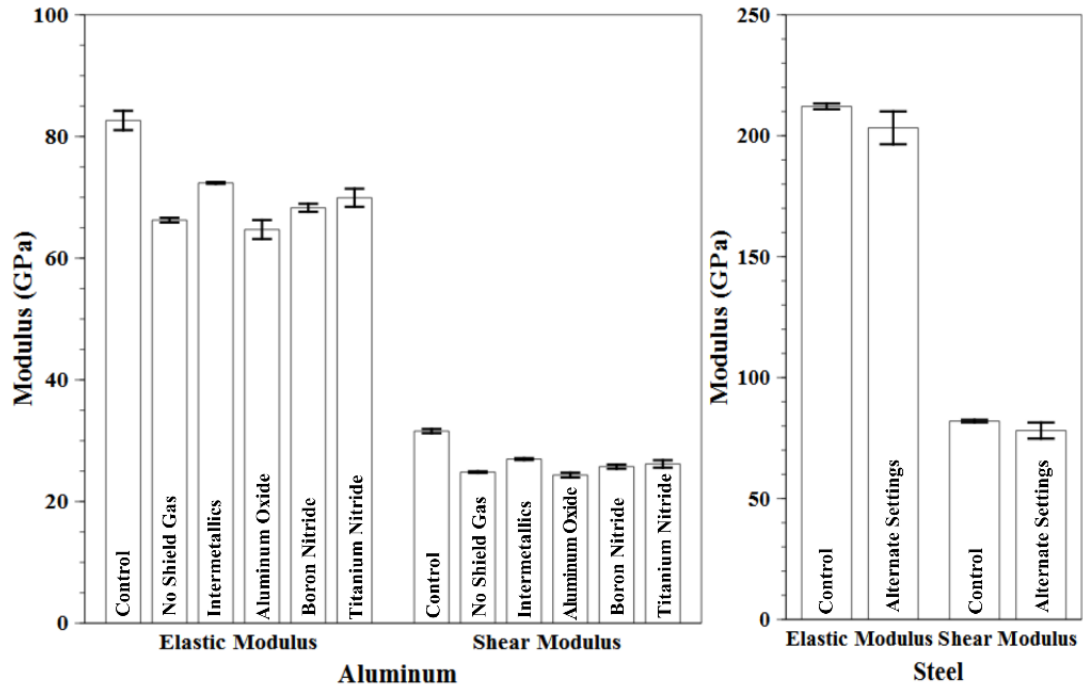


Figure 3.11 Elastic and shear moduli of 3-D printed specimens. Aluminum (left) and steel (right). Error bars represent ± 2 standard error (95% confidence interval).

3.6 Discussion

Steel print resolution was superior to that of aluminum. The lower viscosity of molten aluminum allows it to spread, influencing the final dimensions of the part. Liquid metal viscosity can be controlled by alloying additions to improve print resolution.

For the control settings, no atmospheric reactions were encouraged to produce oxides or materials added to limited weld penetration into the substrate. Therefore, a strong bond formed between the 3-D printed part and the substrate. These parts were compositionally homogeneous compared with parts printed via other substrate release mechanisms with no intermetallics, oxides, or ceramic particles dispersed throughout the

specimen. These parts exhibited microstructures as shown in Figure 3.8 and hardness as shown in Figure 3.10. Both the steel and aluminum control specimens were harder than parts produced with the proposed substrate release mechanisms. As these specimens had to be cut from the substrate, any interface defects were removed.

With 95% confidence, the p-value was calculated to be less than 0.05. Thus the null hypothesis could be rejected and the alternative hypothesis was accepted. A combination of effects allowed specimens produced without first layer shield gas and alternate settings to be easily removed from the substrate. Allowing the first steel layer to cool completely before printing additional layers was found in preliminary experiments to reduce the energy required to remove the part from the substrate. With steel, less weld power was used and more weld material was deposited while printing the first layer. For both aluminum and steel, while some oxides may have formed as a result of no shield gas use, arc stability was reduced which prevented weld bead penetration into the substrate. The melted weld wire had little interaction with the substrate thus forming a weak bond. Iron oxide and aluminum oxide compounds were visually observed on the bottom surface of the steel and aluminum specimens respectively. Without the use of shield gas there was nothing to inhibit the hot weld material from reacting with ambient air. The hot metal reacted with moisture and oxygen in the atmosphere. The moisture decomposed into hydrogen gas that was more soluble in the molten metal than in the solid metal. This solubility gap allowed hydrogen bubbles to nucleate upon directional solidification forming elongated pores that were not present elsewhere in the sample. Compared to steel, this type of porosity was more pronounced in aluminum given its sensitivity to

hydrogen porosity. Printing without first layer shield gas produced more porous specimens than those printed with other substrate release mechanisms, regardless of material. The significantly higher porosity in the steel specimen likely caused the strengths of these specimens to be lower than those produced in the control group. A porosity gradient was not observed within the printed specimens and significant diffusion of porosity in subsequently printed layers was not expected. A similar penetration limit may be achievable by shifting the 3-D printing transfer mode to spray rather than short-circuit as spray transfer is also used to weld thin sections of metal (Table 1.1.). This may be achieved by significantly increasing weld current while using argon shield gas to limit the formation of porosity and oxides.

The aluminum specimen printed on steel behaved similarly to aluminum printed without first layer shield gas. However, aluminum printed on steel exhibited less weld penetration and the aluminum did not wet the steel substrate as well. This produced a rougher surface texture at the interface between the first layer and the print substrate as compared to parts produced without first layer shield gas. Taban et al. (2010) and Pasic et al (2007) described the difficulty of joining aluminum and steel by traditional welding methods. It was expected that if a joint formed, aluminum would form a very weak interface dominated by the formation of aluminum iron intermetallics (Taban, et al. 2010). These intermetallics form due to the significant chemical, physical, and geometric differences between aluminum and iron (Pasic, et al. 2007). An iron composition gradient was observed over the first ten microns of the aluminum specimens printed on steel substrates, with as much as 32% iron in the aluminum directly adjacent to the steel

substrate (Figure 3.8). Aluminum iron intermetallics comprised of approximately 33% iron have been defined by Pasic et al as being of the FeAl_2 type (2007). As iron is denser than aluminum, the iron-rich layers likely decreased the apparent porosity of these specimens, and may have artificially increased the moduli of these specimens.

The direct application of oxides and nitrides to the surface was expected to limit weld penetration by forming a barrier between the substrate and the weld material. There was little statistical difference in part quality or impact energy required to remove the specimen from the substrate based upon the type of ceramic coating used. The use of aluminum oxide with a chemical binder appeared to work well to prevent adhesion between the print material and the substrate as proposed by Haselhuhn et al. (2014). Compositional analysis of the specimens indicated that some of the coating particles may have been dislodged from the substrate by the welding process, with these particles being mixed within the first two millimeters above the substrate.

The elastic and shear moduli of all specimens agree well with those reported in the literature (Table 3.3).

Table 3.3 Aluminum and Steel Modulus Values as Reported in the Literature

Material	Elastic Modulus (GPa)	Shear Modulus (GPa)	Reference
Al – 5% Si	71	26.2	Gale & Totemeier (2003)
ER4043 Al	71	27	<i>This study</i>
ER4043 Al	66.4	-	<i>Predicted</i>
Mild Steel	208-209	81-82	Gale & Totemeier (2003)
Low Carbon Steel	207.1	-	Wolfenden & Schwanz (1995)
ER70S-6 Steel	208	80	<i>This study</i>
ER70S-6 Steel	198.9	-	<i>Predicted</i>

The predicted elastic modulus of ER4043 and ER70S-6 based upon average porosity levels were calculated according to an equation developed by Wachtman and MacKenzie (Equation 3.8) in which E_0 is the theoretical Young’s modulus for an alloy and p is the amount of porosity (Meyers & Chawla, 2009).

$$E = E_0(1 - 1.9p + 0.9p^2) \quad (3.8)$$

The predicted values of elastic modulus were similar to those shown in Figure 3.11 for both steel and aluminum. Modulus measurements via ultrasonic methods are sensitive to interfaces and defects within the specimen such as micro porosity. Both macro-porosity, the result of poor in-fill between weld beads, and micro-porosity due to soluble gases, were observed in the specimens. Defects such as micro porosity and poor infill can reduce a material’s moduli by lowering resistance to elastic deformation. Future testing of specimens printed via GMAW-based 3-D metal printing should include tensile and

compression testing to obtain a more thorough understanding of the mechanical properties of printed parts.

Variations in specimen hardness relate directly to local microstructure. As previously described, regions with a finer microstructure had correspondingly higher hardness in both aluminum and steel. While there were no long-range macroscopic trends in aluminum, steel specimens were hardest near edges where acicular ferrite was dominant due to the faster cooling rate. This banded microstructure has been reported by other researchers for 3-D printed metal specimens. Choi et al. (2001) reported a similar banded microstructure in their mild steel parts produced via laser welding and milling. Similarly, a finer grain structure was observed in the center of the weld bead with coarser grain structures dominant at the intersections between weld beads. These banded microstructures correspond to thermal gradients produced as subsequent layers are printed. Any curvature associated with these banded regions is dependent upon the path the printer follows while printing. Knowledge of this effect can be used by designers to develop print paths that optimize microstructure and properties. It may be possible to tailor print methods to deliver part or all of some heat treatment processes.

Printing without first layer shield gas and facilitating aluminum-iron compound formation by printing aluminum on steel substrates were shown to be effective methods for enabling easy removal of printed parts from substrates. These methods were no-cost methods whereas the coatings investigated could be costly, costing upwards of \$200 per aerosol canister. Regardless, all of the methods investigated were much less expensive than cutting parts from their substrates and subsequent post-printing treatment.

All of these methods, however, reduce the total cost of metal 3-D printing into the range accessible to small and medium sized enterprises and businesses. For the first time it makes metal printing in addition to plastic printing (Pearce, et al. 2010) of open source appropriate technologies (Pearce, 2012) and education (Canessa, et al., 2013) viable for sustainable development (King et al., 2014) and for low-cost laboratory supplies (Pearce, 2014). Most notably, the minimal weld penetration allowed all of the print substrates to be reused to print additional parts, although the substrates were not reused in this study. This has significant cost savings potential and it is clear that it qualitatively reduces the environmental impact of 3-D metal printing. Previous work has shown improved constrained sustainability (Reeves, 2009), reduced carbon emissions (Reeves, 2012), reduced environmental impact using 3-D printing for prototyping (Drizo & Pegna, 2006), distributed manufacturing (Kreiger and Pearce, 2013) and global sustainability (Gebler, Uiterkamp, & Visser, 2014) as compared conventional methods of manufacturing in plastic and metal. Future work should consider a full life cycle analysis of GMAW 3-D printing.

Future work should also quantitatively evaluate the residual stresses during GMAW-based metal 3-D printing. In the present study there was no observed accumulation of residual stress in the parts during printing or upon removal from the print substrate, and part distortion did not occur. It is possible that residual stresses assisted in sample removal, although this was not measured in this study. Residual stresses should be minimized within 3-D printed specimens as these stresses may prematurely remove the part from the substrate. This residual stress can also pose a significant issue for 3-D

printed parts produced via laser sintering methods as described by Mercelis and Kruth (2006) and Wu et al. (2014), where they observed that upon cutting the part from the print substrate, the residual stresses caused the part to distort. Mercelis and Kruth (2006) explain that reducing thermal gradients may be critical to also reducing residual stress buildup whereas Wu et al. note that many more factors such as part size and the print time affect the formation of residual stresses (2014). Both in situ heating (Vasinonta et al., 2006) and ex situ annealing steps (Shiomi et al., 2004) have been utilized to reduce residual stresses of 3-D laser sintered parts. The extended thermal cycle associated with GMAW-based 3-D printing may serve as a stress relief treatment that is effective for small parts, such as the cubes printed in this study. Residual stress measurement during printing and cooling can properly evaluate the impact these stresses have upon print quality.

Future work is necessary to determine if these substrate release mechanisms can be applied to other 3-D printing platforms to minimize the amount of energy required to remove a part from the print substrate. Methods that involve ambient atmosphere, would not be suitable for electron beam welding or laser sintering as they may result in dangerous environments or equipment damage. Methods that involve coatings, may be suitable although care should be given to minimize thermal decomposition of coatings and to ensure the thermal decomposition products do not form a combustible atmosphere. The impact of coating roughness and uniformity on metal 3-D printed part geometry may be a greater issue with high-resolution 3-D printing platforms such as electron beam welding and laser sintering. The impact of coating roughness and uniformity could not be

quantified with this GMAW-based metal 3-D printer due to the current resolution limitations of this technology but this should be evaluated in the future. Methods that involve laser sintering or electron beam melting of dissimilar metals, may be most suitable to adoption by other 3-D metal printing platforms. Encouraging the formation of intermetallic compounds, such as by printing ferrous-based or aluminum-based materials on titanium, may allow the specimen to be removed from the substrate with ease. Limiting heat input into the 3-D printed part by reducing current or increasing weld speed may also limit joining of a 3-D printed part and a metallic substrate.

3.7 Conclusions

This study expanded upon previous work on low-cost substrate release mechanisms for GMAW-based 3-D metal printing. No-cost methods were also developed that eliminate the need for coatings: manipulation of first layer weld settings and aluminum-iron compound formation. Print settings, such as printing without shield gas and using alternate weld unit settings for the first layer, were developed to limit weld penetration into the substrate and to encourage in situ formation of release agents such as oxides. Encouraging the formation of aluminum-iron compounds allowed aluminum specimens to be removed from steel substrates with the lowest impact energy. These mechanisms allowed the steel and aluminum specimens to be removed from the substrate without the use of cutting tools. Low-cost methods, such as the use of aluminum oxide, boron nitride, and titanium nitride coatings, were also found to be effective substrate release agents for aluminum 3-D printing as long as a chemical binder was present in the coating solution. These substrate release mechanisms further democratize 3-D printer manufacturing, as

they are suited for consumers as well as small and medium enterprises. In addition to reducing the overall costs of producing 3-D metal parts, these substrate release mechanisms also minimized the waste and concomitant environmental impact associated with 3-D metal printing by yielding substrates suitable for reuse.

3.8 References

Anzalone G.C., Zhang C., Wijnen B., Sanders, P.G., Pearce, J.M. (2013). A low-cost open-source metal 3-D printer. *IEEE Access* 1, 803-810.

ASTM B962-13. Standard Test Methods for Density of Compacted or Sintered Powder Metallurgy (PM) Products Using Archimedes' Principle, ASTM International, West Conshohocken, PA, 2013, www.astm.org.

Berman, B. (2012). 3-D printing: The new industrial revolution. *Business Horizons*, 55, 155-162.

Campbell, T., Williams, C., Ivanova, O., & Garrett, B. (2011). Could 3D printing change the world?. *Technologies, Potential, and Implications of Additive Manufacturing*. Washington, DC: Atlantic Council.

Canessa, E., Fonda, C., & Zennaro, M. (2013). Low--cost 3D printing for science, education and sustainable development. *Low-Cost 3D Printing*, 11.

- Choi, D. S., Lee, S. H., Shin, B. S., Whang, K. H., Song, Y. A., Park, S. H., & Jee, H. S. (2001). Development of a direct metal freeform fabrication technique using CO₂ laser welding and milling technology. *Journal of Materials Processing Technology*, 113(1), 273-279.
- Drizo, A., & Pegna, J. (2006). Environmental impacts of rapid prototyping: an overview of research to date. *Rapid Prototyping Journal*, 12(2), 64-71.
- Gale W.F., and Totemeier, T.C. (Eds.). *Smithells metals reference book*, 8th Ed., Butterworth-Heinemann, 2003, 14:16-15:3.
- Gebler, M., Uiterkamp, A. J. S., & Visser, C. (2014). A global sustainability perspective on 3D printing technologies. *Energy Policy* 74, 158-167.
- Haselhuhn, A.S., Gooding, E.J., Glover, A.G., Anzalone, G.C., Wijnen, B., Sanders, P.G., & Pearce, J.M. (2014). Substrate release mechanisms for gas metal arc weld 3-D aluminum metal printing. *3-D Printing and Additive Manufacturing*, 1(4), 204-209. DOI:10.1089/3dp.2014.0015
- Holliday, D.B. (1993). Gas-Metal Arc Welding. In: Olson, D.L., et al. (Eds.), *ASM Handbook: Welding, Brazing, and Soldering*, vol. 6. ASM International, 180-185.
- Jones, R., Haufe, P., Sells, E., Iravani, P., Olliver, V., Palmer, C., & Bowyer, A. (2011). RepRap—the replicating rapid prototyper. *Robotica*, 29(01), 177-191.

- King, D. L., Babasola, A., Rozario, J., & Pearce, J. M. (2014). Mobile open-source solar-powered 3-D printers for distributed manufacturing in off-grid communities. *Challenges in Sustainability*, 2(1), 18-27.
- Krautkrämer J, & Krautkrämer H. (1990). *Ultrasonic Testing of Materials* (4th ed.). New York: Springer-Verlag.
- Kreiger, M., & Pearce, J. M. (2013). Environmental life cycle analysis of distributed three-dimensional printing and conventional manufacturing of polymer products. *ACS Sustainable Chemistry & Engineering*, 1(12), 1511-1519.
- Mercelis, P., & Kruth, J-P. (2006) Residual stresses in selective laser sintering and selective laser melting. *Rapid Prototyping Journal*, 12(5), 254-265.
- Meyers, M, & Chawla, K. (2009). *Mechanical Behavior of Materials*. 2nd Ed. Cambridge: Cambridge University Press.
- O'Brien R.L., (1991). *Welding Handbook*, 8th Ed., Vol 2. Welding Processes. American Welding Society, Miami, FL, 110-155.
- Pasic, O., Hajro, I., & Hodzic, D. (2007). Welding of dissimilar metals-status requirement, and trend of development. *Welding in the World*, 51(1), 377-384.
- Pearce, J. M., Blair, C. M., Laciak, K. J., Andrews, R., Nosrat, A., & Zelenika-Zovko, I. (2010). 3-D printing of open source appropriate technologies for self-directed sustainable development. *Journal of Sustainable Development*, 3(4), 17-29.

- Pearce, J. M. (2012). The case for open source appropriate technology. *Environment, Development and Sustainability*, 14(3), 425-431.
- Pearce, J. M. (2014). *Open-source lab: How to build your own hardware and reduce research costs*. Elsevier.
- Peels, J. (23 May 2014). Metal 3D printing: From lab to fab. *Inside 3DP*. Retrieved from <http://www.inside3dp.com/metal-3d-printing-lab-fab/>.
- Rasband, W.S., Image J., U.S. National Institutes of Health, Bethesda, Maryland, USA, <http://imagej.nih.gov/ig/>, 1997-2014.
- Ratto, M., & Ree, R. (2012). *Materializing information: 3D printing and social change*. *First Monday*, 17(7).
- Reeves, P. (2009). *Additive manufacturing—A supply chain wide response to economic uncertainty and environmental sustainability*. Econolyst Limited, The Silversmiths, Crown Yard, Wirksworth, Derbyshire, DE4 4ET, UK.
- Reeves, P. (2012). *Example of econolyst research—Understanding the benefits of AM on CO2* Econolyst Ltd., Derbyshire, UK (2012)
<http://www.econolyst.co.uk/resources/documents/files/Presentation%20-%20Nov%202012%20-%20TCT%20conference%20UK%20-%20AM%20and%20carbon%20footprint.pdf>
- Reprap Org. Rostock, <http://reprap.org/wiki/Rostock>, last accessed October 23, 2014.

- Sachs, E., Cima, M., Williams, P., Brancazio, D., & Cornie, J. (1992). Three dimensional printing: rapid tooling and prototypes directly from a CAD model. *Journal of Manufacturing Science and Engineering*, 114(4), 481-488.
- Shiomi, M., Osakada, K., Nakamura, K., Yamashita, T., & Abe, F. (2004). Residual stress within metallic model made by selective laser melting process. *CIRP Annals – Manufacturing Technology*, 51(1), 195-198.
- Taban, E., Gould, J.E., & Lippold, J.C. (2010). Dissimilar friction welding of 6061-T6 aluminum and AISI 1018 steel: Properties and microstructural characterization. *Materials & Design*, 31, 2305-2311.
- Vasinonta, A., Beuth, J.L., & Griffith, M. (2006). Process maps for predicting residual stress and melt pool size in the laser-based fabrication of thin-walled structures. *Journal of Manufacturing Science and Engineering*, 129(1), 101-109.
- Wittbrodt, B. T., Glover, A. G., Laureto, J., Anzalone, G. C., Oppliger, D., Irwin, J. L., & Pearce, J. M. (2013). Life-cycle economic analysis of distributed manufacturing with open-source 3-D printers. *Mechatronics*, 23(6), 713-726.
- Wohlers, T., & Caffrey, T. (2014). *Wohlers Report 2014 Annual Worldwide Progress Report*. Wohlers Associates, Inc. Fort Collins, CO.
- Wolfenden, A., & Schwanz W.R.. (1995). An evaluation of three methods to measure the dynamic elastic modulus of steel. *Journal of Testing and Evaluation*, 23, 176-179.

Wu, A.S., Brown, D.W., Kumar, M., Gallegos, G.F., & King, W.E. (2014). An experimental investigation into additive manufacturing-induced residual stresses in 316L stainless steel. *Metallurgical and Materials Transactions A*, 45(13), 6260-6270.

4 Structure-Properties Relationships of Common Aluminum Weld Alloys Utilized as Feedstock for GMAW-Based 3-D Printing³

4.1 Abstract

The tensile, compressive, and microstructural properties of common aluminum weld filler alloys (ER1100, ER4043, ER4943, ER4047, and ER5356) were evaluated following gas metal arc weld (GMAW)-based metal 3-D printing to identify optimal alloy systems for this type of additive manufacturing. The porosities in all test specimens were found to be less than 2%, with interdendritic shrinkage in 4000 series alloys vs. intergranular shrinkage in 5356. The 4000 series alloys performed better than 1100 and 5356 with respect to printed bead width, porosity, strength, and defect sensitivity. In comparison to standard wrought and weld alloys, the 3-D printed specimens exhibited similar or superior mechanical properties with only minor exceptions. Long print times allow for stress relieving and annealing that improved the print properties of the 4000 series and 5356 alloys. Overall the GMAW-based 3-D parts printed from aluminum

³ The material contained within this chapter has been published in the journal “*Materials Science & Engineering: A.*”

Citation:

A.S. Haselhuhn, M.W. Buhr, B. Wijnen, P.G. Sanders, & J.M. Pearce. (2016). "Structure-Property Relationships of Common Aluminum Weld Alloys Utilized as Feedstock for GMAW-Based 3-D Printing." *Materials Science & Engineering: A*. Submitted.

alloys exhibited similar mechanical properties to those fabricated using more conventional processing techniques.

4.2 Introduction

3-D printing, a type of additive manufacturing, has technically matured, creating rapid growth in applications such as design and prototyping, small-batch production, and distributed manufacturing (Gebhardt, 2003; Gershenfeld, 2005; Wittbrodt, et al., 2013). 3-D printing can be used to fabricate functional components digitally from a computer model that is then sliced into discrete layers and converted into tool paths for the print head. Parts with varying size and complexity can be printed via 3-D printing for a variety of uses such as open source appropriate technologies (OSAT) for sustainable development (Birtchnell & Hoyle, 2014; Pearce, 2010), patterns for cast metal parts (Wohlers & Caffrey, 2014), fuel nozzles for airplane jet engines (Wohlers & Caffrey, 2014), consumer products (Wittbrodt, et al., 2013), scientific equipment (Pearce, 2012; Pearce, 2013), and prototypes for tools and machine inserts (Wohlers, 2014; Pearce, 2012; Pearce, 2013).

3-D printing is commonly used with polymers due to lower capital costs of the equipment, especially with the arrival of open-source self-replicating rapid prototyper (RepRap) 3-D printer designs (Sells, et al., 2009; Jones, et al., 2011; Bowyer, 2014). Metal 3-D printing methods are used industrially and include laser sintering and melting (Laeng, et al., 2000; Lewis & Schlienger, 2000; Santos, et al., 2006; Delgado, et al., 2011) and electron beam melting (Heinl, et al., 2007; Gaytan, et al., 2009; Murr, et al., 2012). These industrial-grade additive manufacturing machines can be prohibitively

expensive; they generally cost more than US\$500,000 and some metal laser sintering machines can cost upwards of US\$1.5 million, beyond the reach of consumers and small and medium sized enterprises (SMEs) (Peels, 2014).

Ribeiro (1998) proposed that metal 3-D printing might be accomplished with industrial robots and welding machines, but very little development in this area took place until recently. By augmenting a RepRap 3-D printer design meant for plastic parts, a low-cost metal 3-D printer utilizing gas metal arc welding (GMAW) technology was developed by Anzalone, et al. (2013), and further developed by Haselhuhn, et al. (2014), which enables SMEs and even individuals to print 3-D objects in metal. This system employs a common GMAW welder and is capable of printing steel and aluminum. Initial work to characterize the porosity, hardness, and ultrasonic moduli of parts produced found mechanical properties similar to the bulk wrought material (Haselhuhn, et al., 2014; Haselhuhn, et al., 2015). Previously, a complete evaluation of mechanical properties has not been reported in the literature for this method of printing. It is important to understand how materials behave when they are 3-D printed as this can guide designs utilizing conventional alloys with GMAW-based metal 3-D printing. This baseline knowledge will also help identify opportunities for improved alloys and processing regimes.

4.3 Background

Much of the traditional welding literature can be directly applied to GMAW-based metal 3-D printing to understand fundamental concepts and behaviors of printed metal parts. 3-D printing via GMAW most closely resembles single-layer, multi-pass

welding, also known as multi-run welding (Easterling, 1983; Lancaster, 1993; Zhao, et al., 2011; Zhao et al., 2012). This type of welding process reheats previously welded material, thus altering the grain structure, which can improve weld mechanical properties such ductility while reducing residual stress (Easterling, 1983; Lancaster, 1993).

Although GMAW-based metal 3-D printing is analogous to single-layer multi-pass welding technology, 3-D printing with this technology requires special considerations since the weld material comprises the entire part, rather than a small portion (Zhao, et al., 2011). This results in a unique distribution of thermal stresses, microstructures, and mechanical properties as a function of process parameters and part geometry.

Aluminum alloys that are commonly used as weld filler material include ER1100, ER4043, ER4047, and ER5356 (Table 4.1).

Table 4.1 Common Aluminum Weld Alloys

Alloy	Main Alloying Element	Commonly Used to Join:
ER1100 ^a	None; $\geq 99\%$ Al	1xxx series alloys, 3003/3004 Al alloys
ER4043 ^b	4.5-6% Si	1xxx series alloys, 2xxx series alloys, 3003/3004 Al alloys, 6xxx series alloys
ER4943 ^b	5-6% Si + 0.3-0.5% Mg	1xxx, 3xxx, 5xxx with less than 3.0% Mg, and 6xxx series alloys.
ER4047 ^a	11-13% Si	6xxx series alloys
ER5356 ^b	4.5-5.5% Mg	5xxx series alloys, 6xxx series alloys, 7xxx series alloys

^a Alcotec Wire Corporation, 2016

^b Hobart Brothers Company, 2016

ER4943 is a newly developed aluminum welding alloy based from the ER4043 alloy system (Anderson, 2011). Dilution of weld filler materials in the weld is typically

anticipated to prevent weld cracking and to produce desired mechanical and electrochemical properties with the exception of ER4943 which was designed to negate the requirement of dilution (Martukanitz, 1993). However, in GMAW-based metal 3-D printing, there is only one material and alloy dilution does not occur. It is important to characterize how common aluminum weld alloys behave in the GMAW-based 3-D printing environment in order to adjust 3-D printing processes on a per-alloy basis, and to guide future alloy development. By printing all materials at the same settings it is straightforward to determine which alloys would benefit from more heat input, faster print speeds, etc.

Heard, et al., analyzed microstructure and fatigue life properties of ER4047 specimens produced via GMAW-based 3-D printing (2012). They observed dendrite arm spacing of 3.5 μ m in the first layer which coarsened to 6.6 μ m in the fourth layer as heat accumulated in the print substrate. Heart, et al., also observed flexural strengths of 3-D printed samples comparable to their cast counterparts. This paper compares to the work of Heard, et al., and extends it to additional aluminum alloys, ER1100, ER4043, ER4943, and ER5356, and evaluates the structure-properties relationships associated with GMAW-based metal 3-D printing of aluminum. In order to understand and design for thermodynamic environment and resulting material properties that arise in the unique welding environment associated with GMAW-based metal 3-D printing, this study evaluates specimen mechanical properties in both compression and tension and also with respect to different print orientations. Microstructural analysis, such as dendrite arm

spacing analysis, was also performed on the printed specimens and the fracture surfaces were evaluated.

4.4 Hypotheses

Hypothesis 1: If weld alloys contain alloying additions such as magnesium, then they will exhibit greater 3-D printed porosity, because magnesium has a high affinity for hydrogen and easily oxidizes, creating nucleation sites for porosity.

Hypothesis 2: If test specimens are oriented within few layers as opposed to across many layers, then the mechanical properties will improve resulting in increased strength and ductility, because defects concentrated at layer boundaries could act as stress concentrators limiting mechanical properties.

Hypothesis 3: If aluminum is alloyed with elements such as silicon and magnesium, then mechanical properties such as yield strength and ultimate tensile strength will be greater than a commercially pure aluminum alloy, due to silicon's modification to the microstructure and magnesium's solid solution strengthening effects.

4.5 Materials and Methods

4.5.1 Description of the Metal 3-D Printer

The open-source GMAW-based metal 3-D printer and software toolchain utilized in this study have been described previously (Chapter 2; Nilsiam, et al., 2015). A Millermatic 190 GMAW welder with a Miller Spoolmate 100 weld gun were used to supply the weld power and the weld material. G-Code to control the 3-D printer was written manually and uploaded to a custom web server that directly interfaced with the

printer (Haselhuhn, et al., 2014; Wijnen, 2015). Standard weld-grade argon cover gas (99.995% purity) was used during printing. Voltage and current were monitored during printing using custom equipment (Pinar, et al., 2015); the weld power monitor measured voltage and current synchronously, providing signals that were processed and recorded by the robot's firmware.

4.5.2 Printing of Test Specimens

Standard ER1100 and ER4047 wire (AlcoTec Wire Corporation, 2016) in addition to ER4043, ER4943, and ER5356 wire (Hobart Brothers Company, 2016), 0.035 inches (0.889 mm) in diameter were used as feedstock material to 3-D print rectangular blocks (105.6 x 26.4 x 25.4 mm) onto cleaned and degreased ASTM A36 steel substrates (127 x 127 x 6.35 mm) (Table 4.2). Aluminum was printed onto low carbon steel as this was previously found to allow easy sample removal (Chapter 3; Haselhuhn, et al., 2014; Haselhuhn, et al., 2015).

Table 4.2 Compositions of Aluminum Weld Wire. (wt%; Single values are maximum values unless otherwise noted. Key elements are highlighted in bold font.)

Alloy	Si	Fe	Cu	Mn	Mg	Cr	Zn	Ti	Be	Others	
										Ea.	Total
ER1100 ^a	0.95		0.05-0.20	0.05	-	-	0.10	-	-	0.05	0.15
ER4043 ^b	4.5-6.0	0.8	0.30	0.05	0.05	-	0.10	0.20	<0.0003	0.05	0.15
ER4943 ^b	5.0-6.0	0.40	0.10	0.05	0.30-0.50	-	0.10	0.15	<0.0003	0.05	0.15
ER4047 ^a	11.0-13.0	0.8	0.30	0.15	0.10	-	0.20	-	0.0003	0.05	0.15
ER5356 ^b	0.25	0.40	0.10	0.05-0.20	4.5-5.5	0.05-0.20	0.10	0.06-0.20	<0.0003	0.05	0.15

^a AlcoTec Wire Corporation, 2016

^b Hobart Brothers Company, 2016

The welder and 3-D printer settings are described in Table 4.3 whereas the print path for each sample is described in Figure 4.1. Print settings were constant for all print alloys in order to evaluate the behavior of each alloy under identical processing conditions. All specimens were water quenched immediately after printing. Five (5) identical blocks were printed for each alloy.

Table 4.3 3-D Printing Parameters

Parameter	Value
Welder Power Setting (unitless)	1
Wire Feed Rate (mm/sec)	124.6
Print Speed (mm/sec)	10
Wire Stick-Out (mm)	10
Shield Gas Flow Rate (L/sec)	0.24
G-Code Layer Height (mm)	2.5
G-Code Lateral Bead Spacing (mm)	3.3
Pause After Each Layer (sec)	60
Number of Print Layers	15

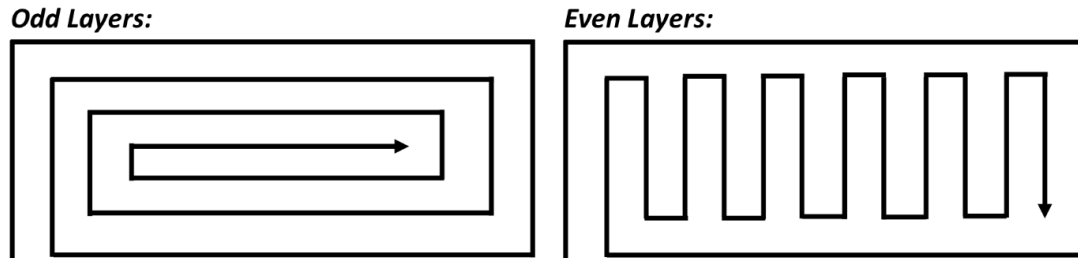


Figure 4.1 Alternating print paths for all specimens viewed in the direction of the z-axis

4.5.3 Specimen Machining & Analysis

Prior to machining, dimensions of test specimens and bulk porosities were measured. The average center bead width in the top print layer was measured in each alloy using Mitutoyo digital calipers with a 0.01 mm measurement resolution. This measurement was chosen as it was the most consistent and reliable bead in the top layer of the printed parts, although it did represent a worst-case scenario as the bead widths in the topmost layer would be the largest. Due to topological differences in the print specimens, ten measurements were taken along the entire length of the specimen and averaged. Internal (closed) porosity in all mechanical test specimens was measured in water according to the Archimedes' principle as described in a previous study (Chapter 3.3.4: Sample Testing & Analysis; Haselhuhn, et al., 2015).

Four blocks of each alloy were machined into standard round tensile bars (6.35 mm gauge diameter by 25 mm gauge length) using a lathe (ASTM, 2013). Each block was machined into 4 tensile bars. One block of each alloy was machined into

compression samples and a specimen for microstructural analysis using a 2½ axis CNC mill (Figure 4.2).

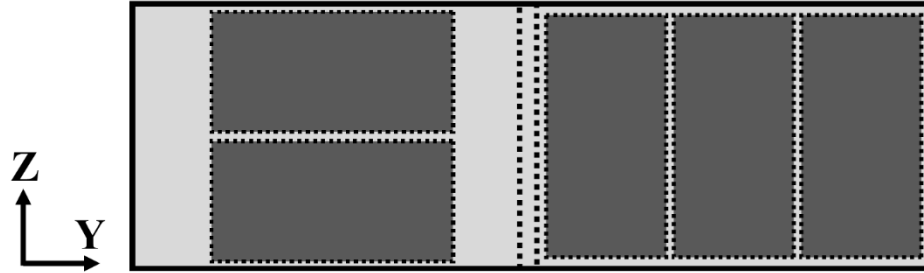


Figure 4.2 Orientation of compression and microstructural specimen machining.

Two compression rectangular solids were oriented parallel and three compression rectangular solids were oriented perpendicular to the print layer to evaluate any anisotropy. The 12.5 x 12.5 x 19 mm compression specimens had a height to width ratio of 1.5:1. The top and bottom surfaces of the specimens were polished to 0.05 µm using silica to reduce friction with the compression platens. Microstructural specimens were polished to 0.05 µm silica prior to being etched in Keller’s solution for 30 seconds for examination in an optical microscope

Tensile specimens were pulled to failure in an Instron load frame with an MTS control package using a 22 kN load cell at a strain rate of 10^{-3} sec^{-1} according to ASTM B557 (ASTM, 2013). An Epsilon clip-on axial extensometer with a 25 mm gauge length was used to measure the elongation of the specimen during tensile loading. Only specimens that broke within the gauge section were used for quantitative and qualitative

analysis. Tensile fracture surfaces were analyzed in a JEOL 6400 scanning electron microscope (SEM).

Prior to compression, the ultrasonic modulus of the machined compression specimens was measured using an Olympus 38DL Plus ultrasonic thickness gage. The longitudinal wave velocities were measured using an Olympus M112 transducer (10 MHz frequency, 6 mm transducer diameter) with a glycerin couplant. The shear wave velocities were measured using an Olympus V157 transducer (5 MHz frequency, 3 mm transducer diameter) with a shear gel couplant. Longitudinal and shear velocities were measured in two specimen orientations: Vertically from the top of the print to the bottom across many layers and horizontally across few layers. Using the longitudinal and shear velocities, in addition to the density measured via the Archimedes' principle, Poisson's ratio, elastic moduli, and shear moduli were calculated for each alloy as described in previous study (Chapter 3.4.4; Haselhuhn, et al., 2015). Using Poisson's ratio (ν) and elastic modulus (E), the bulk modulus (K) of each alloy was calculated (Equation 4.1) (Meyers & Chawla, 2009).

$$K = \frac{E}{3(1-2\nu)} \quad (4.1)$$

Following ultrasonic modulus testing, compression specimens were lubricated with graphite powder, preloaded to 44.5 N to ensure sample positioning, and loaded in an Instron load frame with a 150kN load cell at a strain rate of 10^{-3} sec^{-1} . Specimens were compressed to a maximum of 10% strain. The compression specimens were not loaded to failure as the load cell capacity was reached.

Low silicon solubility in 4043, 4943, and 4047 enabled cooling rate analysis via measurement of secondary dendrite arm spacing (SDAS) from images obtained using a standard optical microscope. SDAS was measured along the center of the 4043, 4943, and 4047 microstructural specimens using ImageJ software (Rasband, 2014). The SDAS was measured across the length of three or more secondary dendrite arms in an edge-to-edge fashion (Figure 4.3).

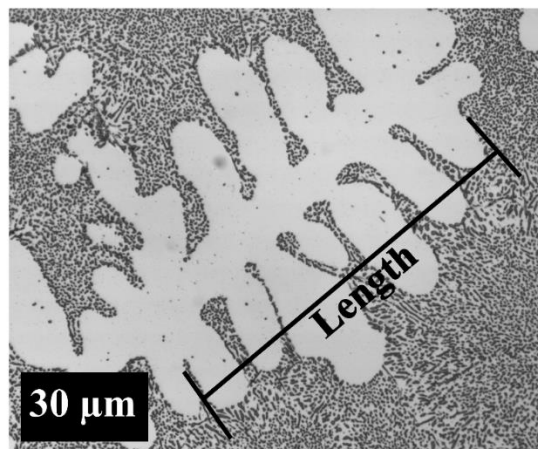


Figure 4.3 A dendrite in 4047 aluminum with a schematic line

The SDAS was calculated based upon the total number of secondary dendrite arm spaces (Equation 4.2) and a characteristic cooling rate was subsequently calculated (Equation 4.3). L is the length in μm and N is the number of dendrite arm spaces. The variable B is a fitting factor for a specific alloy and n is a constant. For 4043 aluminum, $B = 50 \mu\text{m} (\text{Ks}^{-1})^n$ and $n = 0.33$, a unitless number (Bouchard & Kirkaldy, 1997; Su, et al., 1994). Heard, et al. found agreement between calculated and experimental data when these 4043 aluminum constants were applied to 4047 aluminum (2012). The same computational analysis was applied to this study and extended to 4943 aluminum.

$$SDAS = \frac{L}{N} \quad (4.2)$$

$$Cooling\ Rate = \left(\frac{SDAS}{B}\right)^{-1/n} \quad (4.3)$$

The microstructural specimens were also analyzed in a Philips XL 40 environmental scanning electron microscope. Characterization of an iron gradient within the first two print layers was performed using energy dispersive spectroscopy for an alloy with a large solidification range (4043) and an alloy with a small solidification range (4047).

4.6 Results

4.6.1 As-Printed Dimensions & Porosity

The top layer center bead width ranged from approximately 5 to 6.5 mm (Figure 4.4). The bead width of 1100 was the smallest followed by the 4047 and 4043. The two alloys with magnesium additions, 4943 and 5356, exhibited the largest bead widths and were statistically equivalent.

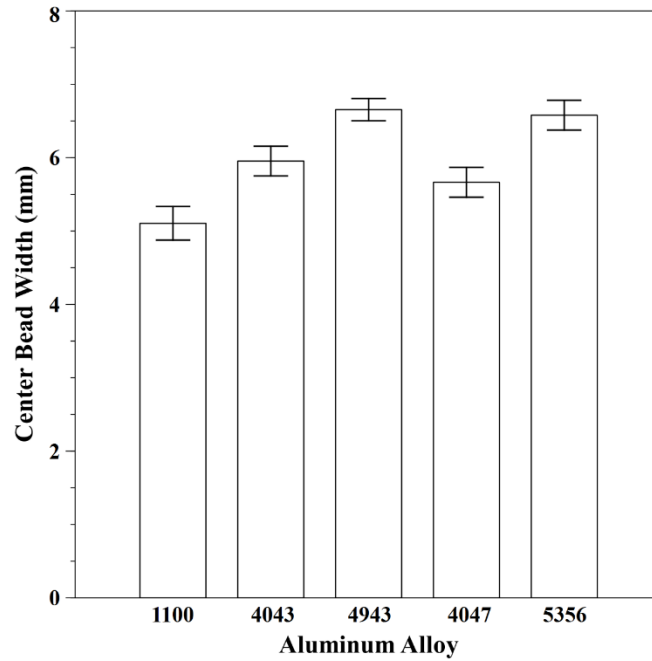


Figure 4.4 Average center bead width in the top print layer for each aluminum alloy.

Error bars represent ± 2 standard error (95% confidence interval).

Average porosity was generally low and ranged from 0.65 to 1.85% (Figure 4.5). The 1100 and 4043 as-printed parts were significantly less porous than the other three aluminum alloys. The high magnesium 5356 alloy exhibited the greatest porosity.

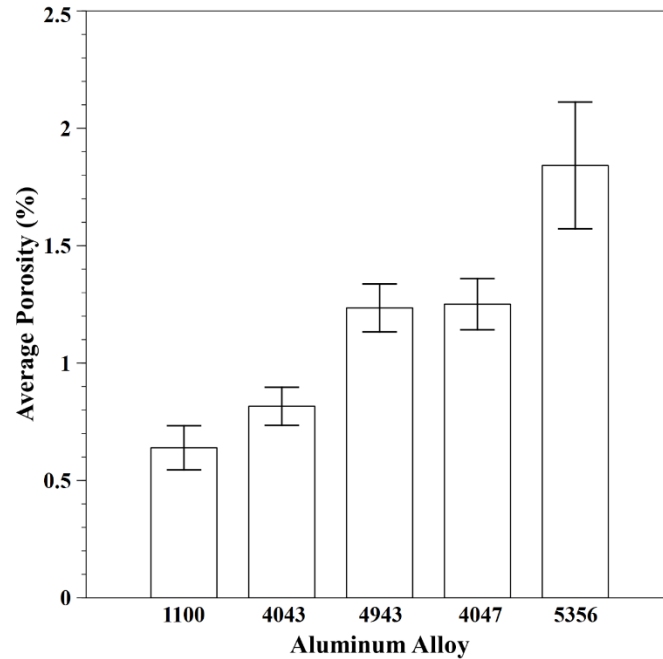


Figure 4.5 Average porosity of the as-printed specimens. Error bars represent ± 2 standard error (95% confidence interval).

4.6.2 Influence of Specimen Location & Orientation on Mechanical Properties

The shear modulus and elastic modulus (Figure 4.6), the tensile behavior (Figure 4.7), and the compressive behavior (Figure 4.8) of each aluminum alloy were evaluated based upon specimen orientation in the printed block. Horizontal elastic modulus, shear modulus, and compression specimens had their long axis in the x-y plane; vertical specimens had their long axis in the z-direction across many layers. In the tensile specimens bottom specimens were closer to the steel print substrate and had more heat flow through them than top specimens. Very minor differences in moduli, tensile behavior, or compressive behavior were observed based upon specimen orientation. The 1100 alloy vertical specimens exhibited higher moduli than the horizontal specimens. The

only differences in ultimate tensile strength based upon sample location occurred in 1100 and 4047 in which the strengths of the bottom specimens were less than those of the top specimens. In elongation, the bottom specimens of 1100, 4943, and 4047 were all less than the top specimens.

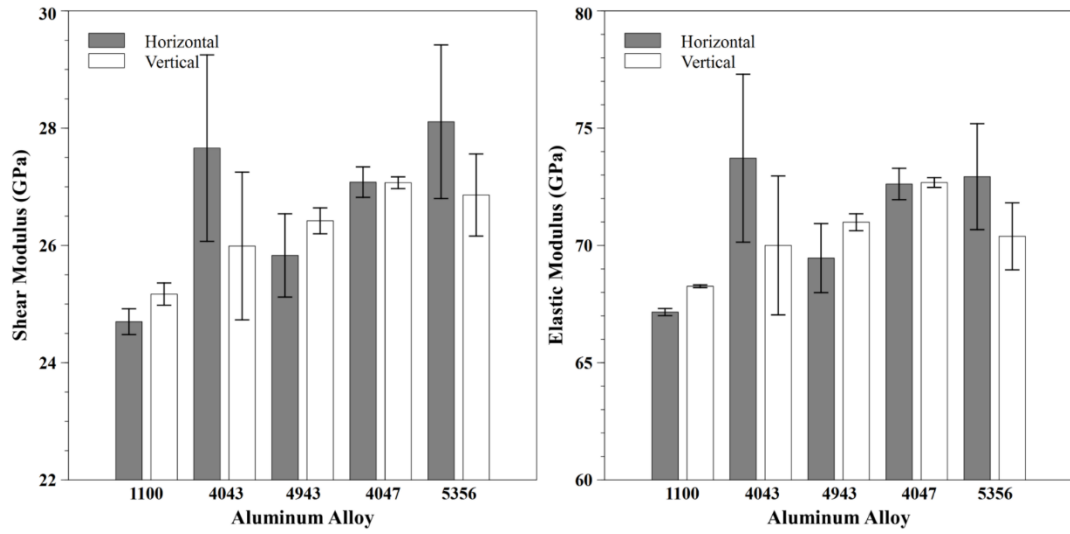


Figure 4.6 Influence of specimen orientation on ultrasonic moduli. Shear modulus (left) & elastic modulus (right) of each aluminum alloy. Error bars represent ± 2 standard error.

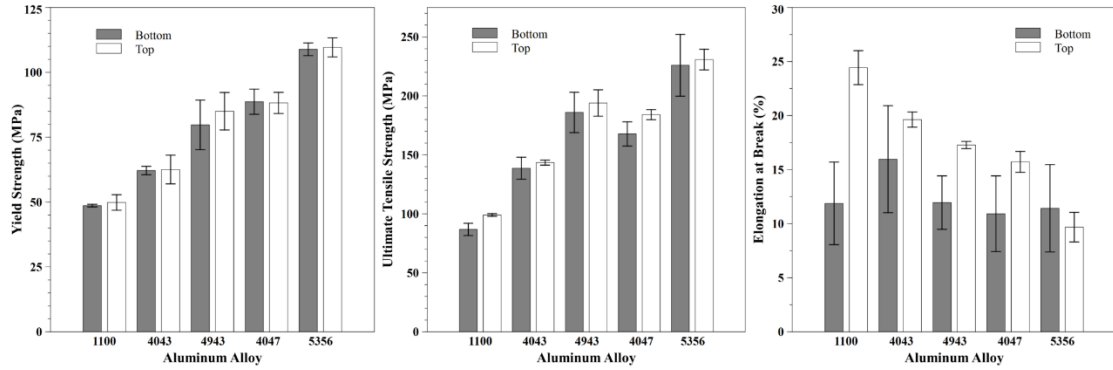


Figure 4.7 Influence of specimen location in printed block on mechanical properties. Tensile yield strength (left), ultimate yield strength (center), & elongation at break (right). Error bars represent ± 2 standard error.

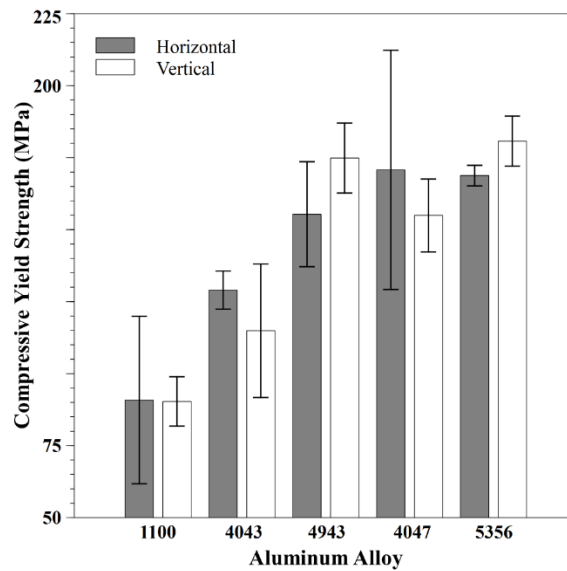


Figure 4.8 Influence of specimen orientation in printed block on compressive yield strength. Error bars represent ± 2 standard error.

4.6.3 Average Mechanical Properties

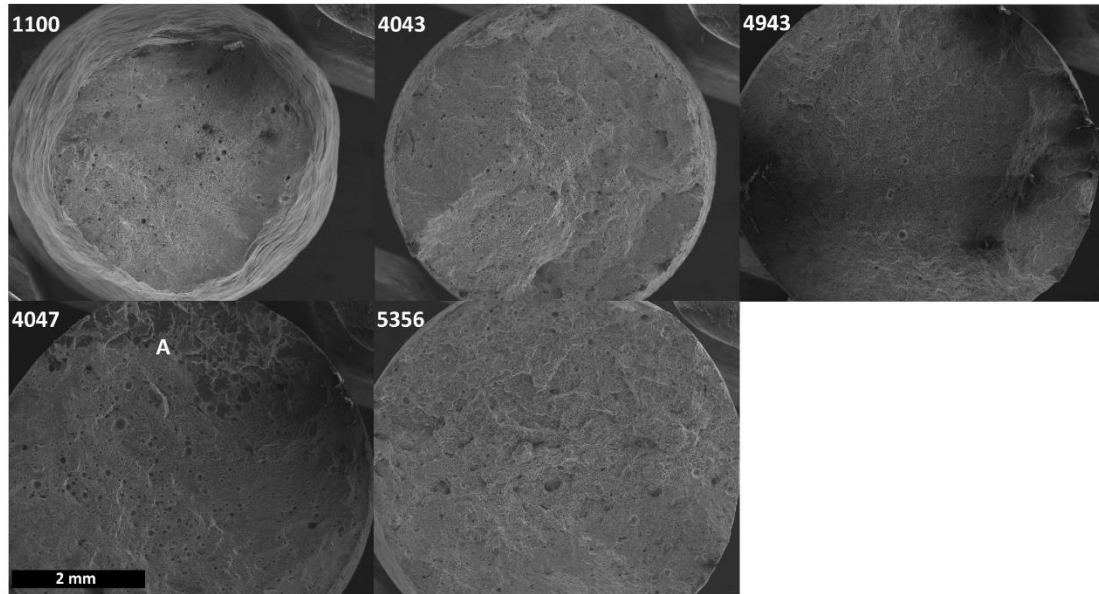
The shear and elastic moduli of all alloys were greater than those for 1100 (Table 4.4). The elastic and shear moduli of 4047 were also greater than those observed for 4943. There was no significant difference in the moduli of 4043 and 4943. Greater variation in the data was observed for 4043 and 5356 specimens. The bulk modulus was largest for 1100 specimens. The low-silicon 4043 and 4943 specimens exhibited a larger bulk modulus on average than 4047 although this trend was not statistically significant. The 5356 specimens exhibited the smallest bulk modulus.

Table 4.4 Average Calculated Elastic Properties for Each Aluminum Alloy. (± 2 standard error)

Alloy	Poisson's Ratio	Elastic Modulus (GPa)	Shear Modulus (GPa)	Bulk Modulus (GPa)
1100	0.36 ± 0.005	67.7 ± 0.5	25.0 ± 0.3	77.8 ± 2.5
4043	0.34 ± 0.009	71.5 ± 2.7	26.7 ± 1.2	75.0 ± 1.4
4943	0.34 ± 0.005	70.4 ± 0.9	26.2 ± 0.4	75.2 ± 2.1
4047	0.34 ± 0.001	72.7 ± 0.2	27.1 ± 0.1	76.5 ± 0.4
5356	0.31 ± 0.010	71.4 ± 1.6	27.4 ± 0.8	61.2 ± 1.8

Tensile specimen fracture surfaces were highly ductile with typical cup-cone surface morphology (Figure 4.9). Variation in specimen diameters in Figure 4.9 demonstrate the reduction of area associated with tensile deformation. The 1100 tensile specimens also exhibited macro-coning. Some of the 4047 tensile specimens exhibited some regions of brittle fracture while some of the 5356 tensile specimens exhibited cracking along discrete lines, likely corresponding to barriers between print layers. All

fracture surfaces also exhibited higher than average bulk porosity, likely resulting from material failure at locally weak regions having the highest concentration of defects.



***Figure 4.9 Tensile fracture surfaces of 3-D printed aluminum alloys. Note macro-
coning in the 1100 specimen and the region of brittle fracture in 4047 (A). Scale bar
represents 2 mm.***

Rounded gas porosity was observed in all alloys (Figure 4.10). In all alloys except 1100, interdendritic or intergranular shrinkage was observed on the fracture surfaces. In these alloys, shrinkage porosity would often be combined with gas-type porosity.

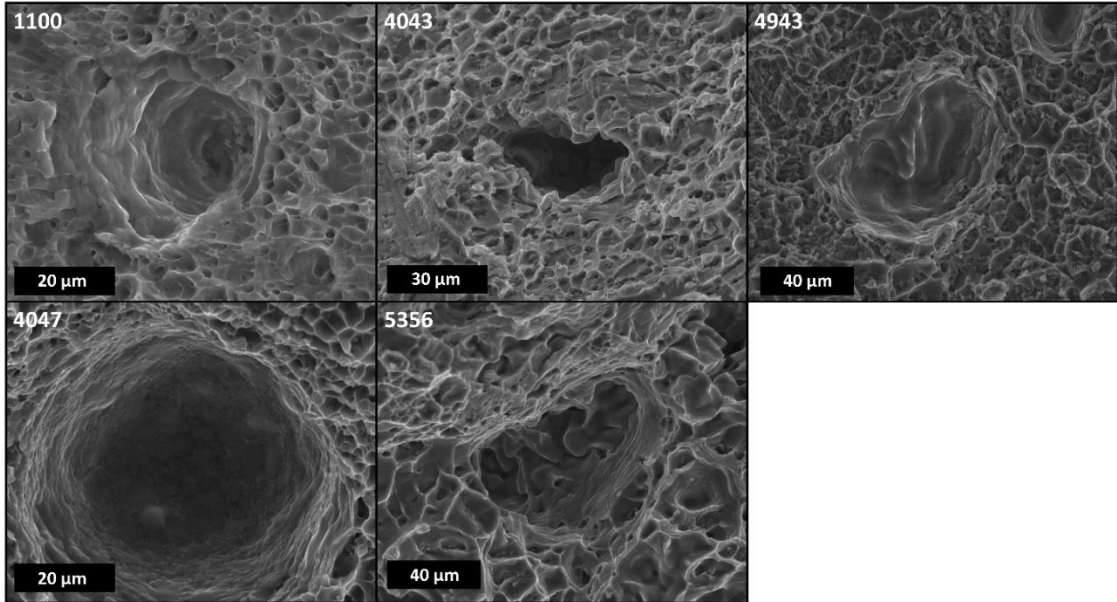


Figure 4.10 Examples of porosity in each 3-D printed aluminum alloy.

It should be noted that the Figure 4.10 images were taken of typical pore sizes for each alloy and thus shown at appropriate magnification to make them clear, but they are not all the same size and as can be seen in Figure 4.11 there are also much larger macro pores. The brittle regions in 4047 also exhibited porosity, although to a lesser extent than the ductile regions (Figure 4.11). These brittle regions were only observed in some of the tensile specimens machined closest to the print substrate. The brittle fracture regions were marked by transgranular fracture in which aluminum grains were sheared. Element mapping of brittle regions in the 4047 fracture surfaces yielded large features containing primarily silicon with small amounts of iron exhibited as lamellar features. The iron lamellae were only visible in the bottom 1-2 mm of the gauge section.

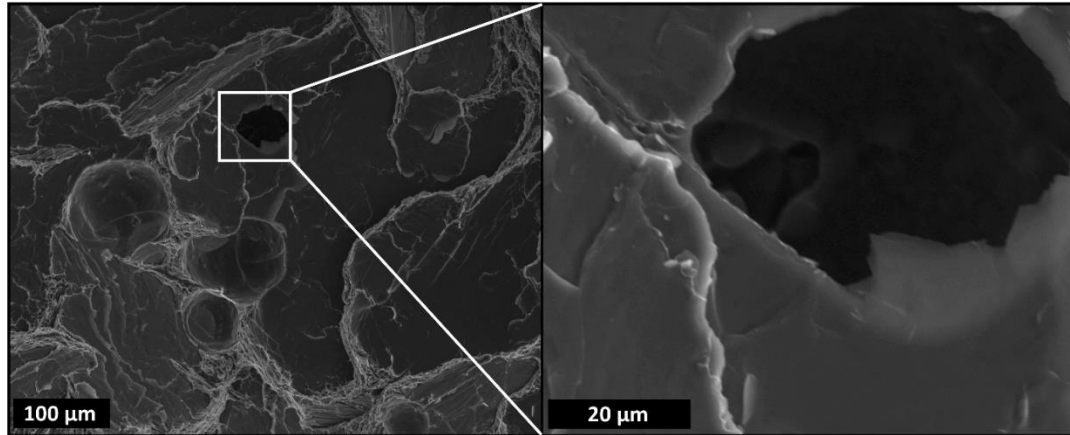


Figure 4.11 Brittle 4047 fracture surface. Enlarged image of porosity in brittle region shown at right.

Given that no significant differences were observed with respect to sample location and orientation, all the mechanical measurements were averaged for subsequent analysis. Additionally, defective 4047 tensile specimens with visible brittle regions were removed from the analysis. The ultimate tensile strengths of the magnesium containing 4943 and 5356 alloys were the highest followed by 4047, 4043, and 1100 (Figure 4.12). The 2% offset tensile yield strengths generally followed the same trend except that 4943 fell to the same level as 4047. Compressive yield strength was significantly higher than tensile yield strength. Compressive and tensile yield strengths followed the similar trends on a per alloy basis. Elongation to failure was generally in the range of 15 to 17% except for 5356 which was at 10%. The 1100 alloy had the most elongation variation.

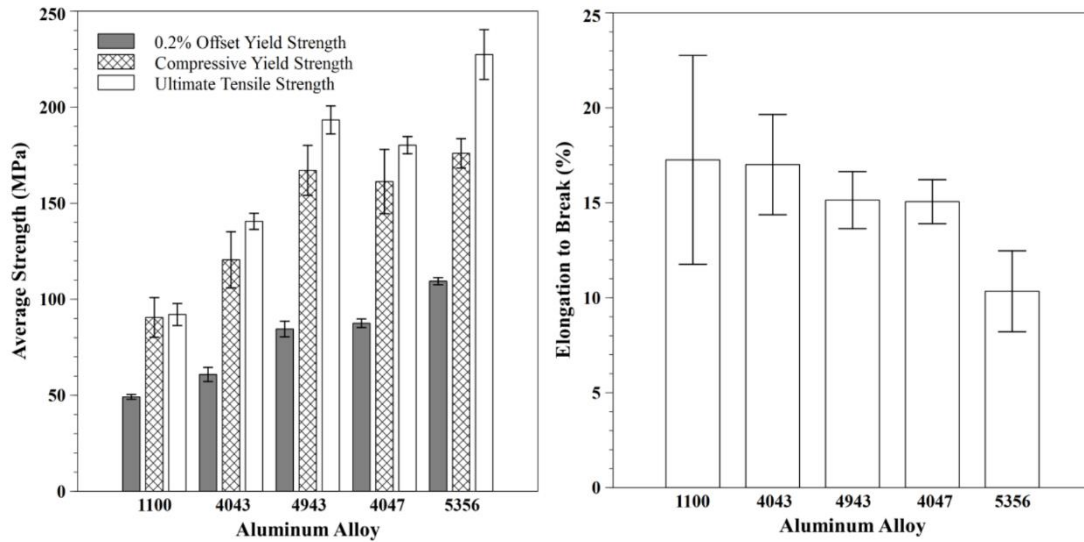


Figure 4.12 Average mechanical properties of printed specimens. 0.2% offset yield, compressive yield, and ultimate tensile strengths of the aluminum tensile specimens (left). Elongation at failure of the tensile specimens based upon aluminum alloy type (right). Error bars represent ± 2 standard error (95% confidence interval).

An estimate of the strain hardening behavior can be made by subtracting the tensile yield strength from the ultimate tensile strength for each alloy (Figure 4.13) (Tiryakioglu & Staley, 2003). As solute concentration increases, the amount of strain hardening also increases. Although there are only slight differences in silicon content between 4043 and 4943, the small magnesium solute concentration in 4943 contributes significantly to the strain hardening response.

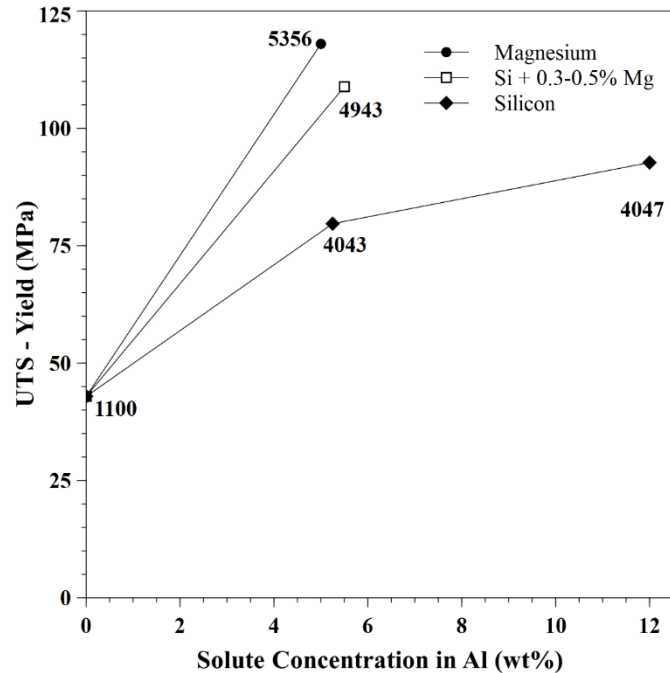


Figure 4.13 Estimate of the strain hardening response of each aluminum alloy based upon solute content.

4.6.4 Microstructural Analysis

The single-phase 1100 and 5356 compression specimens exhibited few microstructural features whereas the aluminum and silicon phases were visible in unetched 4043, 4943, and 4047 specimens (Figure 4.14). The similar Si contents of 4043 and 4943 produced microstructures with comparable amounts of interdendritic dendrites; whereas 4047 had larger areas of eutectic microconstituent. Black features in the “bottom” images may correspond to either hydrogen porosity or regions in which the iron was pulled out of the specimen during polishing procedures.

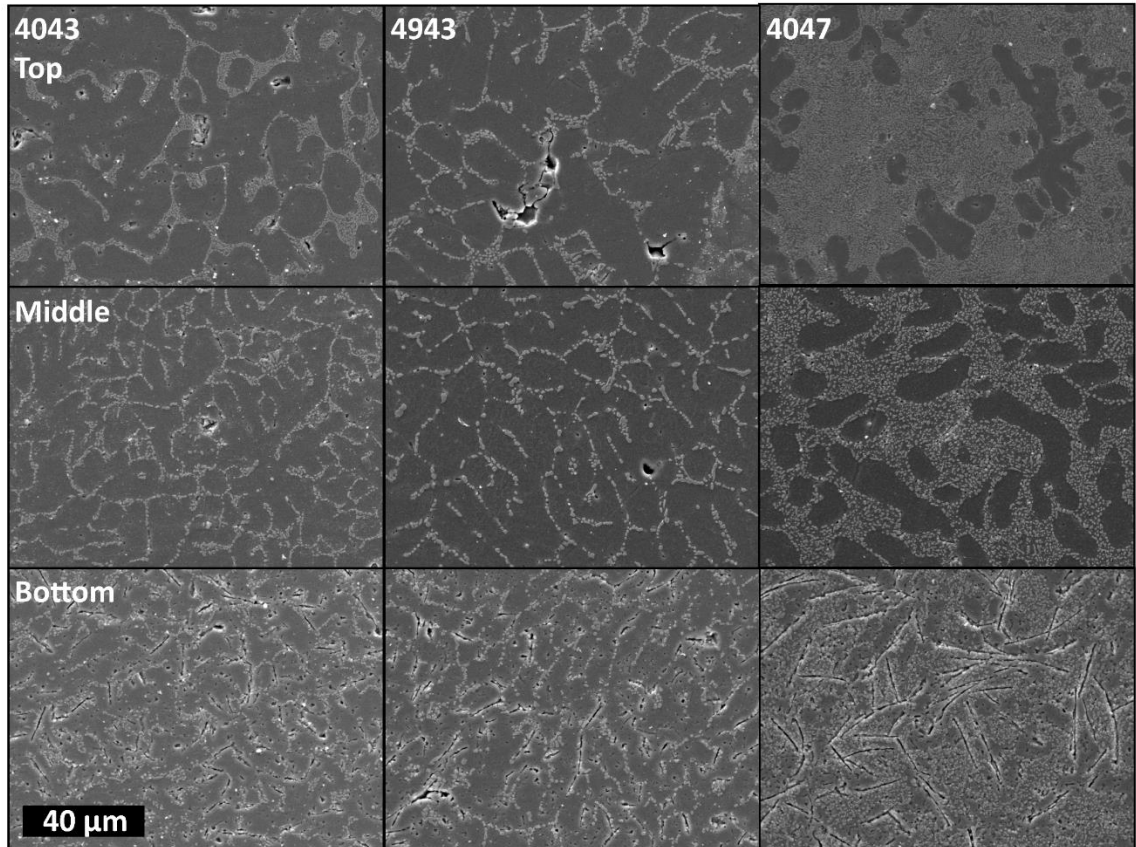


Figure 4.14 Scanning electron images of 4000 series test specimens in the bottom, top, and middle of the printed block. Scale bar represents 40 μm.

The secondary dendrite arm spacing (SDAS) of all the 4000 series alloys averaged 8-10 μm (Figure 4.15). The 4043 and 4047 cross-sections exhibited consistent SDAS with no long range trends within the sample, while the 4943 SDAS increased linearly with distance from the substrate (Equation 4.4).

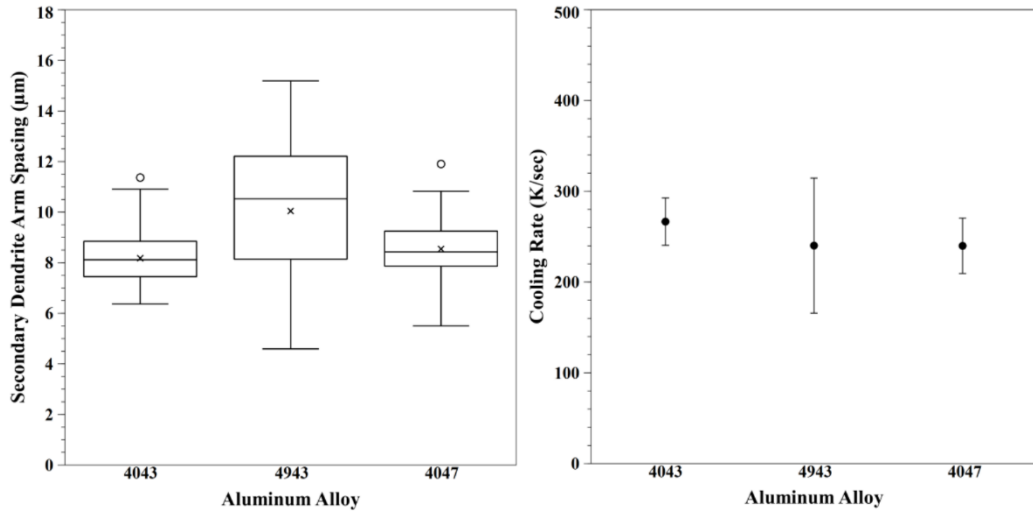


Figure 4.15 Secondary dendrite arm spacing (SDAS) analysis of printed specimens. Box plots of 4000 series SDAS (left) and corresponding average cooling rates (right).

Error bars represent ± 2 standard error.

$$4943 \text{ SDAS}(\mu\text{m}) = [0.31 * \text{Distance from substrate}(\text{mm})] + 5.72 \quad (4.4)$$

Iron contamination was observed in the first layer microstructure of each printed alloy (Figure 4.16), but the iron concentration decreased significantly in the second layer. In the 4000 series specimens, iron contaminants were present as randomly oriented plates. These plates were not visible beyond the first print layer (approximately 3.8 mm above the print substrate) where the iron content was significantly lower than in the previous layer of the specimen (Figure 4.17).

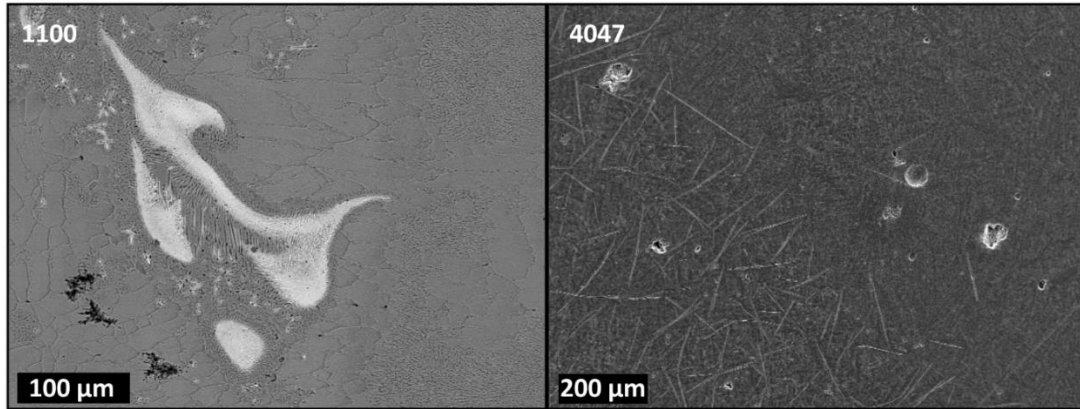


Figure 4.16 Secondary electron images of iron contamination in the first print layer of 1100 and 4047.

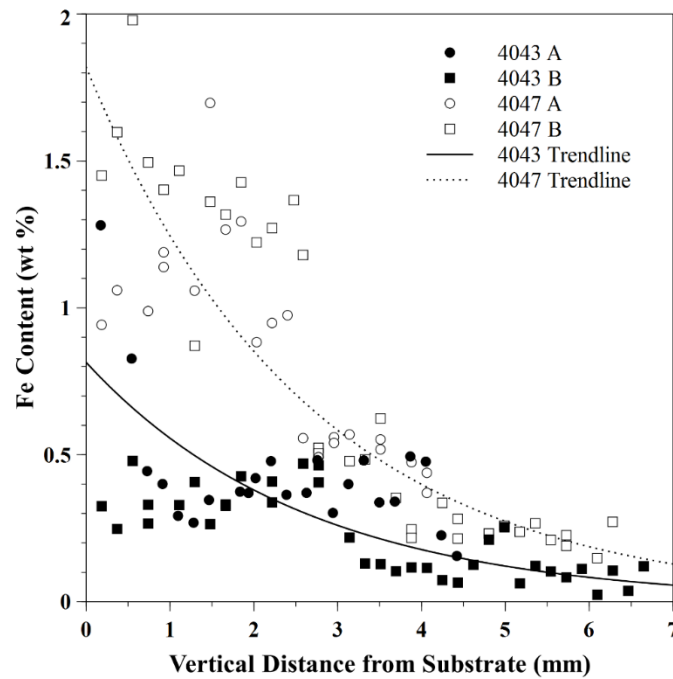


Figure 4.17 Iron gradient from EDS of the first two print layers of 4043 and 4047.

The 4047 microstructure in brittle regions of the tensile fracture surface exhibited silicon and iron within the lamellar features (Figure 4.18) shown previously (Figure 4.16).

Portions of the iron plates were pulled out during the polishing process, leaving behind crack-like formations that appear as voids.

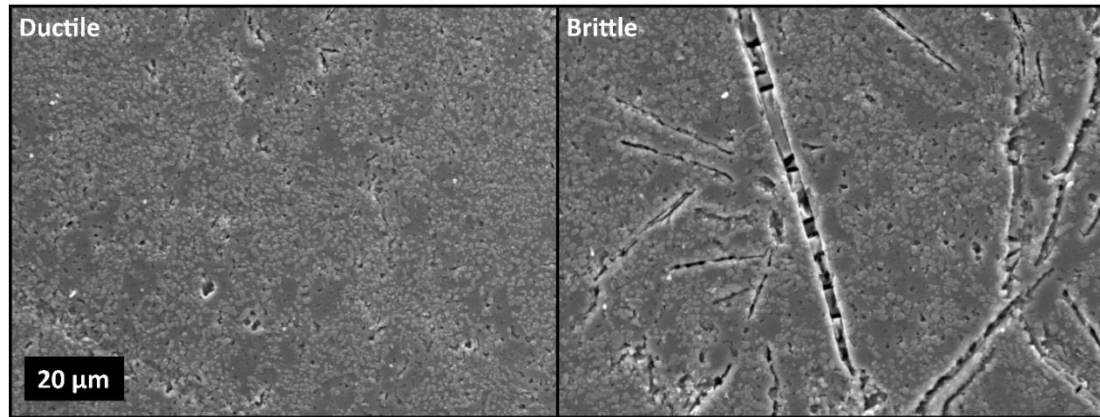


Figure 4.18 Variation in microstructures observed in 4047 tensile specimens. Both ductile (left) and brittle regions (right) were observed. Scale bar represents 20 μm .

4.7 Discussion

4.7.1 As-Printed Dimensions & Porosity

At similar cooling rates, one would expect alloys with large freezing ranges to take more time to solidify and thus have the potential to flow into wider beads. Indeed, the commercially pure 1100 aluminum and near-eutectic 4047 exhibited the smallest bead widths while the alloys with magnesium and larger freezing ranges (4943 and 5356) had larger bead widths.

Alloy fluidity aids in feeding interdendritic shrinkage. Improved fluidity is observed with decreasing solidification range and with a decrease in liquid metal viscosity. Both silicon and magnesium additions have been shown to decrease the

internal friction in molten aluminum alloys, resulting in a decrease in viscosity (Hatch, 1984). Metal fluidity increases as the solidification range decreases such that pure alloys (1100) and near-eutectic alloys (4047) will exhibit less shrinkage porosity than alloys with larger solidification ranges (4043, 4943, and 5356) (Tiryakioglu & Staley, 2003). The observed interdendritic shrinkage (Figure 4.10) is common in aluminum weld structures (Easterling, 1983). Alloys with higher silicon contents such as 4047 have fewer primary aluminum dendrites and are less likely to have interdendritic shrinkage and cracks as interdendritic feeding is able to fill the space between dendrite before the metal is fully solidified (Kou, 1987). In alloys with more primary aluminum dendrites, such as 4043 and 4943, interdendritic feeding is more difficult resulting in interdendritic porosity. Additionally, unlike aluminum, silicon has higher specific and latent heats, and expands as it solidifies and alloys with higher silicon contents suffer less from interdendritic shrinkage (Tiryakioglu & Staley, 2003). Magnesium additions in 4943 and 5356 produce larger solidification ranges leading to higher shrinkage porosity.

Aluminum has a high affinity for hydrogen, which is less soluble in solid metal than in a liquid metal (Kou, 1987). Upon cooling, this gas comes out of solution and either escapes or, if solidification is sufficiently fast, is trapped to form gas porosity. If reactive magnesium is oxidized, it can increase porosity by serving as heterogeneous nucleation sites for pores (Tiryakioglu & Staley, 2003). Thus, alloys with magnesium additions (4943 and 5356) would exhibit more nucleation sites for porosity formation. Further, testing hypothesis 1, with 95% confidence the null hypothesis, stating there

would be no difference in porosity based upon alloy type, was rejected and alternative hypothesis 1 was accepted.

4.7.2 Influence of Specimen Orientation on Mechanical Properties

With 95% confidence, null hypothesis 2 stating that there would be no difference in elastic or shear modulus based upon specimen orientation could not be rejected.

Mechanical properties were not observed to differ significantly based upon specimen location or orientation. The layered structure of the 3-D printed parts did not negatively affect compressive or ultrasonic mechanical properties. Elevated iron levels were observed in the first layer of all alloys, up to approximately 4 mm above the print substrate, which resulted in fibrous iron intermetallics in the first layer (Figure 4.17). This iron gradient did not extend far enough in the 3-D printed blocks to cause elevated iron content in the gauge section of tensile specimens or in the compression specimens.

Elevated iron content within the first 4 mm was a result of printing the aluminum test specimens on a steel substrate. To evaluate whether this iron content was the result of solid state diffusion, liquid mixing in the weld pool, or a combination thereof, the theoretical steady state diffusion length of iron in aluminum was calculated (Equation 4.5) (Porter, et al., 2009).

$$Length = \sqrt{Diffusivity * time} \quad (4.5)$$

The diffusivity of iron in pure aluminum was reported by Hirano, et al., to be $4.9 \cdot 10^{-9} \exp(-13,900/RT)$ cm²/sec (Hirano, et al., 1962). Using this information, the diffusion length of iron into aluminum was calculated at the melting temperature of pure

aluminum (933 K) and at the eutectic temperature of a hypoeutectic aluminum-silicon alloy (850 K) (Figure 4.19).

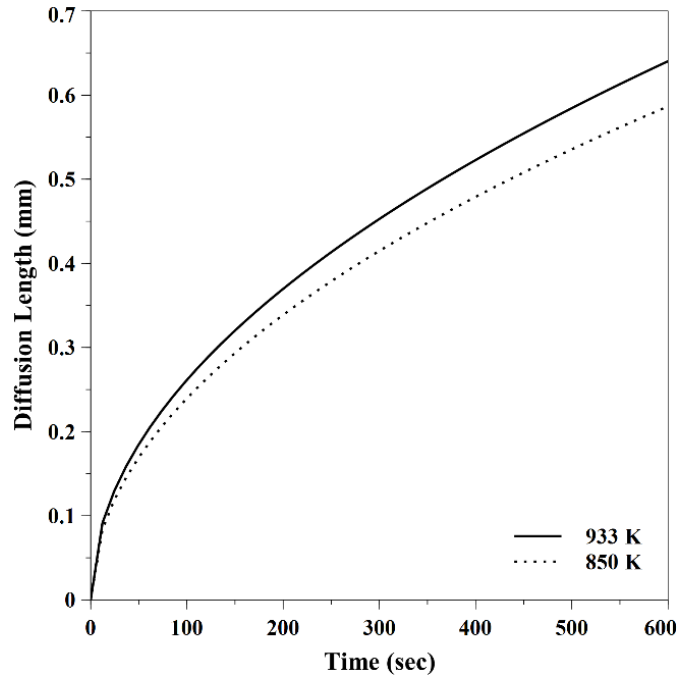


Figure 4.19 Calculated diffusion length of iron in aluminum as a function of solidification time.

From Figure 4.19 it was evident that even at long solidification times of 300 or more seconds, the maximum diffusion length of iron in aluminum is less than 1 mm. Thus, solid state diffusion cannot fully account for the iron gradient observed in 3-D printed aluminum parts. Fluid flow within the liquid metal weld pool mixed iron compounds into the first layer of the welded part, resulting in iron contents further into the welded part than could be accounted for by solid state diffusion (Kou, 1987). In the aluminum-silicon alloys this resulted in lamellar features. These same features were observed in hypoeutectic aluminum-silicon alloyed with iron additions and were determined to be

Al₅FeSi platelets (Lu & Dahle, 2005). The iron gradient observed previously at the interface between the printed aluminum part and the steel substrate (Figure 3.9) was not evaluated in specimens analyzed in this study as the observed platelets were of greater concern to mechanical properties. The use of alternate substrate release mechanisms for larger prints, such as alumina or nitride coatings, may eliminate iron contamination when printing aluminum on steel (Chapter 3; Haselhuhn, et al., 2014; Haselhuhn, et al., 2015).

4.7.3 Microstructural Analysis

The SDAS in this study were similar to those reported by Heard, et al., who observed an approximately constant SDAS of 5.7 μm in four layers of 4047 printed by a GMAW-based 3-D printer with five minute pauses between layers (2012). The 4043 and 4047 specimens in this study had approximately constant SDAS of 8.4 μm across 15 print layers. In contrast, the 4943 SDAS averaged 10 μm but with an increasing linear trend with vertical distance from the substrate. Weld current and voltage in this study were lower than those used by Heard, et al., (2012). Heat input is directly proportional to voltage and current and inversely proportional to weld speed (Lancaster, 1993). Greater heat input results in slower cooling and larger SDAS. A weld speed was not reported by Heard, et al., but a faster speed could produce the smaller SDAS than that observed in this study (2012). Additionally, differences in specimen size and shape could result in different cooling that could explain differences in SDAS. The specimens in this study were blocks consisting of 15 layers requiring 40 minutes to print, whereas the specimen's in Heard's study were 4 layer cylinders. The larger specimen size in this study would contribute to slower cooling and thus a larger microstructure. Additionally, only a 1

minute pause was utilized between print layers in this study whereas 5 minutes per print layer reported in Heard's study. Overall, results from this study were similar to those reported by Heard, allowing for small differences due to differences in experimental set-up.

There were no observed differences in the macro solidification structure such as a finer structure near the print outer surface as compared to interior. In castings, the metal solidifies first at the specimen edges and then directionally cools from the outside in (Campbell, 2008). Thus, the smallest microstructural elements would be found at the specimen edges, yielding to columnar growth inward then to large equiaxed grains in the center of the casting where slower cooling occurred. In welds solidification occurs faster because there is less material deposited at a given time and less heat to extract prior to solidification of the weld. In multi-layer welds, similar to weld-based 3-D printing, the edges of previously welded beads are melted or partially melted which promotes homogenization of the microstructure (Lancaster, 1993; Kou, 1987). SDAS on the order of 10 μm is common in welding whereas larger dendrite arm spacings on the order of 100 μm are more common in casting (Campbell, 2008).

4.7.4 Mechanical Properties

The average yield strengths and ultimate tensile strength of aluminum containing alloying elements such as silicon and magnesium (4043, 4943, 4047, and 5356) were greater than that of commercially pure 1100 aluminum. With a p-value less than .05, with 95% confidence null hypothesis 3, stating there would be no influence of yield and tensile strength based upon alloy type, was rejected, and alternative hypothesis 3 was

accepted. All 3-D printed alloys exhibited similar or superior mechanical properties in comparison to standard wrought, weld, or cast counterparts (Table 4.5). Two exceptions to this trend were the lower ductility of 1100 printed specimens and the lower strength of printed 5356 as compared to the wrought material. The 3-D printed aluminum-silicon alloys may have exhibited greater ductility than their cast counterparts due to a smaller microstructure, as described previously (section 4.7.3). The SDAS of 3-D printed specimens was smaller than average cast SDAS. These smaller dendrites would allow for greater dislocation motion prior to plastic deformation. In general, the fine structure of the printed materials outperformed their macro-cast counterparts and approached the performance of wrought-processed material.

**Table 4.5 Mechanical Properties of Aluminum Alloys from Multiple Processes
Compared with Study Results**

Alloy	Process	Tensile Yield (MPa)	UTS (MPa)	Elong. (%)
1100-O ^a 1100/1100 ^b 1100	Wrought Weld This Study	34 31 (min) 49 ± 1	90 75.8 (min) 92 ± 6	40 29 17 ± 6
443.0 (Al-5.2Si) ^a Al-5Si ^c 4043 (~5.3 Si) 4943 (~5.5 Si) Al-11.5 Si ^c 4047 (~12 Si)	Cast Cast This Study This Study Cast This Study	55 60 61 ± 3 85 ± 4 65 88 ± 2	130 125 141 ± 4 193 ± 7 170 180 ± 4	8 5 17 ± 3 15 ± 2 8 15 ± 1
5356-O ^a 514.0 (Al-4Mg) ^a 535.0 (Al-6.9Mg) ^a 5356 (~5 Mg)	Wrought Cast Cast This Study	130 83 124 109 ± 2	285 172 250 230 ± 10	- 9 9 10 ± 2

^a Kaufman, 1999

^b Dickerson, 1993

^c Gale & Totemeier, 2003

Compressive yield strength was expected to be higher than in tension. Porosity defects, and particularly non-spherical porosity defects such as interdendritic shrinkage, act as stress concentrators. In tension these defects severely limit material strength whereas in compression they are less detrimental. The decrease in yield strength may also be related to the Peierls stress in aluminum alloys (Hertzberg, et al., 2012; Shin & Carter, 2013). Peierls stress, also known as lattice friction, is the shear stress required to move a dislocation in a given crystal structure. The stress required to move a dislocation increases in compression due to the closer spaced planes and obstacles to dislocation motion. As dislocation pileup occurs, the mobility of dislocations concurrently decreases

and more stress must be applied to plastically deform a material, resulting in work hardening (Hertzberg, et al., 2012). There is also more dislocation pileup during compression than in tension, which can be further compounded by alloying additions (Tiryakioglu & Staley, 2003). For instance, magnesium has been observed to increase dislocation multiplication and storage rates, thus increasing work hardening and suppressing recovery in aluminum-magnesium alloys. In aluminum-silicon alloys, dislocations pile up at silicon phases during plastic deformation because the hard silicon phases cannot be sheared by dislocations. However, Peierls stress would likely be a small contributor compared to porosity defects.

Porosity defects can act as stress concentrators causing premature tensile yielding. Interdendritic shrinkage porosity, which is typically elongated and has sharper edges, acts as a greater stress concentrator than spherical gas porosity. Fracture of the tensile specimens occurred in regions of higher than average porosity. Future work is necessary to optimize printer parameters (e.g., welder power, wire feed rate, welding speed, etc.) to minimize defect density. Hydrogen was likely a significant cause of the spherical gas porosity; these defects can be minimized through improved environmental control. Gas porosity defects in 1100 and the combination of gas porosity and interdendritic/intergranular shrinkage defects in 4043, 4943, 4047, and 5356 led to reductions in mechanical properties, particularly elongation.

4.8 Conclusions

A low-cost GMAW-based 3-D metal printer was used to print 1100, 4043, 4943, 4047, and 5356 aluminum parts. The mechanical properties of 3-D printed aluminum

alloys were evaluated via tensile and compression tests in conjunction with microstructural analysis. This work was performed in order to optimize process parameters and guide future development of alloys specifically for use with GMAW-based 3-D printing.

The 4000 series alloys performed better than the other alloys studied when considering porosity and strength. The 1100 specimens exhibited the smallest bead width and lowest porosity, but were also the weakest in tension and compression. The 4000 series alloys exhibited similar bead widths and porosities compared with 1100. Unlike 1100, the 4000 series alloys exhibited significantly higher strengths. The small magnesium additions in 4943 significantly increased its strength over 4043. While the 5356 specimens were the strongest, they also exhibited the largest bead width and the greatest amount of porosity. These porosity defects likely limited the 5356 test specimens' strength compared with their wrought counterparts.

4.9 References

AlcoTec Wire Corporation. Alloy 1100 weld data sheet. <http://www.alcotec.com/us/en/support/upload/a1100tds.pdf>, last accessed February 3, 2016.

AlcoTec Wire Corporation. Alloy 4047 weld data sheet. <http://www.alcotec.com/us/en/support/upload/a4047tds.pdf>, last accessed 3 February 2016.

Anderson, B.E. (2011). U.S. Patent Application No. 13/023,158. Publication No. 2011/0194973 (Published August 11, 2011). Washington, DC: U.S. Patent and Trademark Office.

- Anzalone G. C., Zhang C., Wijnen B., Sanders, P. G., Pearce, J. M. (2013). A low-cost open-source metal 3-D printer. *IEEE Access*, 1, 803-810.
- ASTM B557-02. Standard Test Methods for Tension Testing Wrought and Cast Aluminum- and Magnesium-Alloy Products. ASTM International, West Conshohocken, PA, 2013, www.astm.org.
- Birtchnell, T., & Hoyle, W. (2014). *3D Printing for Development in the Global South: The 3D4D Challenge*. Palgrave Macmillan.
- Bouchard, D., & Kirkaldy, J. S. (1997). Prediction of dendrite arm spacings in unsteady- and steady-state heat flow of unidirectionally solidified binary alloys. *Metall. Mater. Trans. B*, 28(4), 651-663.
- Bowyer, A., 2014. 3D Printing and Humanity's First Imperfect Replicator. *3D Printing and Addit. Manuf.*, 1(1), pp.4-5.
- Campbell, F. C. (Ed.). (2008). *Elements of Metallurgy and Engineering Alloys*, ASM International, Materials Park, OH, 487-508.
- Cross, C.E., Olson, D.L., & Liu, S. (2003). Aluminum Welding. In G.E. Totten & D.S. MacKenzie (Eds.), *Handbook of Aluminum Volume 1* (481-532). New York: Marcel Dekker, Inc.
- Delgado, J., Ciurana, J., & Serenó, L. (2011). Comparison of forming manufacturing processes and selective laser melting technology based on the mechanical properties of products. *Virtual Phys. Prototyp.*, 6(3), 167-178.

- Dickerson, P. B. (1993). Welding of Aluminum Alloys. ASM Handbook, 6, 722-739.
- Easterling, K. Introduction to the physical metallurgy of welding; 1983. London, Butterworth.
- Gale W. F., & Totemeier, T. C. (Eds.). *Smithells metals reference book*, 8th Ed., Butterworth-Heinemann, 2003, 14-16.
- Gaytan, S. M., Murr, L. E., Medina, F., Martinez, E., Lopez, M. I., & Wicker, R. B. (2009). Advanced metal powder based manufacturing of complex components by electron beam melting. *Mater. Tech.*, 24(3), 180-190.
- Gebhardt, A. *Rapid Prototyping*. Germany: Hanser Verlag, 2003.
- Gershenfeld, N. *Fab: The Coming Revolution on Your Desktop – from Personal Computers to Pers. Fabr.*, New York: Basic Books, 2005.
- Haselhuhn, A. S., Gooding, E. J., Glover, A. G., Anzalone, G. C., Wijnen, B., Sanders, P. G., & Pearce, J. M. (2014). Substrate release mechanisms for gas metal arc weld 3-D aluminum metal printing. *3-D Print. Addit. Manuf.*, 1(4), 204-209.
- Haselhuhn, A. S., Wijnen, B., Anzalone, G.C., Sanders, P.G., & Pearce, J.M. (2015). In situ formation of substrate release mechanisms for gas metal arc weld metal 3-D printing. *J. Mater. Process. Tech.*, 226, 50-59.
- Hatch, J.E. Aluminum Properties and Physical Metallurgy. 1984. Metals Park, Ohio: American Society for Metals.

- Heard, D. W., Brophy, S., & Brochu, M. (2012). Solid freeform fabrication of Al-Si components via the CSC-MIG process. *Can. Metall. Q.*, 51(3), 302-312.
- Heinl, P., Rottmair, A., Körner, C., & Singer, R. F. (2007). Cellular titanium by selective electron beam melting. *Adv. Eng. Mater.*, 9(5), 360-364.
- Hertzberg, R.W., Vinci, R.P., & Hertzberg, J.L. (2012). Deformation and Fracture Mechanics of Engineering Materials. 5th Ed. New York: John Wiley & Sons.
- Hirano, K., Agarwala, R. P., & Cohen, M. (1962). Diffusion of iron, nickel, and cobalt in aluminum. *Acta Metall.*, 10(9), 857–863.
- Hobart Brothers Company. Hobart MAXAL 4043.
http://maxal.com/Hobart_Maxal_4043.pdf, last accessed 3 February 2016.
- Hobart Brothers Company. Hobart MAXAL 4943.
http://maxal.com/Hobart_Maxal_4943.pdf, last accessed 3 February 2016.
- Hobart Brothers Company. Hobart MAXAL 5356.
http://maxal.com/Hobart_Maxal_5356.pdf, last accessed 3 February 2016.
- Jones, R., Haufe, P., Sells, E., Irvani, P., Olliver, V., Palmer, C., & Bowyer, A. (2011). RepRap—the replicating rapid prototyper. *Robotica*, 29(01), 177-191.
- Kaufman, J. G. (Ed.). (1999). Properties of aluminum alloys: Tensile, creep, and fatigue data at high and low temperatures. ASM International.
- Kou, S. (1987). *Welding Metallurgy*. New York: John Wiley & Sons.

- Laeng, J., Stewart, J. G., & Liou, F. W. (2000). Laser metal forming processes for rapid prototyping – A review. *Int. J. Prod. Res.*, 38(16), 3973-3996.
- Lancaster, J. F. *Metallurgy of Welding*; 1993. London, Chapman & Hall.
- Lewis, G. K., & Schlienger, E. (2000). Practical considerations and capabilities for laser assisted direct metal deposition. *Mater. Des.*, 21(4), 417-423.
- Lu, L., & Dahle, A. K. (2005). Iron-rich intermetallic phases and their role in casting defect formation in hypoeutectic Al–Si alloys. *Metall. Mater. Trans. A*, 36(13), 819–835.
- Martukanitz, R. P. (1993). Selection and Weldability of Heat-Treatable Aluminum Alloys. *ASM Handbook*, 6, 528-536.
- Meyers, M., & Chawla, K. (2009). *Mechanical Behavior of Materials*. 2nd Ed. Cambridge: Cambridge University Press.
- Murr, L. E., Gaytan, S. M., Ramirez, D. A., Martinez, E., Hernandez, J., Amato, K. N., Shindo, P. W., Medina, F. R., & Wicker, R. B. (2012). Metal fabrication by additive manufacturing using laser and electron beam melting technologies. *J. Mater. Sci. Tech.*, 28(1), 1-14.
- Nilsiam, Y., Haselhuhn, A., Wijnen, B., Sanders, P. and Pearce, J.M., (2015). Integrated voltage-current monitoring and control of gas metal arc weld magnetic ball-jointed open source 3-D printer. *Mach.*, 3(4), pp.339-351.

- Pearce, J. M., Blair, C. M., Laciak, K. J., Andrews, R., Nosrat, A., & Zelenika-Zovko, I. (2010). 3-D printing of open source appropriate technologies for self-directed sustainable development. *J. Sustain. Dev.*, 3(4), 17–29.
- Pearce, J. M. (2012). Building research equipment with free, open-source hardware. *Science*, 337(6100), 1303-1304.
- Pearce, J. M. (2013). *Open-source lab: How to build your own hardware and reduce research costs*. Elsevier: New York.
- Peels, J. (23 May 2014). Metal 3D printing: From lab to fab. Inside 3DP. Retrieved from <http://www.inside3dp.com/metal-3d-pinting-lab-fab/>.
- Pinar, A. Wijnen, B., Anzalone, G.C., Havens, T.C., Sanders, P.G., & Pearce, J.M. (2015). Low-Cost Open-Source voltage and current monitor for gas metal arc weld 3-D printing. *J. Sens.*, 2015: 8.
- Porter, D.A., Easterling, K.E., & Sherif, M.Y. Phase Transformations in Metals and Alloys. 3rd Edition. 2009. Boca Raton, FL, CRC Press.
- Rasband, W. S., Image J., U.S. National Institutes of Health, Bethesda, Maryland, USA, <http://imagej.nih.gov/ig/>, 1997-2014.
- Ribeiro, F. 3D printing with metals, *Comput. Control Eng. J.*, Vol. 9, no. 1, pp. 31–38, 1998.
- Santos, E. C., Shiomi, M., Osakada, K., & Laoui, T. (2006). Rapid manufacturing of metal components by laser forming. *Int. J. Mach. Tools Manuf.*, 46 (12-13), 1459-1468.

- Sells, E., Smith, Z., Bailard, S., Bowyer, A., & Olliver, V. (2009). RepRap: The Replicating Rapid Prototyper: Maximizing Customizability by Breeding the Means of Production. in F. T. Piller, M. M. Tseng (Eds.), *Handbook of Research in Mass Customization and Personalization: Strategies and concepts. Vol. 1. World Scientific*, pp. 568-580, 2010.
- Shin, I. & Carter, E.A. (2013). Possible origin of the discrepancy of Peierls stresses of fcc metals: First-principles of dislocation mobility in aluminum. *Phys. Rev. B*, 88 (6), 1-10.
- Su, S., Liang, X., Moran, A., & Lavernia, E. J. (1994). Solidification behavior of an Al-6Si alloy during spray atomization and deposition. *Int. J. Rapid Solidif.*, 8(3), 161-177.
- Tiryakioglu, M., & Staley, J.T. (2003). Physical Metallurgy and the Effect of Alloying Additions in Aluminum Alloys. In G.E. Totten & D.S. MacKenzie (Eds.), *Handbook of Aluminum Volume 1* (81-209). New York: Marcel Dekker, Inc.
- Wijnen, Bas. MTU-MOST Franklin, <https://github.com/mtu-most/franklin>, last accessed February 9, 2015.
- Wittbrodt, B. T., Glover, A. G., Laureto, J., Anzalone, G. C., Oppliger, D., Irwin, J. L., & Pearce, J. M. (2013). Life-cycle economic analysis of distributed manufacturing with open-source 3-D printers. *Mechatron.*, 23(6), 713-726.

Wohlers, T., & Caffrey, T. (2014). Wohlers Report 2014 Annual Worldwide Progress Report. Wohlers Associates, Inc. Fort Collins, CO.

Zhao, H., Zhang, G., Yin, Z., & Wu, L. (2011). A 3D dynamic analysis of thermal behavior during single-pass multi-layer weld-based rapid prototyping. *J. Mater. Process. Tech.*, 211(3), 488-495.

Zhao, H., Zhang, G., Yin, Z., & Wu, L. (2012). Three-dimensional finite element analysis of thermal stress in single-pass multi-layer weld-based rapid prototyping. *J. Mater. Process. Tech.*, 212(1), 276-285.

5 Aluminum Alloy Development for GMAW-Based 3-D Printing

5.1 Abstract

Alloy development can simplify low-cost weld-based metal printing for the average user who is not a welder, engineer, or metallurgist by producing easy-to-print aluminum alloys. Previous work evaluated the mechanical and microstructural properties of commercially available aluminum weld alloys (1100, 4043, 4943, 4047, and 5356) (Chapter 4). This study found good properties in all alloys, particularly 4943 and 4047. These alloys were easy to print but could benefit from alloying to increase ductility and to minimize or redistribute porosity.

The 4047 and 4943-based alloys were modified with additions of magnesium, strontium, titanium boride, and combinations thereof. Wedge-shaped castings were used to screen alloying additions over the same ranges of solidification rates as weld-based printing. The alloying additions were most effective at modifying the high-silicon 4047 alloy whereas no change in microstructure was observed in the low-silicon 4943 alloy. Strontium was an effective modifier of the high-silicon alloy. Titanium boride did not have a grain refining effect on aluminum dendrites, although the combination of strontium and titanium boride produced the most refined eutectic structure in the high-silicon alloy.

5.2 Introduction

Previous work has shown that aluminum-silicon weld alloys may benefit most from alloy modification (Chapter 4; Haselhuhn, et al., 2016). Alloys such as 4047 and 4943 were easy to weld and exhibited good mechanical properties. The ductility and strengths of these alloys maybe further improved by a redistribution of porosity, refinement of the eutectic silicon morphology, and grain refinement.

5.2.1 *Eutectic Modification Strategies in Hypoeutectic Al-Si Alloys*

The eutectic structure of hypoeutectic aluminum-silicon alloys is commonly modified from a coarse, sharp, plate-like structure to a fine, fibrous structure with rounded edges to improve mechanical properties such as ductility and to redistribute porosity (Dahle, et al., 2005). A method of modifying the eutectic structure in aluminum-silicon alloys using alkaline fluorides was first patented by Pacz (1920). Since then researchers studied the mechanisms attributed to sodium's ability modify the eutectic structure of aluminum-silicon alloys (Flood & Hunt; 1981; Cross & Olson, 1982; Lu & Hellawell, 1987; and Qiyang, et al., 1991). While effective, effects of sodium were observed to fade rapidly in cast alloys and were difficult to control (Lu & Hellawell, 1995; Liao, et al., 2007). Although typically applied to cast aluminum-silicon alloys, Cross & Olson applied similar practices to modify the eutectic structure of aluminum-silicon weld alloys. Cross & Olson evaluated whether additions of sodium could survive the welding thermal environment in sufficient quantities to interact with the weld solidification mechanisms and produce a refined structure. They observed that even small

additions (0.001 wt% sodium) were sufficient to enhance eutectic modification over that of rapid cooling produced during welding. Thus, methods utilized by the foundry industry to modify aluminum-silicon eutectic structures could be applied to weld alloys.

While sodium is an effective eutectic modifier, its efficacy fades rapidly and can be difficult to control (Lu & Hellawell, 1995; Liao, et al., 2007). Strontium has been identified as a suitable alternative to sodium that is easy to control (Liao, et al., 2007). Additionally, strontium-modified aluminum-silicon alloys melt easily, are difficult to over-modify, and are more stable than sodium-modified alloys (Lu, et al., 2005). In comparing the modification effect of sodium versus strontium, Tiedje, et al., observed both elements to be effective modifiers although the sodium-modified alloy exhibited a finer and more uniform structure than the strontium-modified alloy (2012). On average, they also observed strontium additions to increase porosity in cast aluminum-silicon alloys. Lu, et al., studied the combined effect of both sodium and strontium additions in near eutectic aluminum-silicon alloys but did not observe any additional benefit to using two modifiers (2005).

Based on the comparative work of sodium and strontium modifications, many researchers have studied the effects and mechanisms responsible for strontium modification of aluminum-silicon alloys (Table 5.1). While the fundamental mechanisms for strontium modification are not fully understood (Dahle, et al., 2005), it has been observed that no significant gains in mechanical properties are observed at strontium additions in excess of approximately 300 ppm in a near-eutectic aluminum-silicon alloy (Shin, et al., 2012).

Table 5.1 Strontium Levels in Hypoeutectic Al-Si Alloys as Reported in the Literature

Si Content (wt%)	Sr Content (ppm)	References
10	30-290	Cho, et al., (2008)
7	70-500	Dahle, et al., (2005)
10	0-1000	Dahle, et al., (2001)
1, 9	200	Dinnis, et al., (2005)
10	200	Dinnis, et al., (2004)
5.5	150	Fatahalla, et al., (1999)
12.2	1000	Haque & Maleque (1998)
7	150	Heiberg & Arnberg (2001)
7	100-150	Heiberg, et al., (2002)
9, 11	50-200	Heusler & Schneider (2002)
9	200-600	Kulunk & Zuliani (1996)
11.6	100-375	Liao, et al., (2007)
11.7	300	Liao, et al., (2002)
5, 6, 7, 12	70-245	Liu, et al., (2004)
10	250	Lu & Dahle (2005)
10	150	McDonald, et al., (2004a)
10	30-720	McDonald, et al., (2004b)
10	90-140	McDonald, et al., (2006)
7	50	Nafisi, et al., (2008)
10.2	290	Nogita, et al., (2006)
8.7	400	Shabestari, et al., (2009)
10.5	100-1000	Shin, et al., (2012)
7	400	Sreeja Kumari, et al., (2007)
7	200	Sreeja Kumari, et al., (2008)
3, 12.5	400	Srirangam, et al., (2014)
3, 7, 10, 12.5	400	Srirangam, et al., (2011)
7, 12.5	250-350	Tiedje, et al., (2012)
10	200	Timpel, et al., (2012)
5	50-3000	Zarif, et al., (2010)
5	50-3000	Zarif, et al., (2011)
3	1500-3000	Zhang and Cantor (1993)

Other researchers have studied the effects of antimony on the ability to modify the eutectic structure of cast hypoeutectic aluminum-silicon alloys. Telli and Kisakürek chose to study the eutectic modification effects of antimony as antimony does not suffer the same fading effects as many of the IA and IIA group elements (1986). Uzun, et al.,

found 0.5wt% additions of antimony to a near-eutectic aluminum-silicon alloy to be effective at eutectic modification and improved mechanical properties, although additions of 1.0wt% allowed for the precipitation of primary silicon that was detrimental to mechanical properties (2011). Xiufang, et al., also found antimony to be effective at modifying the eutectic structure of near-eutectic aluminum-silicon alloys (2001). Fatahalla, et al., compared the effects of sodium, strontium, and antimony on eutectic modification (1999). Fatahalla, et al., found that the use of antimony as a modifying agent resulted in a lamellar eutectic structure whereas the use of sodium or strontium produced a finely spaced fibrous structure. The lamellar structure resulted in a combination of brittle and ductile fracture whereas the fibrous structure produced completely ductile fracture in tension. While antimony may be effective, its use can produce toxic byproducts that limit its use in the foundry industry (Kori, et al., 2000). In addition to antimony, group IIA elements, transition elements, and rare earth elements have been evaluated by other researchers (Knuutinen, et al., 2001a; Knuutinen, et al., 2001b; Nogita, et al., 2001; Nogita, et al., 2004; Sreeja Kumari, et al., 2007; & Sreeja Kumari, et al., 2008).

5.2.2 Grain Refinement in Hypoeutectic Aluminum-Silicon Alloys

Strontium has been observed to be an effective modifier of the eutectic structure of hypoeutectic aluminum-silicon alloys, but can result in enlarged, columnar dendrites which is disadvantageous for mechanical properties (Liao, et al., 2002). A review of the grain refinement mechanisms proposed for Al-Ti-B additions in aluminum silicon alloys was presented by Easton and StJohn (1999a). Although prior literature debated whether

grain nucleation occurred on TiB_2 , AlB_2 , $(\text{Ti,Al})\text{B}_2$, or Al_3Ti phases, experimental work performed by Easton and StJohn with aluminum castings provided evidence that grain nucleation occurred on TiB_2 phases and the optimum amount of Al-5Ti-1B additions was to 0.05wt% Ti (1999a; 1999b). The Al-5Ti-1B master alloy has approximately equal ratios of titanium and boron in atomic percent, resulting in an excess of titanium that has been shown to improve the grain refining effect of TiB_2 (Easton and StJohn, 1999a; Easton and StJohn, 1999b). The addition of Al-5Ti-1B to a strontium-modified Al-10Si-0.35Mg alloy was observed to be effective at modifying the eutectic structure while refining grain sizes (Lu & Dahle, 2006). Mallapur, et al., also observed improved mechanical properties in an Al-Ti-B grain-refined, strontium-modified A356 aluminum alloy (2010). Murty, et al, observed that at traditional Al-5Ti-1B additions of 0.01wt% Ti in aluminum alloys may be ineffective when silicon is present in the alloy due to a mutual poisoning effect (2002). The poisoning effect could not be fully explained, but Al-5Ti-1B additions in excess of 0.01wt% Ti were suggested in the presence of silicon. Lee, et al., observed that for high silicon levels (8wt% or higher), that no significant reductions in grain size were observed beyond Al-5Ti-1B additions to 0.5wt% Ti (1999).

5.2.3 Alloying Considerations for Welding

The chemistries of aluminum weld alloys are designed to achieve optimal mechanical properties when diluted with a base metal during welding (Martukanitz, 1993). However, in weld-based 3-D printing, there is no dilution of the weld filler metal with a base metal. The design of an optimal alloy for weld-based 3-D printing must avoid alloying additions that commonly cause cracking in welds (Figure 5.1) while also having

the ability to be printed into a part with good microstructural and mechanical properties with no assistance from dilution (Dickerson, 1993).

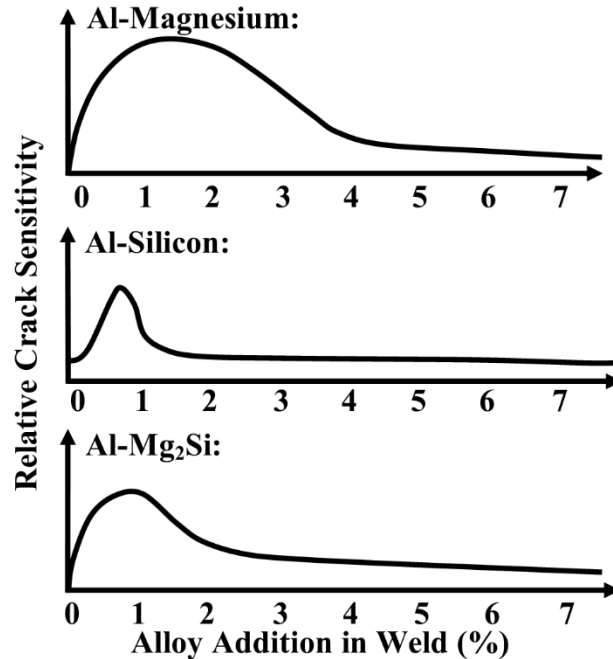


Figure 5.1 Influence of alloying additions on the weld crack susceptibility in aluminum welds. (Modified from Dickerson, 1993)

As solidification range increases, crack susceptibility also increases (Lancaster, 1993). Alloying additions that increase the solidification range increase crack susceptibility and should be avoided. By contrast, good starting points for alloy modifications may lie in regions on the phase diagram with short solidification ranges such as compositionally pure and eutectic compositions. Grain refinement, such as adding titanium boride in aluminum alloys, has also been shown to reduce cracking susceptibility (Lancaster, 1993). Alloying additions that cause the formation of brittle

structures such as aluminum-iron intermetallics or magnesium disilicides can also limit weld performance and should be avoided.

5.2.4 The Role of Wedge Castings in Alloy Development

Wedge-shaped castings are a novel method to evaluate the effect of solidification rate upon mechanical and microstructural properties of aluminum alloys as a wide range of solidification rates can be induced in a single casting. Caton, et al., evaluated the cracking susceptibility of two aluminum-silicon-copper alloys cast into a wedge shape designed to induce a wide range of solidification rates (1999). Boileau and Allison later used the wedge-shaped mold developed by Caton, et al., to evaluate the influence of solidification rate on the fatigue properties in aluminum-silicon-copper alloys for light-weight vehicle components (2003). Wedge-shaped castings have also allowed researchers to efficiently evaluate the temperature-dependence of microstructural evolution in aluminum-iron-silicon alloys (Stone & Jones, 1997), aluminum-magnesium-silicon alloys (Ourfali, et al., 2005; Zhang, et al., 2000), aluminum-manganese alloys (Juarez-Islas, et al., 1989), aluminum rich alloys alloyed with lanthanide series elements (Hawksworth, et al., 1999), and in metallic glasses (Perepezko and Hildal, 2006).

Norman, et al., proposed a wedge casting to evaluate many different amounts of scandium additions to aluminum under a wide range of solidification temperatures (1998). Norman, et al., later extended this work to evaluate scandium's influence on the grain refinement and weldability of 2000 and 7000 series aluminum alloys (2003). In their 2003 study, Norman, et al., were able to successfully cast aluminum-scandium alloys at solidification rates comparable to those observed in fusion welding.

The approach of Norman, et al., to evaluate the influence of alloying elements on weldability, was extended to this study to screen several alloy modifications for GMAW-based 3-D printing (2003). Initial proof-of-concept work identified the lower 1/3 of the wedge closest to the wedge tip as the region of interest for 3-D printed cooling rates although these cooling rates could not be verified using cast thermal modeling software Magma. Previous work identified 4047 and 4943 alloys as good-performing alloys in a 3-D printing environment that could still benefit from additional alloying (Chapter 4; Haselhuhn, et al., 2016). Common modifiers to aluminum-silicon alloys, strontium and titanium boride, were evaluated for their ability to reduce porosity and further increase ductility of 3-D printed materials.

5.3 Hypotheses

Hypothesis 1: If magnesium is added to an 11.6% aluminum-silicon alloy then porosity will increase because magnesium has a high affinity for hydrogen and oxidizes easily, acting as nucleation sites for porosity.

Hypothesis 2: If strontium is added to aluminum-silicon alloys, then porosity will increase, because strontium increases the solubility of hydrogen gas in an aluminum-silicon melt.

Hypothesis 3: If magnesium is added to an 11.6% aluminum-silicon alloy then yield strength will increase, because magnesium has a solid solution strengthening effect in aluminum.

Hypothesis 4: If strontium is added to aluminum-silicon alloys, then elongation at break will increase, because the eutectic structure will be modified and refined and porosity will be finely distributed, resulting in greater ductility.

5.4 Materials & Methods

5.4.1 Description of Permanent Mold

The permanent mold used in this study was a wedge shaped casting modified from Norman, et al. (Figure 5.2) (1998).

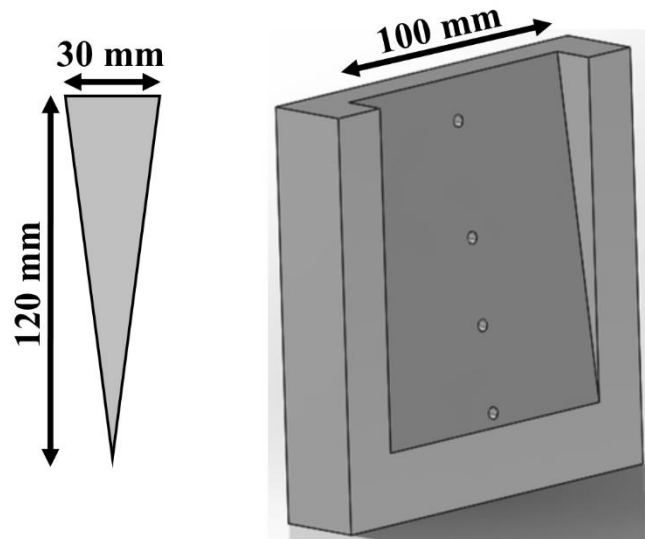


Figure 5.2 Schematic drawings of the wedge casting and permanent mold. Wedge profile (left) and the modified permanent mold (right).

This mold was chosen as it could induce a wide range of cooling rates, allowing for comparisons between cast alloys and 3-D printed alloys. The mold was machined from two 99.00% copper bars rather than four pieces used by Norman, et al. (1998). There

were no differences in the overall size of the mold or the wedge casting in this study as compared to that used by Norman, et al. (1998). The four holes for thermocouple insertion were moved from the end of the mold to the side to allow for cooling rate measurement from the centerline of the wedge while minimizing the length of thermocouple within the mold. The holes were decreased in size from 4 mm diameter in the mold used by Norman, et al., to 2.25 mm in diameter. This change in size provided a tight fit for the Type K thermocouples used in this study with a protective stainless steel sheath (0.25 mm wall thickness).

5.4.2 Alloy Melting & Pouring

Eleven alloys based upon 4047 (approximately 11.6 wt% Si) and 4943 (with approximately 5.5 wt% Si and 0.3 wt% Mg) were analyzed in this study (Table 5.2). Additions of magnesium, strontium, titanium boride, and combinations thereof were evaluated for the influence on the microstructural and mechanical properties of aluminum-silicon alloys similar to 4047 and 4943.

Table 5.2 Target Compositions of Experimental Alloys. All values given in wt%.

Si	Mg	Sr	Ti	Al
10.8-12.4	-	-	-	Bal.
10.8-12.4	0.2-0.5	-	-	Bal.
10.8-12.4	0.2-0.5	0.02-0.04	-	Bal.
10.8-12.4	0.2-0.5	-	0.04-0.06	Bal.
10.8-12.4	-	0.02-0.04	0.04-0.06	Bal.
10.8-12.4	0.2-0.5	0.02-0.04	0.04-0.06	Bal.
5-6	0.2-0.5	-	-	Bal.
5-6	0.2-0.5	0.02-0.04	-	Bal.
5-6	0.2-0.5	-	0.04-0.06	Bal.
5-6	-	0.02-0.04	0.04-0.06	Bal.
5-6	0.2-0.5	0.02-0.04	0.04-0.06	Bal.

99.999% pure aluminum and Al-36wt%Si charge materials were preheated in a silica crucible in a resistance box furnace for 1 hour at 300°C to drive off any oils or organic materials that could increase porosity in the melt. Following preheat, the crucible and preheated charge material were moved into a Thermolyne type 46200 high temperature furnace. This furnace had two argon gas inlets: One directly to the top of the melt surface and one in the bottom of the furnace. 99.999% pure argon gas was flowed through both gas inlets at approximately 0.05 L/sec.

Once molten, approximately 1 hour after being placed in the Thermolyne furnace, the crucible was pulled out of the furnace and the melt was stirred thoroughly with a stainless steel probe. The crucible was placed back in the furnace and allowed to reheat for 5 minutes prior to pouring a small button for chemical verification via optical emission spectrometry (OES). The button surface was ground smooth with a lathe. A minimum of three burns were used to verify alloy chemistry. Each alloy was monitored for silicon, iron, magnesium, titanium, boron, and strontium levels. Based upon initial chemical analysis, the chemistry was corrected and alloying additions (Al-50wt%Mg, Al-10wt%Sr, and/or Al-5wt%Ti-1wt%B) were stirred into the melt. The melt was allowed to sit in the furnace for 5 minutes to allow for dissolution of alloying additions.

The alloy was stirred thoroughly and a boron nitride coated stainless steel cup was used to scoop an approximately 4 fluid ounce specimen. The cup was placed in an insulating support and a thermocouple was inserted into the center of the melt for cooling rate analysis. The crucible was stirred while verifying the melt temperature was above 650°C. A second OES button was poured and immediately following this, the first wedge

casting was poured, and the crucible was returned to the furnace. The casting was allowed to cool in the mold until all four thermocouples read less than 400°C. The melt was stirred again prior to pouring the second wedge, returned to the furnace, and stirred again prior to pouring the third wedge. A third OES button was poured after the third wedge to verify the initial wedge chemistry and the final wedge chemistry were within the target range.

5.4.3 Alloy Testing & Analysis

One wedge of each alloy was sectioned into four pieces for microstructural analysis (Figure 5.3).

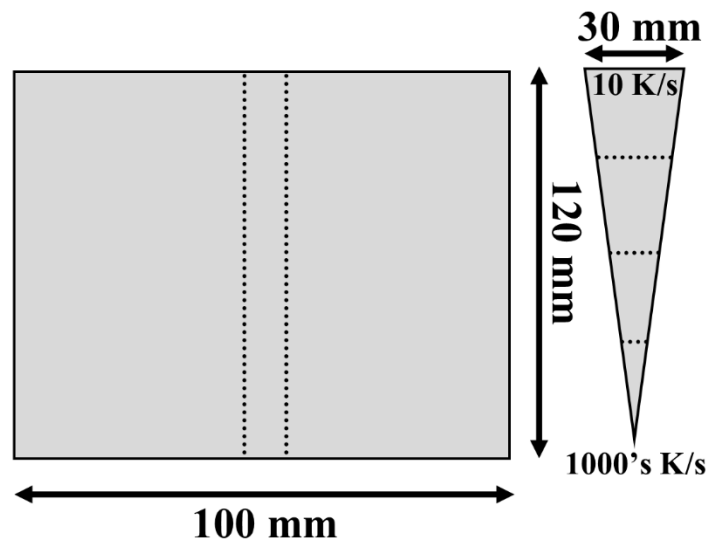


Figure 5.3 Schematic drawing of the wedge castings with dashed lines to represent cut sections.

The sections were mounted in epoxy, polished to 0.05 μm surface finish using silica, and etched for microstructural analysis using Keller's solution for 30 seconds. Secondary dendrite arm spacing (SDAS) was measured and corresponding cooling rates calculated as described in section 4.4.3 (Equation 4.2-4.3). This analysis indicated that the SDAS corresponding to that reported for 3-D printed specimens (Chapter 4) was in the region approximately 25-50 mm above the wedge tip and close to the wedge sides.

Two subsize rectangular tensile specimens were machined from both of the remaining wedges (Figure 5.4) (ASTM B557, 2013).

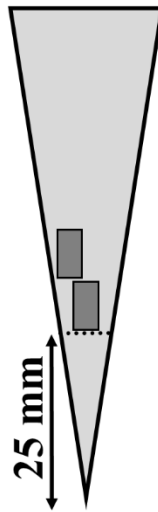


Figure 5.4 Schematic drawing showing the approximate origin of tensile bars.

Prior to tensile testing, the internal (closed) porosity of the tensile specimens was measured in water using the Archimedes' method as described previously (Chapter 3; Haselhuhn, et al., 2015). Tensile specimens were pulled to failure at a strain rate of 10^{-3}

sec⁻¹ according to ASTM B557 as described previously (Chapter 4; Haselhuhn, et al., 2016). Only specimens that broke within the gauge section were used for further analysis.

5.5 Results

5.5.1 Microstructural Analysis

The unmodified high-silicon alloy and the high-silicon alloys modified with magnesium and titanium boride exhibited primary silicon precipitates near to or surrounded by primary aluminum dendrites (Figure 5.5). Alloys modified with strontium exhibited a cleaner and more refined microstructure.

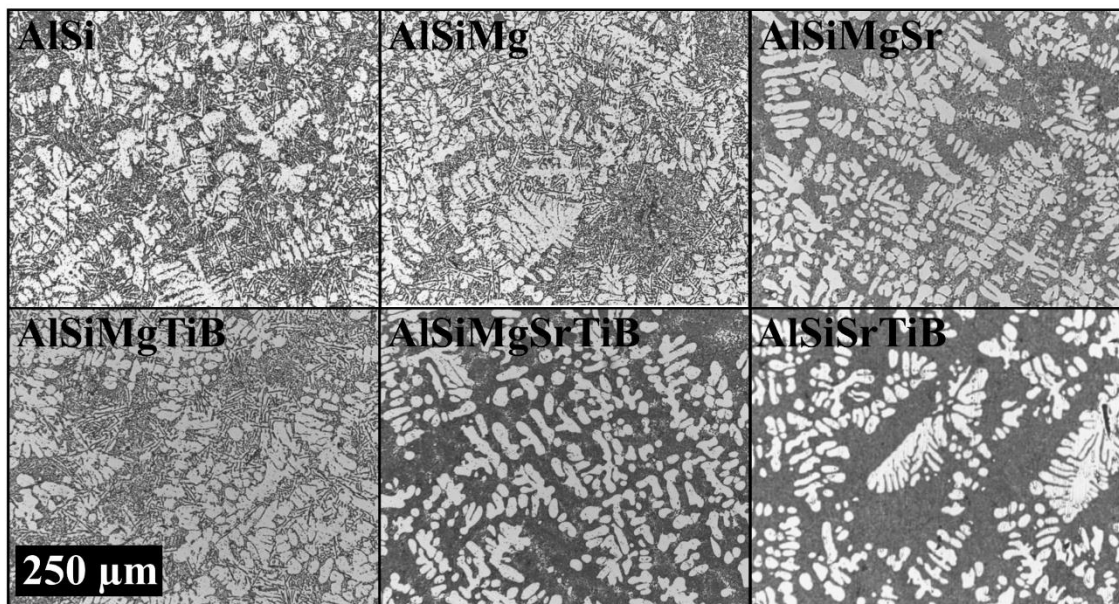


Figure 5.5 Comparative microstructures of the high-silicon alloys. Scale bar represents 250 μ m in all images.

The eutectic structure of alloys not containing strontium was coarse and consisted of flakes with sharp edges (Figure 5.6). The addition of strontium significantly refined the

eutectic structure of the high-silicon alloys in terms of overall size and length. Strontium also rounded the eutectic edges. Alloys containing both strontium and titanium boride exhibited a finer eutectic structure than alloys only modified with strontium. However, the combination of strontium and titanium boride allowed aluminum growth in the magnesium containing alloy but this aluminum growth less pronounced in the strontium-titanium boride alloy that did not contain magnesium.

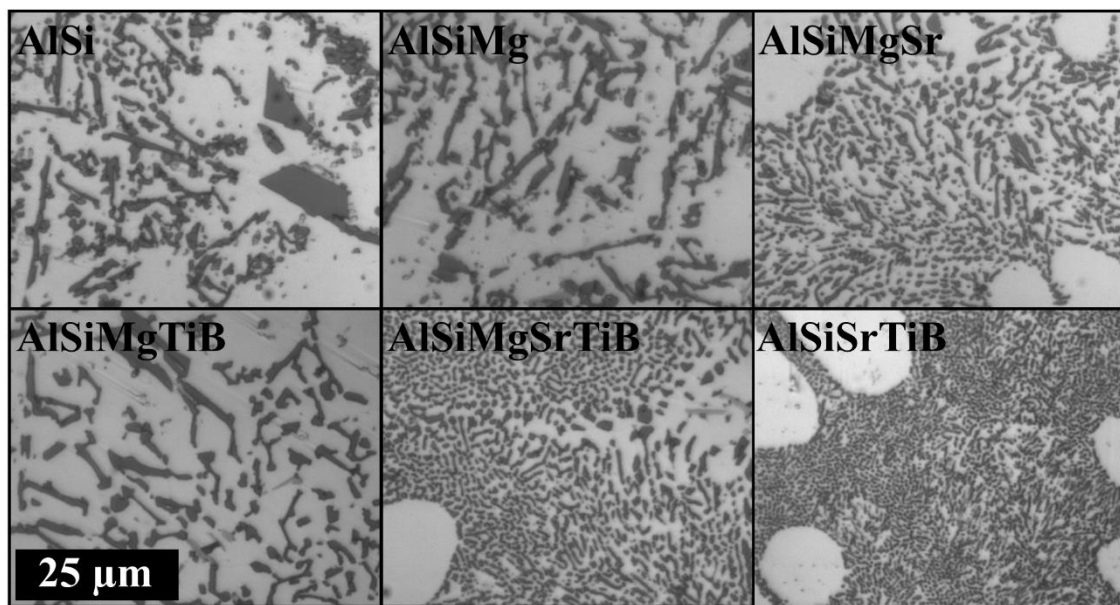


Figure 5.6 Comparative eutectic microstructures of the high-silicon alloys. Scale bar represents 25μm in all images.

Few differences were observed in the microstructure of the low-silicon alloy (Figure 5.7). The dendritic and eutectic structures of the Al-5.5Si-0.03Sr-0.05TiB alloy appeared to be more refined than in the other low-silicon alloys. Additionally, the

eutectic phase appeared to form larger colonies in the Al-5.5Si-0.03Sr-0.05TiB alloy than in the other alloys.

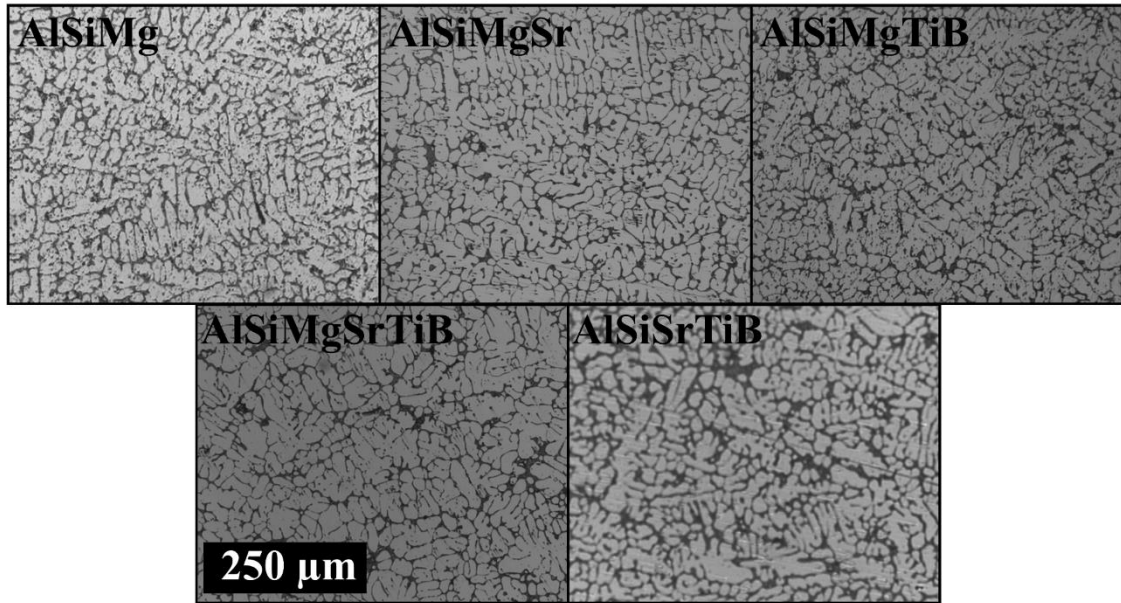


Figure 5.7 Comparative microstructures of the low-silicon alloys. Scale bar represents 250 μ m in all images.

No significant differences were observed upon closer examination of the low-silicon alloy eutectic phases (Figure 5.8). The eutectic structures of all alloys appeared to be small and with rounded edges, similar to the strontium modified high-silicon alloys.

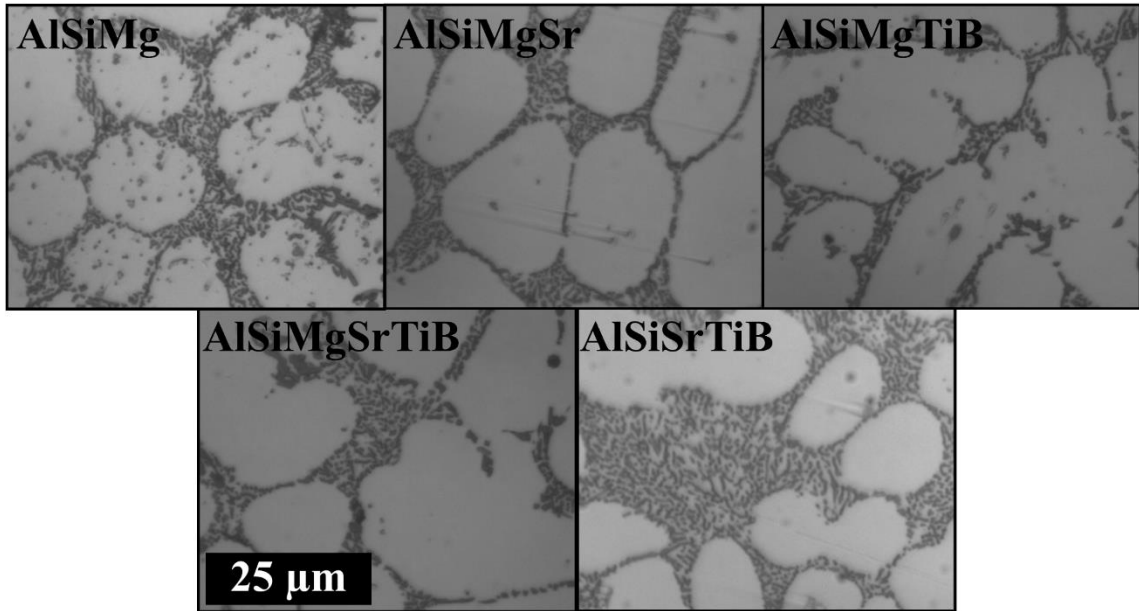


Figure 5.8 Comparative eutectic microstructures in the low-silicon alloys. Scale bar represents 25 μ m in all images.

5.5.2 Mechanical Properties

All alloys exhibited porosities of 0.4% or less (Figure 5.9). The porosity of the low-silicon alloy was lower than that for the high-silicon alloy. Magnesium additions significantly increased porosity levels in the high-silicon alloy. Additions of strontium or titanium boride to magnesium-containing alloys further increased porosity levels, although porosity levels significantly decreased when both strontium and titanium boride were added to magnesium-containing alloys.

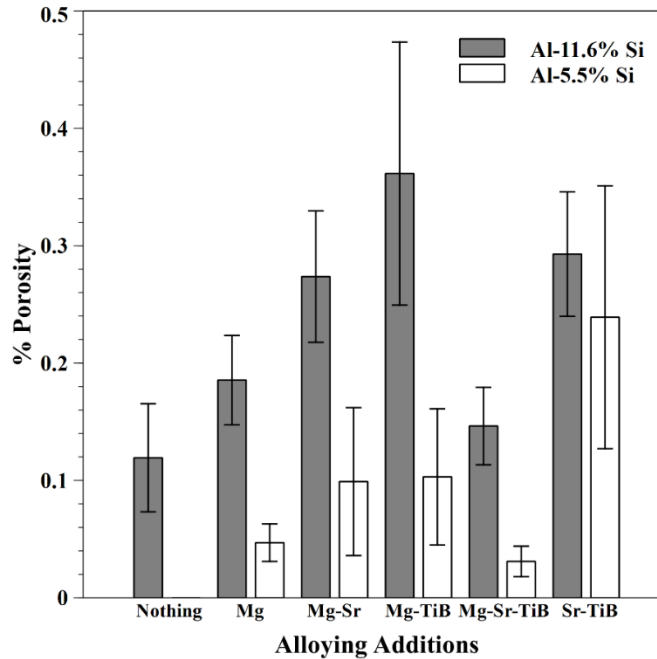


Figure 5.9 Average porosity of the cast experimental alloys. Error bars represent ± 2 standard error.

Few significant differences were observed in the yield strengths of either aluminum-silicon alloy (Figure 5.10). Any modification to the high-silicon alloy (magnesium, strontium, and/or titanium boride) significantly increased the yield strength. Low-silicon alloys containing magnesium exhibited higher yield strengths than the low-silicon that did not contain magnesium. There were no differences in the yield strengths of the high or low-silicon alloys that contained magnesium.

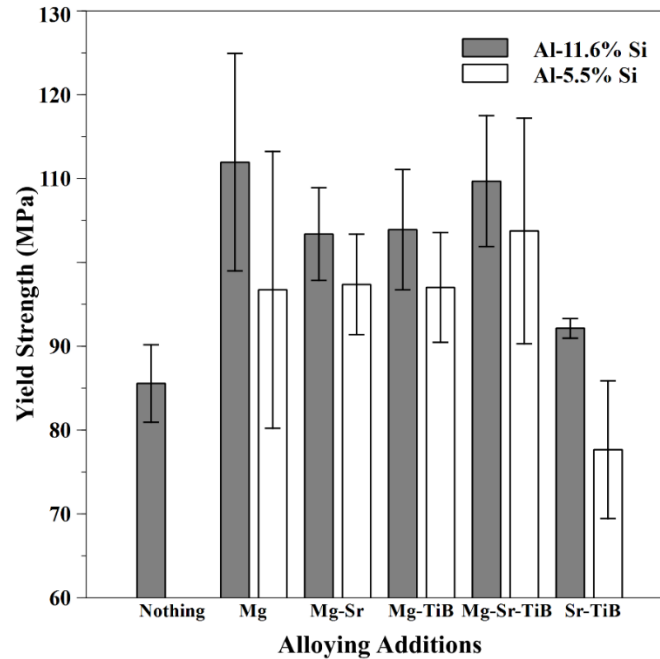


Figure 5.10 Average 0.02% offset yield strength of the cast experimental alloys. Error bars represent ± 2 standard error.

The additions of magnesium-strontium, magnesium-strontium-titanium boride, and strontium-titanium boride provided the highest ultimate tensile strength in the high-silicon alloy (Figure 5.11). Low-silicon alloys that did not contain titanium boride exhibited higher ultimate tensile strengths than low-silicon alloys containing titanium boride. The low-silicon magnesium, magnesium-strontium, and magnesium-titanium boride alloys exhibited higher ultimate tensile strengths than their high-silicon counterparts. In contrast, the high-silicon strontium-titanium boride alloy had a higher ultimate tensile strength than its low-silicon counterpart.

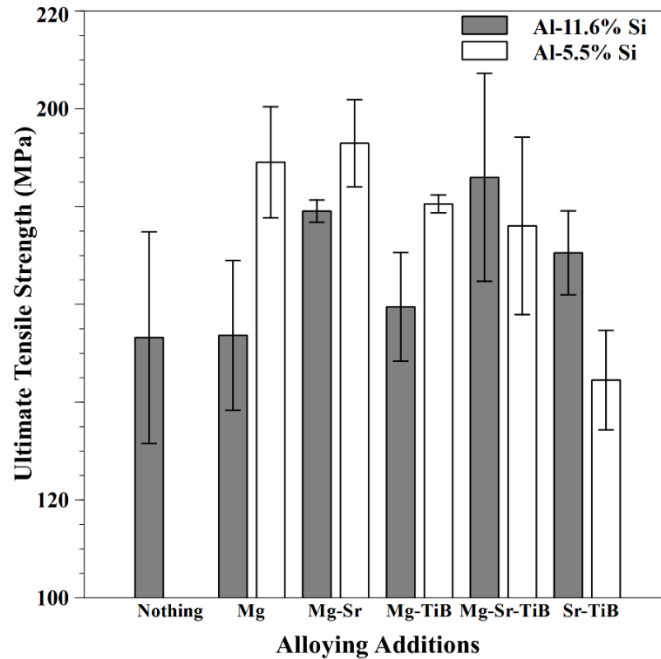


Figure 5.11 Average ultimate tensile strength of the cast experimental alloys. Error bars represent ± 2 standard error.

The low-silicon alloys exhibited greater ductility as greater variability in their performance than the high-silicon alloys (Figure 5.12). Magnesium additions worsened the ductility of high-silicon alloys, although ductility could be recovered with strontium additions. Titanium boride worsened the ductility of magnesium-containing low-silicon alloys. On average, the strontium-titanium boride alloys exhibited the greatest ductility when magnesium was not present. The low-silicon alloys exhibited higher quality indexes on average than the high-silicon alloys. However, the high-silicon alloy containing titanium boride and strontium additions, with and without magnesium, exhibited quality indexes that were statistically equivalent to the low-silicon alloys.

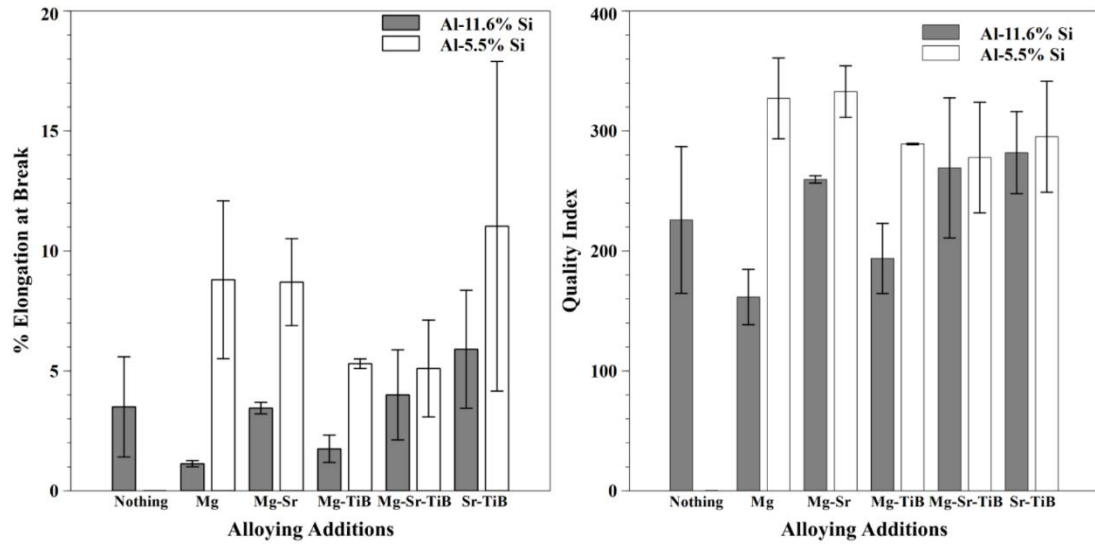


Figure 5.12 Average elongation at break of the cast experimental alloys and corresponding quality index. Error bars represent ± 2 standard error.

5.5.3 Thermal Analysis

The low-silicon alloys exhibited larger solidification ranges than the high-silicon alloys (Figure 5.13). The low-silicon alloys also exhibited lower eutectic growth temperatures and shorter eutectic growth times than the high-silicon alloys (Figure 5.14). All modifications decreased the eutectic growth temperature of the high-silicon alloy, whereas titanium boride additions increased the eutectic growth temperature of the low-silicon alloy. Strontium additions decreased eutectic growth temperatures more than any other alloying modification. In the high-silicon alloy, there was almost no difference in the cooling response of the magnesium-titanium boride alloy and the strontium-titanium boride alloy, and these curves could not be distinguished from one another.

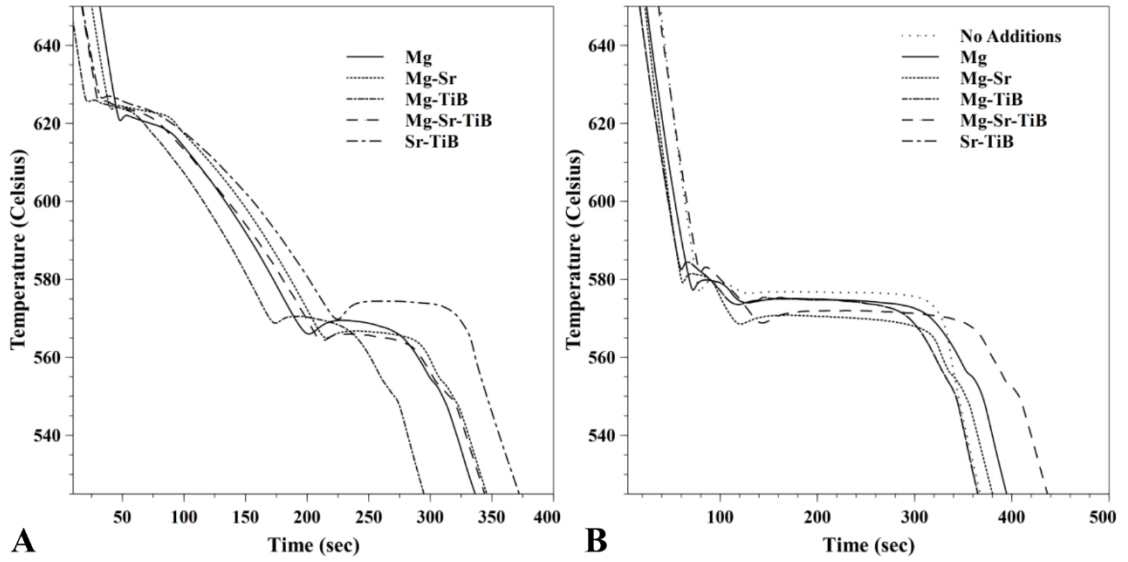


Figure 5.13 Cooling curves of cast alloys. Al-5.5% Si alloys (left) and Al-11.6% Si alloys (right).

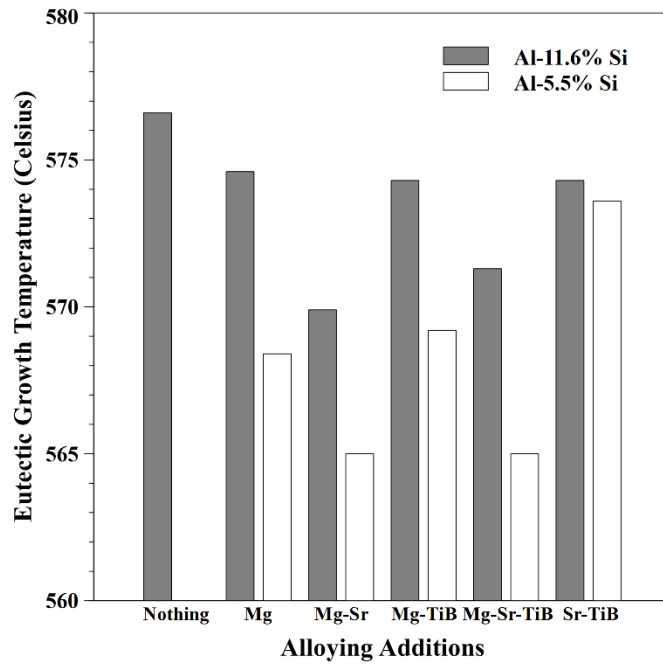


Figure 5.14 Eutectic growth temperature of cast alloys.

5.6 Discussion

Strontium was an effective eutectic modifier in the high-silicon alloy. No significant differences in grain refinement were observed between the alloys treated with and without Al-5Ti-1B. However, the combination of strontium and Al-5Ti-1B produced the most refined eutectic structure. It is possible that the application of strontium and Al-5Ti-1B in a near-eutectic aluminum-silicon weld alloy may illicit more grain refining effect than in an analogous cast alloy.

No significant differences were observed in the microstructures of the low-silicon alloys. Therefore, large differences in mechanical properties were not anticipated or observed. The short eutectic growth time in the low-silicon alloys resulted in a fine silicon eutectic structure. A reduction in the size and aspect ratio of silicon particles in aluminum-silicon particles has been previously reported with faster cooling rates (Wang, 2003). Magnesium additions to aluminum-silicon alloys results in solid solution strengthening, explaining why the Al-5.5Si-Sr-TiB alloy exhibited weaker yield and ultimate tensile strengths than magnesium-containing alloys.

The higher porosity in the high-silicon alloys limited mechanical properties such as ultimate tensile strength and ductility. Pores act as stress concentrators and can cause materials to prematurely fail in tension. It was originally expected that the low-silicon alloy would exhibit higher porosity due to lack of interdendritic feeding between closely spaced dendrites (Kou, 1987). However, it was observed during melting that there was interaction between the aluminum-silicon melt and the silica crucibles and this reaction increased with increasing silicon levels in the melt. These silica levels could contribute to

porosity by allowing for heterogeneous nucleation of pores. Magnesium oxidizes easily and magnesium oxide additions can also contribute to porosity by serving as heterogeneous nucleation sites for pores (Tiryakioglu & Staley, 2003). Thus, it was expected that magnesium-containing high-silicon alloys would exhibit higher porosities than the alloy without magnesium. However, with 95% confidence, this hypothesis could not be confirmed, and null hypothesis 1 was not rejected. The null hypothesis stating strontium would have zero effect on porosity levels could be rejected with 95% confidence, as strontium significantly increased porosity levels in the high-silicon alloy.

There were few differences among the yield and ultimate tensile strengths of the experimental alloys studied. All modified high-silicon alloys exhibited greater yield strengths than the non-modified alloy. The high and low-silicon alloys benefited from magnesium additions as the Al-Si-Sr-TiB alloys exhibited lower yield strengths. There were no significant differences in ultimate tensile strengths among the high-silicon alloy. The low-silicon Al-Si-Sr-TiB alloy that did not contain magnesium exhibited lower ultimate tensile strength than its magnesium-containing counterparts. With 95% confidence and a p-value less than 0.05 null hypothesis 3 stating that magnesium was have zero effect on the high-silicon alloy could be rejected and alternative hypothesis 3 was accepted.

There were also few differences in elongation at break amongst the alloys. The addition of strontium to a high-silicon alloy with magnesium increased ductility. In aluminum-silicon alloys, ductility is limited by cracking of the silicon eutectic particles (Wang, et al., 2003). Wang, et al., observed that cracking in A356 and A357 cast

aluminum alloys was most prominent in silicon particles with large aspect ratios, limiting tensile properties (Wang, et al., 2003; Wang, 2003). Modification of A356 and A357 cast aluminum alloys with strontium was observed to decrease the overall size and aspect ratio of the silicon eutectic particles (Wang, 2003). The smaller, sphere-like silicon particles limiting stress concentration and cracking, ultimately leading to greater ductility in the alloy (Wang, et al., 2003b). Additionally, the small, refined eutectic phases in the strontium-modified Al-Si-Mg alloy resulted in smaller barriers for dislocation motion, resulting in increased elongation at break. The low-silicon alloys exhibited greater elongation at break than the high-silicon alloys, except when strontium and titanium boride were added to the alloys. Therefore, with 95% confidence null hypothesis 4 stating there was no difference in elongation at break with the addition of strontium could not be rejected.

The depression in eutectic temperature with magnesium additions has been reported by Heusler and Schneider (2002). They observed a magnesium addition of 0.35wt% in an Al-11Si alloy to reduce the eutectic temperature from 577°C to approximately 575°C. This same trend was observed in this study upon the addition of 0.3wt% magnesium to an Al-11.6Si alloy. Heusler and Schneider also observed a decrease in eutectic temperature upon the addition of strontium (2002). The depression in eutectic temperature was observed in strontium-modified Al-10Si alloys that did not contain magnesium (Dahle, et al., 2005; McDonald, et al., 2004a). This depression in eutectic growth temperature allows for a faster growth velocity that allows for a modified eutectic structure to grow (McDonald, et al., 2004a). A single accepted explanation for

the decrease in eutectic temperature with the addition of modifying elements does not exist. However, it has been proposed that a decrease in eutectic temperature indicates an increase in the difficulty and location of eutectic nucleation (Dahle, et al., 2005).

5.7 Conclusions

In order to develop an easy-to-print aluminum alloy, previous work indicated that 4047 and 4943 weld alloys may benefit the most from further alloying modifications. Wedge-shaped castings were used to screen alloying additions to 4047 and 4943-based weld alloys to improve mechanical properties such as ductility and to redistribute porosity. Wedge-shaped castings allowed researchers to induce the same solidification rates during casting as during weld-based 3-D printing. The addition of magnesium, strontium, titanium boride, and combinations thereof were evaluated for their influence on microstructural and mechanical properties.

The modified high-silicon alloy (4047) exhibited the greatest change in microstructure whereas the modified low-silicon alloy (4943) did not exhibit changes in microstructure after modification. Strontium was observed to be an effective eutectic-modifier in the high-silicon alloy. While no grain refinement was observed, the combination of strontium and titanium boride in the high-silicon produced the finest eutectic structure. High porosity levels limited the mechanical properties of the high-silicon alloy. However, the alloys containing both strontium and titanium boride without the presence of magnesium exhibited the greatest ductility on average. Future work should evaluate the singular effects of strontium, titanium boride, and the combination of strontium and titanium boride in weld-based 3-D printing.

5.8 References

- ASTM B557-02. Standard Test Methods for Tension Testing Wrought and Cast Aluminum- and Magnesium-Alloy Products. ASTM International, West Conshohocken, PA, 2013, www.astm.org.
- Boileau, J.M., & Allison, J.E. (2003). The effect of solidification time and heat treatment on the fatigue properties of a cast 319 aluminum alloy. *Metallurgical and Materials Transactions A*. 34(9): 1807-1820.
- Caton, M.J., Jones, J.W., Boileau, J.M., & Allison, J.E. (1999). The effect of solidification rate on the growth of small fatigue cracks in a cast 319-type aluminum alloy. *Metallurgical and Materials Transactions A*. 30(12): 3055-3068.
- Cho, Y. H., Lee, H.-C., Oh, K. H., & Dahle, A. K. (2008). Effect of Strontium and Phosphorus on Eutectic Al-Si Nucleation and Formation of β -Al₅FeSi in Hypoeutectic Al-Si Foundry Alloys. *Metallurgical and Materials Transactions A*. 39(10): 2435–2448.
- Cross, C. E., & Olson, D. L. (1982). Modification of Eutectic Weld Metal Microstructure. *Welding Journal*. 61: 381s–387s.
- Dahle, A. K., Nogita, K., McDonald, S. D., Zindel, J. W., & Hogan, L. M. (2001). Eutectic nucleation and growth in hypoeutectic Al-Si alloys at different strontium levels. *Metallurgical and Materials Transactions A*. 32(4): 949–960.

- Dahle, A. K., Nogita, K., McDonald, S. D., Dinnis, C., & Lu, L. (2005). Eutectic modification and microstructure development in Al–Si Alloys. *Materials Science and Engineering: A*. 413–414: 243–248.
- Dickerson, P. B. (1993). Welding of Aluminum Alloys. ASM Handbook, 6, 722-739.
- Dinnis, C. M., Dahle, A. K., Taylor, J. A., & Otte, M. O. (2004). The influence of strontium on porosity formation in Al-Si alloys. *Metallurgical and Materials Transactions A*. 35(11): 3531–3541.
- Dinnis, C. M., Dahle, A. K., & Taylor, J. A. (2005). Three-dimensional analysis of eutectic grains in hypoeutectic Al–Si alloys. *Materials Science and Engineering: A*. 392(1–2): 440–448.
- Easton, M., & StJohn, D. (1999a). Grain refinement of aluminum alloys: Part I. the nucleant and solute paradigms—a review of the literature. *Metallurgical and Materials Transactions A*, 30(6): 1613–1623.
- Easton, M., & StJohn, D. (1999b). Grain refinement of aluminum alloys: Part II. Confirmation of, and a mechanism for, the solute paradigm. *Metallurgical and Materials Transactions A*, 30(6): 1625–1633.
- Fatahalla, N., Hafiz, M., & Abdulkhalek, M. (1999). Effect of microstructure on the mechanical properties and fracture of commercial hypoeutectic Al-Si alloy modified with Na, Sb and Sr. *Journal of Materials Science*. 34(14): 3555–3564.

- Flood, S. C., & Hunt, J. D. (1981). Modification of Al-Si eutectic alloys with Na. *Metal Science*. 15(7): 287–294.
- Haque, M. M., & Maleque, M. A. (1998). Effect of process variables on structure and properties of aluminium–silicon piston alloy. *Journal of Materials Processing Technology*. 77(1–3): 122–128.
- Haselhuhn, A. S., Wijnen, B., Anzalone, G.C., Sanders, P.G., & Pearce, J.M. (2015). In situ formation of substrate release mechanisms for gas metal arc weld metal 3-D printing. *Journal of Materials Processing Technology*, 226, 50-59.
- Haselhuhn, A.S., Buhr, M.W., Wijnen, B., Sanders, P.G., & Pearce, J.M. (2016). Structure-property relationships of common aluminum weld alloys utilized as feedstock for GMAW-based 3-D printing. *Materials Science & Engineering: A*. Accepted.
- Hawksworth, A., Rainforth, W. M., & Jones, H. (1999). Solidification microstructure selection in the Al-rich Al–La, Al–Ce and Al–Nd systems. *Journal of Crystal Growth*. 197(1): 286-296.
- Heiberg, G., & Arnberg, L. (2001). Investigation of the microstructure of the Al–Si eutectic in binary aluminium–7 wt% silicon alloys by electron backscatter diffraction (EBSD). *Journal of Light Metals*. 1(1): 43–49.

- Heiberg, G., Nogita, K., Dahle, A. K., & Arnberg, L. (2002). Columnar to equiaxed transition of eutectic in hypoeutectic aluminium–silicon alloys. *Acta Materialia*. 50(10): 2537–2546.
- Heusler, L., & Schneider, W. (2002). Influence of alloying elements on the thermal analysis results of Al–Si cast alloys. *Journal of Light Metals*. 2(1): 17–26.
- Juarez-Islas, J. A., Warrington, D. H., & Jones, H. (1989). Formation of stable and metastable phases in Al–Mn alloys by the use of a gravity chill casting technique. *Journal of materials science*. 24(6): 2076-2080.
- Knuutinen, A., Nogita, K., McDonald, S. D., & Dahle, A. K. (2001a). Modification of Al–Si alloys with Ba, Ca, Y and Yb. *Journal of Light Metals*. 1(4): 229–240.
- Knuutinen, A., Nogita, K., McDonald, S. D., & Dahle, A. K. (2001b). Porosity formation in aluminium alloy A356 modified with Ba, Ca, Y and Yb. *Journal of Light Metals*. 1(4): 241–249.
- Kori, S. A., Murty, B. S., & Chakraborty, M. (2000). Development of an efficient grain refiner for Al–7Si alloy and its modification with strontium. *Materials Science and Engineering: A*. 283(1–2): 94–104.
- Kou, S. (1987). *Welding Metallurgy*. New York: John Wiley & Sons.
- Kulunk, B., & Zuliani, D. J. (1996). Applications for the strontium treatment of wrought and die-cast Al. *JOM*. 48(10): 60–63.
- Lancaster, J. F. *Metallurgy of Welding*; 1993. London, Chapman & Hall.

- Lee, Y. C., Dahle, A. K., StJohn, D. H., & Hutt, J. E. C. (1999). The effect of grain refinement and silicon content on grain formation in hypoeutectic Al–Si alloys. *Materials Science and Engineering: A*. 259(1): 43–52.
- Liao, H., Sun, Y., & Sun, G. (2002). Correlation between mechanical properties and amount of dendritic α -Al phase in as-cast near-eutectic Al–11.6% Si alloys modified with strontium. *Materials Science and Engineering: A*. 335(1–2): 62–66.
- Liao, H., Dong, G., & Sun, G. (2007). Investigation on influence of sodium- or strontium-modification on corrosion-resistance of Al–11.7%Si alloy. *Journal of Materials Science*. 42(13): 5175–5181.
- Liu, L., Samuel, A. M., Samuel, F. H., Doty, H. W., & Valtierra, S. (2004). Characteristics of α -dendritic and eutectic structures in Sr-treated Al–Si casting alloys. *Journal of Materials Science*. 39(1): 215–224.
- Lu, L., Nogita, K., & Dahle, A. K. (2005). Combining Sr and Na additions in hypoeutectic Al–Si foundry alloys. *Materials Science and Engineering: A*. 399(1–2): 244–253.
- Lu, L., & Dahle, A. K. (2006). Effects of combined additions of Sr and AlTiB grain refiners in hypoeutectic Al–Si foundry alloys. *Materials Science and Engineering: A*. 435–436: 288–296.

- Lu, Shu-Zu, and A. Hellawell. (1987). The Mechanism of Silicon Modification in Aluminum-Silicon Alloys: Impurity Induced Twinning. *Metallurgical Transactions A*. 18(10): 1721–33.
- Lu, S.-Z., & Hellawell, A. (1995). Modification of Al-Si alloys: Microstructure, thermal analysis, and mechanisms. *JOM*. 47(2): 38–40.
- McDonald, S. D., Dahle, A. K., Taylor, J. A., & St. John, D. H. (2004a). Eutectic grains in unmodified and strontium-modified hypoeutectic aluminum-silicon alloys. *Metallurgical and Materials Transactions A*. 35(6): 1829–1837.
- McDonald, S. D., Dahle, A. K., Taylor, J. A., & St. John, D. H. (2004b). Modification-related porosity formation in hypoeutectic aluminum-silicon alloys. *Metallurgical and Materials Transactions B*. 35(6): 1097–1106.
- McDonald, S. D., Nogita, K., & Dahle, A. K. (2006). Eutectic grain size and strontium concentration in hypoeutectic aluminium–silicon alloys. *Journal of Alloys and Compounds*. 422(1-2): 184–191.
- Mallapur, D. G., Kori, S. A., & Udupa, K. R. (2010). Influence of Ti, B and Sr on the microstructure and mechanical properties of A356 alloy. *Journal of Materials Science*. 46(6): 1622–1627.
- Martukanitz, R. P. (1993). Selection and Weldability of Heat-Treatable Aluminum Alloys. *ASM Handbook*, 6, 528-536.

- Murty, B. S., Kori, S. A., & Chakraborty, M. (2002). Grain refinement of aluminium and its alloys by heterogeneous nucleation and alloying. *International Materials Reviews*. 47(1): 3–29.
- Nafisi, S., Ghomashchi, R., & Vali, H. (2008). Eutectic nucleation in hypoeutectic Al-Si alloys. *Materials Characterization*. 59(10): 1466–1473.
- Nogita, K., Knuutinen, A., McDonald, S. D., & Dahle, A. K. (2001). Mechanisms of eutectic solidification in Al–Si alloys modified with Ba, Ca, Y and Yb. *Journal of Light Metals*. 1(4): 219–228.
- Nogita, K., McDonald, S. D., & Dahle, A. K. (2004). Eutectic Modification of Al-Si Alloys with Rare Earth Metals. *Materials Transactions*. 45(2): 232–326.
- Nogita, K., Yasuda, H., Yoshida, K., Uesugi, K., Takeuchi, A., Suzuki, Y., & Dahle, A. K. (2006). Determination of strontium segregation in modified hypoeutectic Al–Si alloy by micro X-ray fluorescence analysis. *Scripta Materialia*. 55(9): 787–790.
- Norman, A.F., Prangnell, P.B., & McEwen, R.S. (1998). The Solidification Behaviour of Dilute Aluminum-Scandium Alloys. *Acta Materialia*. 46(16): 5715-5732.
- Norman, A.F., Hyde, K., Costello, F., Thompson, S., Birley, S., & Prangnell, P.B. (2003). Examination of the Effect of Sc on 2000 and 7000 series aluminium castings: For improvements in fusion welding. *Materials Science & Engineering: A*. 354(1-2): 188-198.

- Ourfali, M. F., Todd, I., & Jones, H. (2005). Effect of solidification cooling rate on the morphology and number per unit volume of primary Mg₂Si particles in a hypereutectic Al-Mg-Si alloy. *Metallurgical and Materials Transactions A*. 36(5): 1368-1372.
- Pacz, A. (1920). U.S. Patent No. 1387900A. (Published August 16, 1921). Washington, DC: U.S. Patent and Trademark Office.
- Perepezko, J.H., & Hildal, K. (2006). Analysis of solidification microstructures during wedge-casting. *Philosophical Magazine*. 86(24): 3681-3701.
- Qiyang, Liu, Li Qingchun, and Liu Qifu. (1991). Modification of Al-Si Alloys with Sodium. *Acta Metallurgica et Materialia*. 39(11): 2497–2502.
- Shabestari, S. G., Keshavarz, M., & Hejazi, M. M. (2009). Effect of strontium on the kinetics of formation and segregation of intermetallic compounds in A380 aluminum alloy. *Journal of Alloys and Compounds*. 477(1–2): 892–899.
- Shin, S.-S., Kim, E.-S., Yeom, G.-Y., & Lee, J.-C. (2012). Modification effect of Sr on the microstructures and mechanical properties of Al–10.5Si–2.0Cu recycled alloy for die casting. *Materials Science and Engineering: A*. 532: 151–157.
- Sreeja Kumari, S. S., Pillai, R. M., Rajan, T. P. D., & Pai, B. C. (2007). Effects of individual and combined additions of Be, Mn, Ca and Sr on the solidification behaviour, structure and mechanical properties of Al–7Si–0.3Mg–0.8Fe alloy. *Materials Science and Engineering: A*. 460–461: 561–573.

- Sreeja Kumari, S. S. S., Pillai, R. M., & Pai, B. C. (2008). Structure and properties of calcium and strontium treated Al–7Si–0.3Mg alloy: A comparison. *Journal of Alloys and Compounds*. 460(1–2): 472–477.
- Srirangam, P., Kramer, M. J., & Shankar, S. (2011). Effect of strontium on liquid structure of Al–Si hypoeutectic alloys using high-energy X-ray diffraction. *Acta Materialia*. 59(2): 503–513.
- Srirangam, P., Chattopadhyay, S., Bhattacharya, A., Nag, S., Kaduk, J., Shankar, S., ... Shibata, T. (2014). Probing the local atomic structure of Sr-modified Al–Si alloys. *Acta Materialia*. 65: 185–193.
- Stone, I. C., & Jones, H. (1997). Effect of cooling rate and front velocity on solidification micro structure selection in Al-3.5 wt.% Fe-0 to 8.5 wt.% Si alloys. *Materials Science and Engineering: A*. 226: 33-37.
- Telli, A. I., & Kısakürek, Ş. E. (1986). Effect of antimony additions on the silicon spacing in directionally solidified Al-Si eutectics. *Scripta Metallurgica*. 20(12): 1657–1660.
- Tiedje, N. S., Taylor, J. A., & Easton, M. A. (2012). Feeding and Distribution of Porosity in Cast Al-Si Alloys as Function of Alloy Composition and Modification. *Metallurgical and Materials Transactions A*. 43(12): 4846–4858.

- Timpel, M., Wanderka, N., Schlesiger, R., Yamamoto, T., Lazarev, N., Isheim, D., ...
Banhart, J. (2012). The role of strontium in modifying aluminium–silicon
alloys. *Acta Materialia*. 60(9): 3920–3928.
- Tiryakioglu, M., & Staley, J.T. (2003). Physical Metallurgy and the Effect of Alloying
Additions in Aluminum Alloys. In G.E. Totten & D.S. MacKenzie (Eds.),
Handbook of Aluminum Volume 1 (81-209). New York: Marcel Dekker, Inc.
- Uzun, O., Yılmaz, F., Kölemen, U., & Başman, N. (2011). Sb effect on micro structural
and mechanical properties of rapidly solidified Al–12Si alloy. *Journal of Alloys
and Compounds*. 509(1): 21–26.
- Wang, Q.G. (2003). Microstructural effects on the tensile and fracture behavior of
aluminum casting alloys A356/357. *Metallurgical and Materials Transactions A*.
34: 2887-2899.
- Wang, Q.G., Caceres, C.H., & Griffiths, J.R. (2003). Damage by eutectic particle
cracking in aluminum casting alloys A356/357. *Metallurgical and Materials
Transactions A*. 34: 2901-2912.
- Xiufang, B., Weimin, W., & Jingyu, Q. (2001). Liquid structure of Al–12.5% Si alloy
modified by antimony. *Materials Characterization*. 46(1): 25–29.
- Zarif, M., McKay, B., Li, J., & Schumacher, P. (2010). Study of the Effect of Strontium
(Sr) on the Nucleation of Eutectic Silicon (Si) in High Purity Hypoeutectic Al-5Si
Alloys. *BHM Berg- Und Hüttenmännische Monatshefte*. 155(11): 506–511.

- Zarif, M., McKay, B., & Schumacher, P. (2011). Study of Heterogeneous Nucleation of Eutectic Si in High-Purity Al-Si Alloys with Sr Addition. *Metallurgical and Materials Transactions A*. 42(6): 1684–1691.
- Zhang, D. L., & Cantor, B. (1993). Heterogeneous nucleation of solidification of Si by solid Al in hypoeutectic Al-Si alloy. *Metallurgical Transactions A*. 24(5): 1195–1204.
- Zhang, J., Fan, Z., Wang, Y. Q., & Zhou, B. L. (2000). Effect of cooling rate on the microstructure of hypereutectic Al-Mg₂Si alloys. *Journal of materials science letters*. 19(20): 1825-1828.

6 3-D Printing of Experimental Aluminum Weld Wire

6.1 Abstract

Previous work to develop easy-to-print aluminum alloys involved characterization of the printed properties of commercially available aluminum alloys and wedge casting experiments to screen alloying additions. Screening experiments were used to evaluate additions of magnesium, strontium, titanium boride, and combinations thereof in hypoeutectic Al-5.5% Si and Al-11.6% Si alloys. These screening experiments found additions of strontium and titanium boride to be promising alloying elements for weld-based 3-D printing filament. Additions of strontium, titanium boride, and a combination of strontium and titanium boride were added to a hypoeutectic 4047 aluminum-silicon alloy. These alloys were cast into billets, extruded into rods, and subsequently drawn into wire. Using this wire, test specimens were 3-D printed and their mechanical and microstructural properties were evaluated. Compared to commercially available 4047, it was observed that the AlSiSr alloy exhibited less porosity, equivalent yield and tensile strengths, and twice the ductility.

6.2 Introduction

Previous work developed substrate release mechanisms to allow for sample removal by hand from a print substrate (Chapter 2). Common commercially available weld alloys were 3-D printed and characterized for their microstructural and mechanical properties (Chapter 3). Using this data, experimental aluminum-silicon alloys were developed with additions of strontium, titanium, and a combination of strontium and

titanium (Chapter 4). This study extends the work of the previous chapters. These experimental weld alloys were drawn into weld wire. They were subsequently 3-D printed using a new type of low-cost metal 3-D printer and their microstructural and mechanical properties were analyzed for comparison with previous results.

6.3 Hypotheses

Hypothesis 1: If heat extraction increases, then the 3-D printed block dimensions will be smaller than if a chill plate is not actively used, because the printed parts will solidify faster and not spread as much prior to solidification.

Hypothesis 2: If strontium is added to an aluminum-silicon alloy then porosity will increase because strontium increases hydrogen solubility in molten aluminum-silicon alloys.

Hypothesis 3: If heat extraction increases, then elongation at break will decrease, because the 3-D printed sample will remain cool and stress-relieving heat treatment will not occur from the printing of subsequent print layers.

Hypothesis 4: If strontium additions are added to an aluminum-silicon alloy then elongation at break will increase, because strontium additions modify and refine the silicon eutectic structure and porosity will be more widely distributed.

Hypothesis 5: If heat extraction increases then the secondary dendrite arm spacing will be smaller, because each layer will cool faster, limiting dendrite growth.

Hypothesis 6: If titanium boride is added to the aluminum-silicon alloy then the secondary dendrite arm spacing will decrease, because titanium boride additions act as nucleation points for heterogeneous nucleation.

6.4 Materials & Methods

6.4.1 Casting of Experimental Alloys

Three experimental alloys were manufactured into weld wire for further analysis (Chapter 5) (Table 6.1).

Table 6.1 Target Compositions of Experimental Alloys. All values given in wt%.

Alloy	Si	Sr	Ti	Al
Al-Si-Sr	11-12	0.02-0.04	0	Bal.
Al-Si-TiB	11-12	0	0.04-0.06	Bal.
Al-Si-Sr-TiB	11-12	0.02-0.04	0.04-0.06	Bal.

The same master alloys used in screening experiments were also used as charge material for casting billets (Chapter 5.4.2: Alloy Melting & Pouring). Silicon was added as Al-36wt%Si. Strontium was added in the form of Al-10wt%Sr whereas titanium was added in the form of Al-5wt%Ti-1wt%B. Boron levels were not controlled to a specific composition.

A kiln (LL Kilns, Fuego F1418-240) was preheated overnight to 830°C. 99.999% pure aluminum and the aluminum-silicon master alloys were melted in a graphite crucible in the kiln with an argon cover gas flowing at 0.06 L/sec. A kiln was used to resistively heat the alloy as induction melting can cause excessive stirring of the melt that can introduce dissolved gases and thus porosity in the casting. Once molten, the alloy was

stirred with a graphite rod and allowed to rest for approximately 5 minutes prior to pouring a small button for chemical verification via optical emission spectrometry (OES). The button surface was ground smooth with a lathe. A minimum of three burns were used to verify alloy chemistry. Each alloy was monitored for silicon, iron, magnesium, titanium, boron, and strontium levels. Based upon initial chemical analysis, the chemistry was corrected for the silicon level.

The alloy was degassed with a rotary degassing unit for 10 minutes with an argon gas flow of 0.05 L/sec. During degassing, alloying additions (Al-50wt%Mg, Al-10wt%Sr, and/or Al-5wt%Ti-1wt%B) were added and stirred into the melt using the rotary degassing unit. After rotary degassing, the crucible was stirred while verifying the melt temperature was above 650°C. A second OES button was poured and immediately following this the melt was poured into a permanent grey iron mold shaped for 95 mm diameter \times 305 mm long extrusion billets. The mold was held at an angle of approximately 60° from horizontal during pouring to minimize turbulence of the melt and thus porosity in the casting. The crucible was returned to the kiln while the casting solidified. Prior to pouring the second and third extrusion billets, the melt was stirred each time and returned to the kiln after pouring to prevent premature cooling. After the last extrusion billet was cast, a third and final OES button was poured. OES buttons were poured before the first casting and after the final casting to ensure the melt chemistry was within the target range.

6.4.2 Extrusion & Heat Treatment

Each billet and the extrusion die were preheated to 420°C in a resistance box furnace prior to extrusion by a Daniele Breda 550 commercial extrusion press. The billets were extruded using a die with four cylindrical openings, each 0.9 mm in diameter. Extrusions were coiled by hand while still warm. Extrusions were heat treated in a resistance furnace at 520°C to remove the effects of cold work and to solutionize the alloy. Specimens were harvested from the as-cast, as-extruded, and the heat-treated extruded specimens for microstructural analysis.

6.4.3 Wire Drawing

The extrusions were drawn into weld wire by Hobart Brothers Company at their aluminum wire facility in Traverse City, Michigan. The alloys were first drawn to 0.062” in diameter and heat treated using a proprietary heat treatment for 3 days. Following this the alloys were drawn to a final diameter of 0.035”. Oxides and oils were cleaned from the wire surface prior to shipment.

6.4.4 3-D Printing

The experimental alloys were printed on a new 3-D printer, a modified CNC Router (CNC Router Parts) (Figure 6.1).



Figure 6.1 Image of the CNC-based 3-D printer from CNC Router Parts.

A benchtop CNC router was modified to have a weld gun rather than a router. The table is large (25 x 25 inches) and operates on an x-y-z gantry system using commercially available Mach3 software as a controller. Due to the large size of the table, large prints can be accommodated. Alternatively, multiple print areas and chill plates can be used because the print table is stationary while the weld gun moves, unlike previous printers used. A Haskris R075 chill unit, capable of providing water in the range of -4 to 21°C, was used to provide consistently cool water to the chill plate. This 3-D printing system used a Millermatic 190 welder and a Miller Spoolmate 100 series weld gun to print aluminum. All samples were printed on the chill plate, however, only half of the samples were printed with the chill unit supplying water at 7.2°C. Half of the samples were printed without flowing cooling water, however the chill plate was cooled to 21°C and

the chill unit was turned off prior to printing each of these samples. Temperature may play a role in microstructural and mechanical properties and its effects were studied. Identical welder and printer settings were used for all alloys, with the only differences being the flow of cooling water (Table 6.2).

Table 6.2 3-D Printing Parameters

Parameter	Value
Welder Power Setting (unitless)	1
Wire Feed Rate (mm/sec)	124.6
Print Speed (mm/sec)	10
Wire Stick-Out (mm)	10
Shield Gas Flow Rate (L/sec)	0.24
G-Code Layer Height (mm)	Layers 1-5: 2.5 Layers 6-10: 2.0 Layers 11-15: 1.5
G-Code Lateral Bead Spacing (mm)	2.9
Pause After Each Layer (sec)	60
Number of Print Layers	15

The same 105.6 x 26.4 x 25.4 mm rectangular blocks printed in Chapter 4 were printed in this study on clean and degreased ASTM A36 steel substrates (127 x 127 x 6.35 mm) (Chapter 4.5.2: Printing of Test Specimens). These blocks were printed in a pattern identical to that described in Chapter 4, although number of passes was adjusted to accommodate larger or smaller lateral bead spacings (Figure 4.1). In addition to the three experimental alloys (Table 6.1), ER4047 was printed as a control to compare with previous work (AlcoTec Wire Corporation, 2016). From each alloy, two blocks were printed at 7.2°C and two blocks were printed with cooling water turned off.

6.4.5 Machining & Analysis

All rectangular blocks were machined into four standard round tensile bars (6.35 mm gauge diameter by 25 mm gauge length) using a lathe (ASTM, 2013). The internal (closed) porosity of these tensile samples were measured using the Archimedes' principle as described previously (Chapter 3.4.4: Sample Testing & Analysis). Tensile specimens were pulled to failure in an Instron load frame with an MTS control package using a 22 kN load cell at a strain rate of 10^{-3} sec^{-1} according to ASTM B557 (ASTM, 2013). An Epsilon clip-on axial extensometer with a 25 mm gauge length was used to measure the elongation of the specimen during tensile loading. Only specimens that broke within the gauge section were used for quantitative and qualitative analysis.

Tensile bar grip sections were cut from the tensile bars using a slow-speed diamond saw and the ends were polished to $0.05\mu\text{m}$ surface finish with silica. The ultrasonic modulus of the grip sections was measured using an Olympus 38DL Plus ultrasonic thickness gage as described previously (Chapter 4.5.3: Specimen Machining & Analysis). The polished sections were then mounted in epoxy, etched using Keller's etchant, and their microstructures were analyzed for general morphology and secondary dendrite arm spacing (SDAS) (Chapter 4.5.3: Specimen Machining & Analysis). Chemistries of the polished grip sections were analyzed using optical emission spectrometry (OES) with a boron nitride reduced aperture. This was done to compare the chemistry of cast billets with 3-D printed chemistries.

6.5 Results

Qualitatively, printing with the experimental alloys was easier. The experimental 4047 alloys were less stiff than the commercially available 4047 alloy so the wire did not curve in the direction it was spooled after leaving the weld gun. This resulted in less arc wander. Significantly more arc wander produced more weld spatter when printing with chill water flowing. Beads printed in this condition were taller and visually appeared to have more curvature than weld beads printed without flowing cooling water. Weld beads printed without flowing cooling water appeared to have a flatter surface. The weld arc wandered more on the highly curved, cooled weld beads, resulting in more weld spatter and once arc wander began, it propagated throughout the remainder of the print. Weld spatter increased the dimensions of blocks printed with flowing chill water by as much as 6.35 mm in each dimension compared to the blocks printed without cooling water. The minimal weld spatter in blocks printed without cooling water resulted in higher dimensional control and a better surface finish.

Porosity of 3-D printed specimens ranged from approximately 0.75-1.25% (Figure 6.2). On average, alloys containing strontium exhibited less porosity than alloys without strontium. The addition of strontium to the alloy containing titanium boride additions significantly reduced porosity. Porosities of experimental alloys were less than the $1.42 \pm 0.1\%$ porosity observed for 4047 previously (Chapter 4.5.1: As-Printed Dimensions & Porosity).

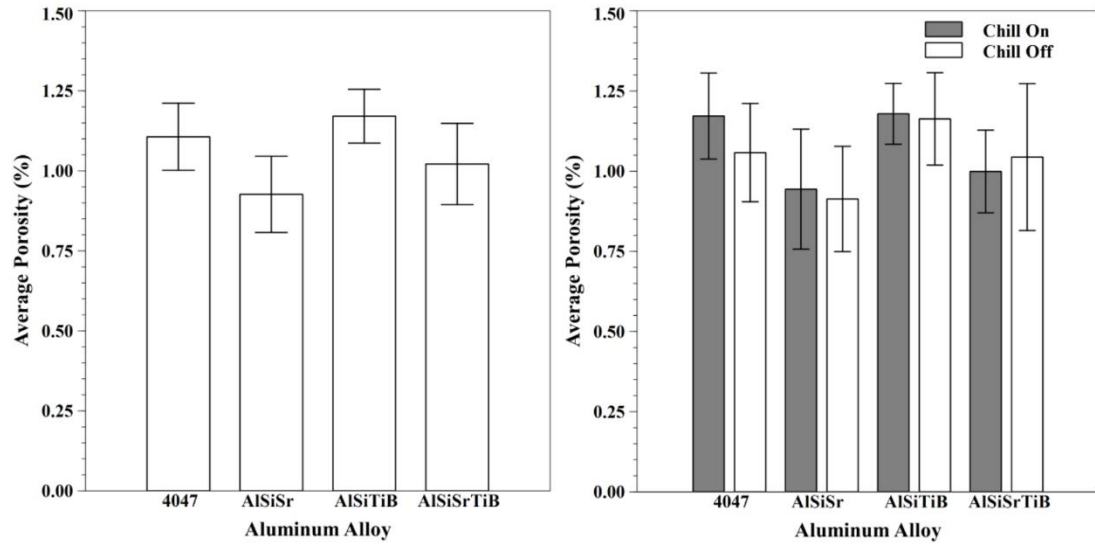


Figure 6.2 Porosity of 3-D printed specimens. Average porosity per alloy (left) and average porosity per alloy based upon chill condition (right). Error bars represent ± 2 standard error.

The yield strengths of 4047 and 4047 AlSiSr were the highest while alloys containing titanium boride exhibited weaker yield strengths (Figure 6.3). There were no significant differences in ultimate tensile strength based upon alloy type. The elongations, and thus ductility, of alloys containing strontium were almost twice that of alloys that did not contain strontium.

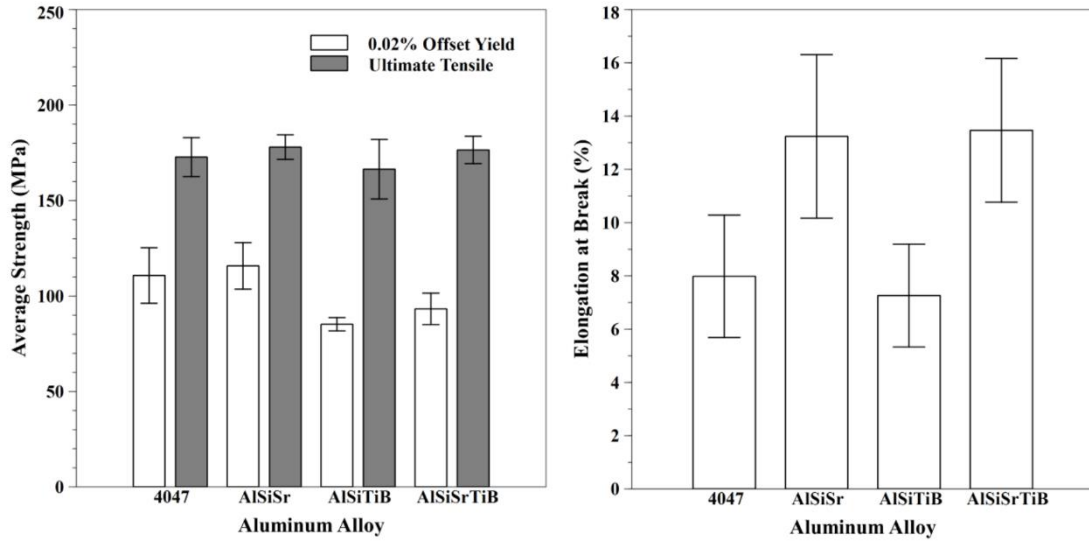


Figure 6.3 Averaged mechanical properties of each printed alloy. 0.02% offset yield and ultimate tensile strengths (left) and elongation at break (right). Error bars represent \pm standard error.

The yield and ultimate tensile strengths benefited from printing without cooling water (Figure 6.4). The strengths of 4047 and 4047 AlSiSr alloys were impacted the most by changes in cooling during printing. The ultimate tensile strengths of alloys containing titanium boride increased with cooling water, which is opposite to the trend observed in 4047 and 4047 AlSiSr. On average, alloys containing strontium exhibited greater ductility in cooled samples whereas alloys that did not contain strontium exhibited greater ductility in samples printed without cooling water. These differences were not statistically significant ($\alpha=0.05$).

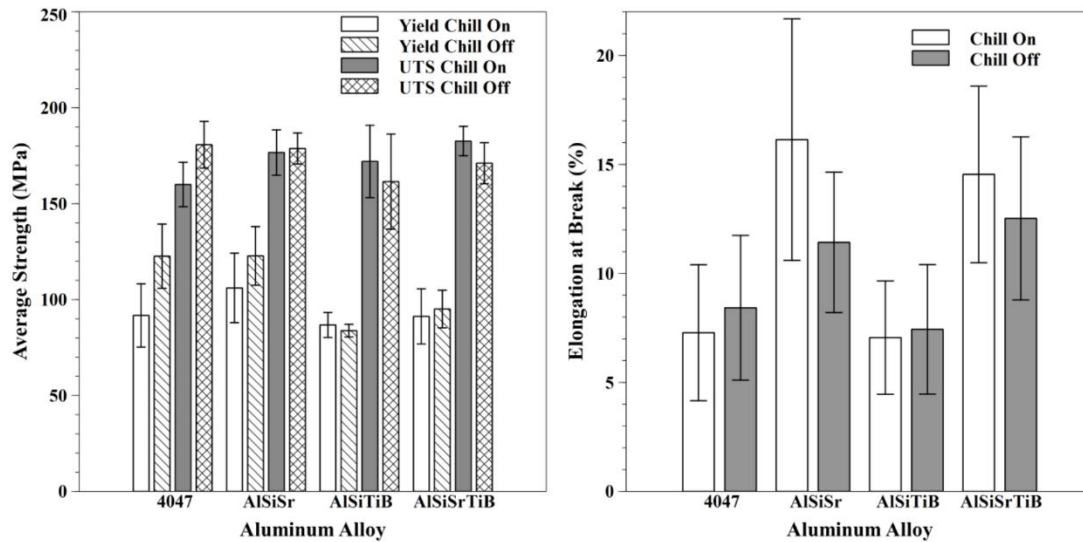


Figure 6.4 Mechanical properties based upon chill condition. 0.02% offset yield strength and ultimate tensile strength (left) with elongation (right). Error bars represent ± 2 standard error.

Significant differences in the ultrasonic moduli of 4047 from the previous study (Chapter 4, Table 4.4) compared with the current study (Table 6.3). Alloys in this study were stiffer than those reported previously, resulting in larger elastic and shear moduli and a lower bulk modulus. No significant differences were observed between the experimental alloys, but the titanium-boride modified alloys exhibited lower elastic and shear modulus than the commercially available 4047 alloys.

Table 6.3 Ultrasonic Moduli of Printed Alloys. Two standard error given for each value.

Alloy	Poisson's Ratio	Elastic Modulus (GPa)	Shear Modulus (GPa)	Bulk Modulus (GPa)
4047 <i>previous study</i>	0.342 ± 0.001	72.7 ± 0.2	27.1 ± 0.1	76.5 ± 0.4
4047 <i>this study</i>	0.315 ± 0.005	82.6 ± 1.9	31.4 ± 0.8	74.4 ± 0.7
AlSiSr	0.326 ± 0.011	79.2 ± 3.6	29.9 ± 1.6	75.8 ± 1.6
AlSiTiB	0.330 ± 0.005	77.3 ± 1.0	29.1 ± 0.5	75.8 ± 1.2
AlSiSrTiB	0.331 ± 0.001	77.5 ± 0.8	29.1 ± 0.3	76.7 ± 0.8

All alloys, except 4047 AlSiTiB, exhibited smaller secondary dendrite arm spacing (SDAS) in the top of the printed blocks than in the bottom near the chill plate (Figure 6.5). In 4047 AlSiTiB, there was no difference in the SDAS in the top of the sample versus near the chill plate. In the 4047, 4047 AlSiSr, and 4047 AlSiSrTiB alloys, the SDAS was larger closer to the chill plate than at the top of the printed blocks. Titanium boride additions in 4047 AlSiTiB and 4047 AlSiSrTiB resulted in the smallest SDAS, particularly when cooling water was flowed through the chill plate. The SDAS of all alloys was significantly larger than that previously measured for commercially available 4047 (Figure 4.14), approximately 12-20 μm in this study versus 8-10 μm reported previously.

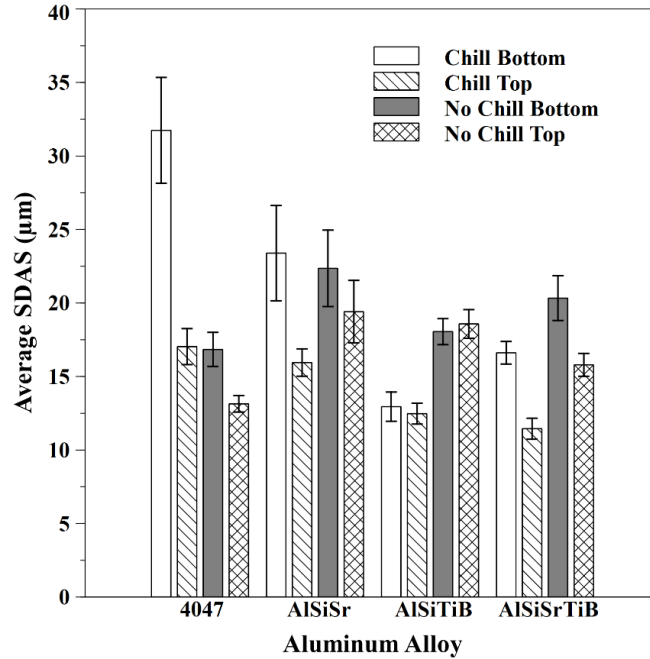


Figure 6.5 Average secondary dendrite arm spacing of printed alloys based upon chill condition. Error bars represent ± 2 standard error.

Significant differences were observed between microstructures in the cast billets (Figure 6.6), in the extruded and heat-treated conditions (Figure 6.7), and after 3-D printing (Figure 6.8). Alloys containing TiB, and particularly AlSiTiB, exhibited primary silicon precipitates in the as-cast structure that persisted in the extruded, heat-treated, and 3-D printed microstructures. The eutectic structures of alloys containing strontium were rounded and finely distributed compared with coarse plates with sharp edges in 4047 and AlSiTiB. Boundaries between print layers were visible in all printed alloys but were most prevalent in 4047 and AlSiSr.

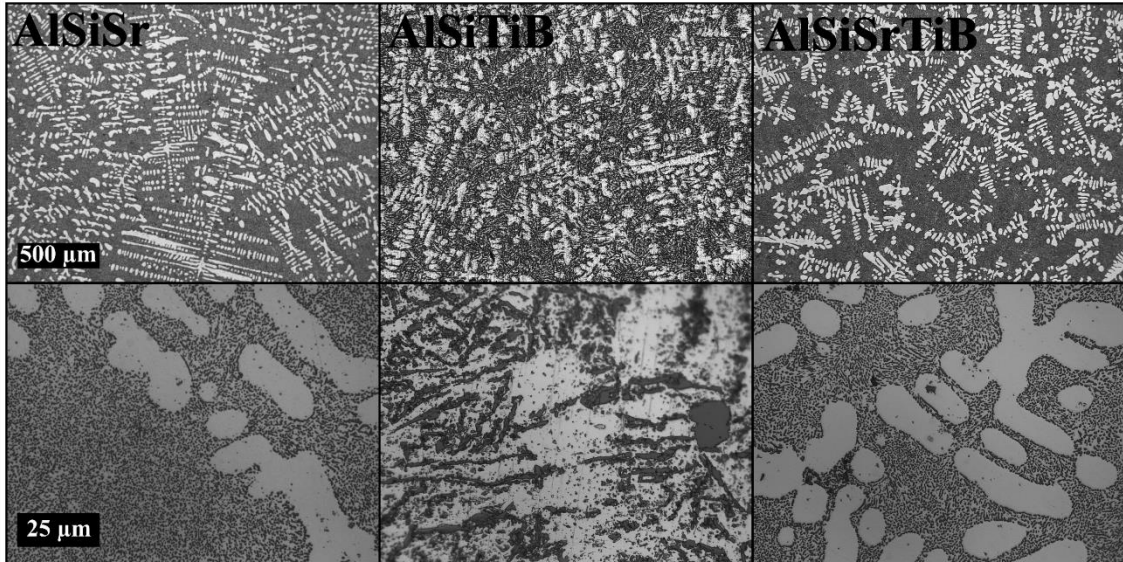


Figure 6.6 Comparison of as-cast billet microstructures of experimental alloys.

Eutectic structures shown for same alloys in bottom row.

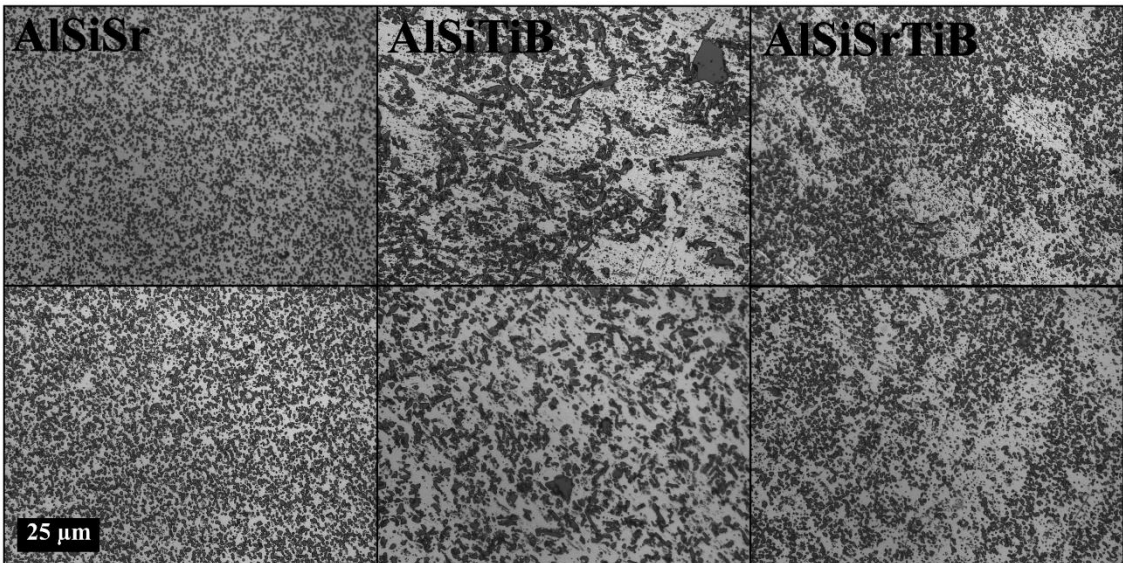


Figure 6.7 Comparison of as-extruded and heat-treated extrusions. As-extruded materials at top and heat-treated analogues at bottom.

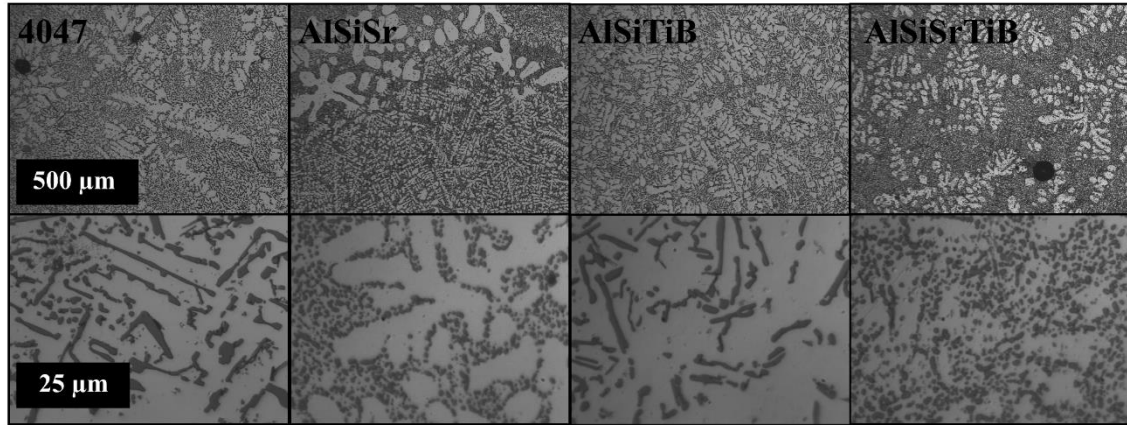


Figure 6.8 Comparison of 3-D printed microstructures. Higher magnification in bottom row displays differences in eutectic structures for each alloy.

Loss of strontium and titanium boride alloying additions from casting through 3-D printing was minimal (Table 6.4). Nearly constant strontium and titanium levels were reported for AlSiSr and AlSiTiB. There were minor losses of strontium and titanium in the AlSiSrTiB alloy, although the observed differences were attributed to variation in OES readings.

Table 6.4 Comparison of Cast and 3-D Printed Chemistries. Values given in wt%.

	Cast Sr	3-D Printed Sr	Cast Ti	3-D Printed Ti
AlSiSr	0.039	0.036	-	-
AlSiTiB	-	-	0.052	0.050
AlSiSrTiB	0.029	0.022	0.053	0.047

6.6 Discussion

Specimens printed on an actively chilled surface were larger than alloys printed with cooling water off. As previously mentioned, the actively chilled surface resulted in printed weld beads that appeared taller and with greater curvature. Visually it appeared

more difficult for the arc to weld in a straight line on this curved surface compared to the flatter weld beads printed with cooling water off. This resulted in greater arc wander and loss of dimensional control. It was originally believed that printing on an actively cooled chill plate would result in smaller printed dimensions because the 3-D printed part would cool quickly and would not spread due to heat build-up in the part. Active feedback on the weld wire location during printing, such as IR imaging of the welding process, may be required to maintain dimensional control when printing on an actively cooled chill plate. Use of a stationary weld head, as was used previously (Chapter 4), may also help to reduce arc wander by limiting forces acting upon the weld gun and wire.

The porosities of strontium-containing experimental alloys were lower than that reported previously for 4047 (Chapter 4.5.1) (Table 6.5).

Table 6.5 Mechanical Properties of Experimental Aluminum Alloys Compared with Previous Results

Alloy	Porosity (%)	Yield (MPa)	UTS (MPa)	Elongation (%)
4047 (Chapter 4.5.1)	1.4±0.1	88±2	180±4	15±1
Cast Al-11.5 Si ^a	-	65	170	8
4047	1.1±0.1	111 ±15	173±10	8±2
AlSiSr	0.9±0.1	116±12	178±6	13±3
AlSiTiB	1.2±0.1	85±3	166±16	7±2
AlSiSrTiB	1.0±0.1	93±8	177±7	14±3

^a Gale & Totemeier, 2003

The yield strengths of 4047 and AlSiSr in this study were significantly greater than that reported previously for 4047 and for cast Al-11.6% Si, whereas there was no significant difference among the ultimate tensile strengths of alloys. There was no significant difference in elongation at break based upon cooling of the chill plate. Strontium-

containing experimental alloys exhibited elongations on par with that previously reported for 4047 and almost twice that of 4047 in this study. However, this trend was only statistically significant at a confidence level of 95% in alloys containing titanium boride. Strontium effectively modified the eutectic structure, resulted in a refined silicon phase that acted as smaller obstacles to dislocation motion than the coarse, unrefined silicon in the unmodified alloys. Additionally, as previously mentioned (Section 5.6), less stress was concentrated on strontium modified silicon particles that were sphere-like with small aspect ratios, reducing cracking of the silicon particles, and increasing ductility (Wang, 2003).

Titanium boride additions had a significant impact upon secondary dendrite arm spacing (SDAS) when active cooling was used. The SDAS of the 4047 and AlSiSr alloys was not significantly affected by cooling. Alloys containing titanium boride were most affected by active versus passive cooling. Titanium boride additions act as nucleation sites allowing for a greater number of primary aluminum dendrites to nucleate. The active cooling limited the growth of these primary aluminum dendrites prior to solidification whereas passive cooling, when water was not flowing through the chill plate, allowed for additional SDAS growth in titanium-boride modified alloys because there was less heat extraction SDAS growth was not limited by fast solidification.

SDAS was significantly larger in this study than that measured previously, 12-20 μm in this study versus 8-10 μm (Figure 4.15). The bead width programmed into the GCode for samples printed on the chill block was smaller (2.9 mm) than was used previously (3.3 mm). In order to print the same sized block with the smaller bead width in

this study, more lines had to be printed per layer. At the same print speed, this resulted in a longer print time and greater heat input into the 3-D printed part over time. The overall active print time not including any print pauses for samples printed in this study on the CNC printer was 30 minutes and 2.5 seconds. The same active print time in specimens printed previously on the magnetic printer was 22 minutes and 26.1 seconds (Chapter 4). Heat input applied to a weld can be calculated knowing the weld voltage (V), weld current (A), weld speed (S), and knowing the efficiency of the welding process (η) (Equation 6.1) (Kou, 1987).

$$\text{Heat Input (J/mm)} = \frac{\eta * V * A}{S} \quad (6.1)$$

The efficiency of gas metal arc welding processes can range from 0.65-0.85 and was assumed to be 0.75 (Kou, 1987). Using Equation 6.1, heat input was calculated to be 175.5 J/mm. The total print length in specimens printed in this study on the CNC printer was 18.1 meters whereas this value was 13.5 meters in samples printed previously on the magnetic printer (Chapter 4). This difference in overall print length resulted in an additional 805 kJ of heat applied to samples printed in this study. Greater heat input and slower cooling would result in an increase in the SDAS and may have also acted as a stress relieving heat treatment. This in combination with lower porosity levels likely contributed to the greater yield strengths observed in 4047 and AlSiSr in this study as opposed to that previously reported (Chapter 4). Larger dendrite arm spacing has also been observed to decrease ductility in cast aluminum alloys, which may account for the lower ductility of specimens printed in this study compared with prior results (Chapter 4) (Wang, 2003).

The strontium and titanium boride additions survived the welding thermal environment with zero to minimal losses. Strontium exhibited positive influences on the porosity and mechanical properties of the experimental alloys. The modification to the silicon eutectic structure without additions of grain refining titanium boride was the most effective at improving printability and properties of 3-D printed parts.

Based upon the provided results, hypotheses could either be accepted or rejected at 95% confidence (Table 6.6). Trends predicted in hypotheses may have been observed on average but were not statistically significant ($\alpha=0.05$). Only hypothesis 6 could be accepted for all alloys whereas hypotheses 4 and 5 were only true when applied to alloys containing titanium boride additions.

Table 6.6 Results of Hypothesis Testing

#	Brief Summary	Result
1	Printing on a chill results in smaller prints	Reject
2	Sr additions will increase porosity	Reject
3	Printing on a chill results in less ductility	Reject
4	Sr additions will increase ductility	Accept in TiB alloys only
5	Printing on a chill results in smaller SDAS	Accept in TiB alloys only
6	TiB additions will decrease SDAS	Accept

Simple aluminum-silicon castings may be readily 3-D printed for custom applications. For instance, aluminum bracket spindle mounts that are typically cast could also be produced via weld-based 3-D printing. These brackets are commonly used to mount round tools or features to a flat plate. Near net shape bracket spindle mounts could be printed using the GMAW-based 3-D printer and the part could be machined to final specified dimensions. This bracket could be manufactured from the experimental

strontium-modified aluminum-silicon presented in this study to exhibit greater ultimate tensile and yield strengths and elongation at break compared with cast 443.0 alloy (ASM International, 1990).

Other items that could be 3-D printed from these alloys include outdoor recreational products: tent stakes, stove bases for backcountry cooking, and ice axes. These items could be custom printed for specific tents, stoves, and axe requirements using light-weight aluminum materials. As these printed parts become worn or lost in the great outdoors, new parts could simply be 3-D printed.

While the mechanical properties of the strontium modified aluminum-silicon alloy developed in this study were superior to baseline cast or wrought alloys, they cannot yet compete with common structural aluminum alloys such as 6061 (ASM International, 1990). Significant progress has been made to show alloying strategies common in other manufacturing processes can be applied to welding alloys with success. Further alloying work may allow for weld-based 3-D printing of more structural aluminum alloys.

6.7 Conclusion

A near eutectic aluminum-silicon alloy was modified with additions of strontium, titanium boride, and a combination of both strontium and titanium boride. The alloys were cast, extruded, and drawn into wire prior to 3-D printing. The mechanical and microstructural properties of 3-D printed experimental aluminum alloys were compared with those for printed, commercially available 4047 aluminum. This work was performed

in order to identify an aluminum alloy that is easier to print with and exhibits superior properties to commercially available alloys.

Printing test specimens with cooling water negatively affected print quality by causing an increase in weld arc wander, resulting in more weld spatter that increased sample size and diminished surface finish. The alloy modified with only strontium exhibited the best combination of properties: low porosity, high strengths, and high ductility. The AlSiSr alloy exhibited less porosity than the samples printed from commercially available 4047, similar yield and ultimate tensile strengths, but twice the ductility.

6.8 References

AlcoTec Wire Corporation. Alloy 4047 weld data sheet. <http://www.alcotec.com/us/en/support/upload/a4047tds.pdf>, last accessed 3 February 2016.

ASM Handbook Committee. (1978). *Metals Handbook: Vol. 2, Properties and selection—nonferrous alloys and pure metals*. American Society for Metals, Metals Park, OH.

ASTM B557-02. *Standard Test Methods for Tension Testing Wrought and Cast Aluminum- and Magnesium-Alloy Products*. ASTM International, West Conshohocken, PA, 2013, www.astm.org.

Gale W. F., & Totemeier, T. C. (Eds.). *Smithells metals reference book*, 8th Ed., Butterworth-Heinemann, 2003, 14-16.

Kou, S. (1987). *Welding Metallurgy*. New York: John Wiley & Sons.

Wang, Q.G. (2003). Microstructural effects on the tensile and fracture behavior of aluminum casting alloys A356/357. *Metallurgical and Materials Transactions A*. 34: 2887-2899.

7 Conclusions

A new, low-cost method to 3-D print metals was successfully demonstrated. This printer utilized standard gas metal arc welding technology to fuse together parts on a layer-by-layer basis. Methods were developed to allow for easy part removal, eliminating the need for expensive and time consuming cutting methods.

Initial work indicated that aluminum was not as easy to print with as steel. The mechanical and microstructural properties of common commercially available 1100, 4043, 4943, 4047, and 5356 aluminum weld alloys were characterized. The mechanical properties of parts produced via this 3-D printing process were on par or superior to their traditionally manufactured counterparts. Using this behavior, 4047 and 4943 were identified as alloys that exhibited a good combination of strength and ductility with low porosities but could still benefit from additional alloying work to further increase ductility and decrease porosity.

Additions of 0.3 wt% magnesium, 0.03 wt% strontium, and 0.05% titanium as titanium boride were added to 4047 and 4943-type aluminum alloys. These alloys were cast into wedge-shaped castings that could induce the same solidification rates as those observed during 3-D printing. The additions of strontium and titanium boride to an Al-11.6% Si alloy similar to 4047 refined the microstructure. None of the alloying additions to the Al-5.5% Si alloy similar to 4943 resulted in a modified structure. The high-silicon alloy exhibited greater porosities than the low-silicon alloy. However, these differences in porosity did not affect the ductility of either alloy modified with both strontium and

titanium boride which exhibited the greatest ductilities of the alloys studied. Based upon their mechanical and microstructural behavior, additions of strontium and titanium boride to 4047-type aluminum alloys were chosen for further analysis.

Strontium and titanium boride-modified 4047-type aluminum alloys were cast into extrusion billets, extruded into rods, and drawn into weld wire. These wires were 3-D printed and the parts were characterized for their mechanical and microstructural properties. Experimental alloy weld wires were less stiff and were observed to be easier to print with than commercially available aluminum weld wires. Printing on a chill plate did not add any significant benefit in this study compared with previous studies as it resulted in greater arc wander and weld spatter. The smaller weld bead spacing in the print code in this study resulted in a greater overall print length and print time as compared with prior work, resulting in an additional 805 kJ of heat input into the printed part. This increased heat input slowed cooling and resulted in a larger dendrite arm spacing.

No losses of strontium or titanium boride were observed from the welding process and both provided significant modification and grain refinement to the aluminum-silicon alloys. The AlSiSr alloy without any titanium boride additions, was observed to exhibit less porosity when printed (0.9%) equivalent yield and tensile strengths (116 MPa and 178 MPa, respectively), and twice the ductility (13% elongation) as the commercially available 4047 aluminum alloy.

A low-cost method of printing metal parts has been demonstrated. Parts from both aluminum and steel can be printed and removed from a print substrate with minimal energy. To improve printability and print quality in aluminum parts, process modifications and alloying experiments were performed. No significant benefit was observed from modifying the printing process to include a chill plate. Significant improvements were made to the printability, porosity, and ductility of a near-eutectic Al-11.6% Si alloy by alloying with strontium. These improvements will simplify aluminum 3-D printing with GMAW technology.